VLT

High Frequency Fluctuations of Water and Carbon Dioxide, Paranal June 25–30, 2007

DRAFT

Prepared	Richard J. Mathar	February 13, 2008	
			Signature
Approved			
			Signature
Released			
			Signature

Change Record

Issue	Date	Section/Parag. affected	Reason/Initiation/Documents/Remarks

Contents

List of Figures

List of Tables

1 OVERVIEW

1.1 Scope

Fluctuations of water and carbon dioxide densities have been measured by W. J. Jaffe and R. S. Le Poole near the roof top of the VLTI control building, in the VLTI tunnel, and the hull of the VST dome with a LI-COR gas analyzer [4] at the end of June 2007. The principle of measurement is optical absorption filtered around IR wavelengths of 2.595 μm (H$_2$O absorption band) and 4.26 μm (CO$_2$ absorption band) [17]. This provides a first view into fast fluctuations of gas species important to the refractive indices in the IR. The sampling frequency is complementary to the frequencies of once per minute at which the ambient data server, and of once per five minutes at which the sensors of the GENIE project [2, 3, 18] are logged.

Section 2 plots all raw data obtained during the campaign, points at the need for re-calibration, then plots the calibrated data. Section 3 derives power density spectra and structure functions from these for 17 different night-time intervals of 4 hours. Section 4 contains a summary.

1.2 Applications

The molecular number (molar) densities are the immediate input to calculations of refractive indices. Scaling with the Avogadro Constant gives the corresponding changes in refractive indices at various infrared wavelengths, with implications for AO, TAD and fringe trackers. Comparison with interferometric phases measured at wavelengths of 10 micron with MIDI at nights during the same period will be done separately [16]. It requires additional models with scale heights of wind velocities and of number densities of the Paranal atmosphere above Paranal, models of how the interferometer integrates phases across the UT pupils plus an error analysis of this type of high-frequency MIDI data reduction, and is decidedly more complicated and specialized than what is presented here.

This script is available under the URL http://www.strw.leidenuniv.nl/~mathar/public/UL-TRE-ESO-15000-0 pdf and changed without further anouncement.

1.3 Data Sources

This manuscript has drawn information from

- a one-time campaign with a loaned LI-COR water/carbon-dioxide gas analyzer, June 25–30, 2007.

- an ASCII interface to the temperatures, pressures, relative humidities, wind directions, wind velocities and seeing parameters stored in the Paranal ambient server data base [21]. We placed a description to this interface in http://www.strw.leidenuniv.nl/~mathar/vlti/.

- data on precipitable water vapor, wind speed and wind direction on the 300 mbar level (height) originating from the ECMWF, taken from a file in http://www.eso.org/gen-fac/ pubs/astclim/forecast/meteo/ERASMUS/.

- Temperatures and relative humidities of four Vaisala HMT323/HMP303 sensors in the VLTI tunnel and ducts copied from S. Wehner's directory on ESO's anonymous ftp://ftp.eso.org server. (They cover one week of the past with a moving wall, so they are not there any longer by

now.) For historical reasons these are referred to as GENIE sensors. Statistics of these data has been gathered while evaluating the the PRIMA error budget [13, App.] and is not in the scope of the current report. Estimates of time constants for temperature and humidity exchange between the tunnel and ambient air are in Appendix 6.3.1 of [13].

1.4   References

[1] Abramowitz, M., & Stegun, I. A. (eds.) 1972, Handbook of Mathematical Functions (New York: Dover Publications), 9th ed.

[2] Albrecht, S. 2004, GENIE T/RH sensor project, Installation of the Humidity Sensors at the VLTI. VLT-TRE-NEV-15846-xxxx

[3] Albrecht, S., Bakker, E. J., de Jong, J. A., Tubbs, R. N., Meisner, J., & le Poole, R. 2004, in New Frontiers in Stellar Interferometry, edited by W. A. Traub (Int. Soc. Optical Engineering), vol. 5491 of Proc. SPIE, 1266

[4] Bioscienes, L. 2007, LI-7500 CO_2/H_2O gas analyzer, Instruction Manual, Lincoln, Nebraska, USA. URL http://www.licor.com/env/Products/GasAnalyzers/7500/7500_manual.jsp

[5] Boyd, R. W. 1978, J. Opt. Soc. Am., 68, 877

[6] Detto, M., & Katul, G. G. 2007, Bound.-Layer Metrology, 122, 205

[7] Feng, S., & Wenhan, J. 2002, Appl. Opt., 41, 3385

[8] Gradstein, I., & Ryshik, I. 1981, Summen-, Produkt- und Integraltafeln (Thun: Harri Deutsch), 1st ed.

[9] Innocenti, C., & Consortini, A. 2004, J. Mod. Opt., 51, 333

[10] Keeling, C. D., & Whorf, T. P. 2005, Atmospheric CO_2 records from sites in the SIO air sampling network. In Trends: A compendium of Data on Global Change, Tech. rep., Tenn., USA

[11] Kowalski, A. S. 2006, Bound.-Layer Metrology, 120, 353

[12] Mathar, R. J. 2004, Appl. Opt., 43, 928

[13] — 2006, Astrometric Survey for Extra-Solar Planets with PRIMA, Astrometric dispersion correction. UL-TRE-AOS-15753-0010

[14] — 2006, PRIMA Non-Astrometric Modes, External Fringe Tracking for MIDI. UL-ICD-DDL-15728-0009

[15] — 2007, J. Opt. A: Pure and Appl. Optics, 9, 470

[16] Mathar, R. J., & Jaffe, W. J. 2007, Correlation of MIDI Phase Fluctuations with Fluctuations of Water and Carbon Dioxide, Paranal June 2007. UL-TRE-MID-15829-0113

[17] Ohtaki, E. 1984, Bound. Layer Met., 29, 85

[18] Puech, F., Lévêque, S., Sarazin, M., & Mathar, R. J. 2006, in Advances in Stellar Interferometry, edited by J. D. Monnier, M. Schöller, & W. Danchi (Int. Soc. Optical Engineering), vol. 6268, 1244

[19] Roddier, F. 1981 (Amsterdam: North Holland), vol. XIX of Prog. Opt., 281–376

[20] Sahlée, E., Smedman, A.-S., & adn Ulf Högström, A. R. 2008, Bound.-Layer Metrology, xxx

[21] Sarazin, M. 2003, Astroclimatology of Paranal, Tech. rep., European Southern Observatory. URL http://www.eso.org/gen-fac/pubs/astclim/paranal

[22] Wagner, W., & Pruß, A. 2002, J. Phys. Chem. Ref. Data, 31, 387

[23] World Data Centre for Greenhouse Gases 2006, WMO WDCGG Data Summary No. 30–GAW Data, Vol IV–Greenhouse Gases and other Atmospheric Gases, Tech. rep.

1.5   Acronyms

AO	Adaptive Optics
ASCII	American Standard Code for Information Interchange http://http://en.wikipedia.org/wiki/American_Standard_Code_for_Information_Interchange
DFT	Discrete Fourier Transform
DL	Delay Line
ECMWF	European Center for Medium-Range Weather Forecasts http://www.ecmwf.int/
ESO	European Southern Observatory http://www.eso.org
GENIE	Ground based European Nulling Interferometry Experiment http://www.strw.leidenuniv.nl/~nevec/GENIE/
GUI	Graphical User Interface
IR	Infrared
LN	liquid nitrogen
MIDI	Mid-Infrared Interferometric Instrument http://www.mpia.de/MIDI
NEVEC	NOVA-ESO VLTI Expertise Center http://www.strw.leidenuniv.nl/~nevec
NOVA	Nederlandse Onderzoekschool voor Astronomie http://www.strw.leidenuniv.nl/nova/
PDF	Power Density Function http://en.wikipedia.org/wiki/Spectral_density
ppmv	parts-per-million of volume
PRIMA	Phase-Reference Imaging and Microarcsecond Astrometry http://obswww.unige.ch/Instruments/PRIMA

TAD   transverse atmospheric dispersion

URL   Universal Resource Locator

UT   Unit Telescope (of the VLTI) http://www.eso.org/projects/vlt/unit-tel/

VLTI   Very Large Telescope Interferometer http://www.eso.org/vlti

VST   VLT Survey Telescope http://vstportal.oacn.inaf.it/

2   SYNOPSIS WITH WEATHER TOWER AND GENIE DATA

2.1   Raw Data

Figure 1:   The picture indicates the location of the weather pole on the north rim of the platform by the long narrow shadow. In the NEVEC logo on the cover page, it is the red and white pin at the right. The VST dome is seen North of UT4.

We label LI-COR data sets as `Lfile` followed by consecutive numbers. Peaks and fluctuations of the molecular densities measured at the start and end of these intervals are expected because this implies human activity (Sect. 6.3 in [16]); these are outliers not be booked as weather data.

We start with the first group of files of Table 1: A rough comparison between the densities measured here at a height of roughly 3 1/2 m above the platform and those reported by the Paranal ambient data server from the weather pole at a height of 30 m http://archive.eso.org/eso/ambient-database.html is done in the Fig. 2–4. The time axis is in UT1, throughout.

Remarks:

Lfile$n$	start	end	location
1	2007-06-25T01:47:08	2007:06:25T13:09:34	stair to roof top VLTI control building
2	2007-06-25T13:10:17	2007:06:25T21:19:18	stair to roof top VLTI control building
3	2007-06-25T21:19:38	2007:06:26T13:16:30	stair to roof top VLTI control building
4	2007-06-26T13:16:40	2007:06:26T21:49:51	stair to roof top VLTI control building
5	2007-06-26T21:50:33	2007:06:27T13:18:07	stair to roof top VLTI control building
6	2007-06-27T19:36:57	2007:06:28T15:39:29	VLTI tunnel near lab entrance
7	2007-06-28T15:41:01	2007:06:28T18:38:39	VLTI tunnel near lab entrance
8	2007-06-28T22:00:09	2007:06:29T13:05:20	VST platform
9	2007-06-29T13:15:41	2007:06:29T21:34:11	VST platform
10	2007-06-29T21:34:34	2007:06:30T12:26:30	VST platform

Table 1: LI-COR measurements have been taken at three different locations.

- The relative humidity reported by the weather pole has been converted to absolute densities with standard conversions (Fig. 37 in [13] or `http://www.strw.leidenuniv.nl/~mathar/progs/prWaterWeb.html`), taking the temperature measured by the weather pole to construct the saturation pressure [22].

- Some ESO driver software truncates the number of significant digits of the weather pole humidity, which leads to the artificial quantisation of the green curve of the water number density from the weather pole as shown.

- Spike removal on the raw LI-COR data was done according to the following "Markov"-type stop criteria: (i) H_2O density must remain below 0.4 mole/m^3 and cannot change by more than 50 % between two readings. (ii) CO_2 fraction must stay between 300 and 400 ppmv. (iii) Absorptance in the CO_2 channel must remain in the interval [0,1]. (iv) Absorptance or number density in the CO_2 channel cannot change by more than 50 % between two readings. (v) Temperature cannot change by more than 1 °C between two readings.
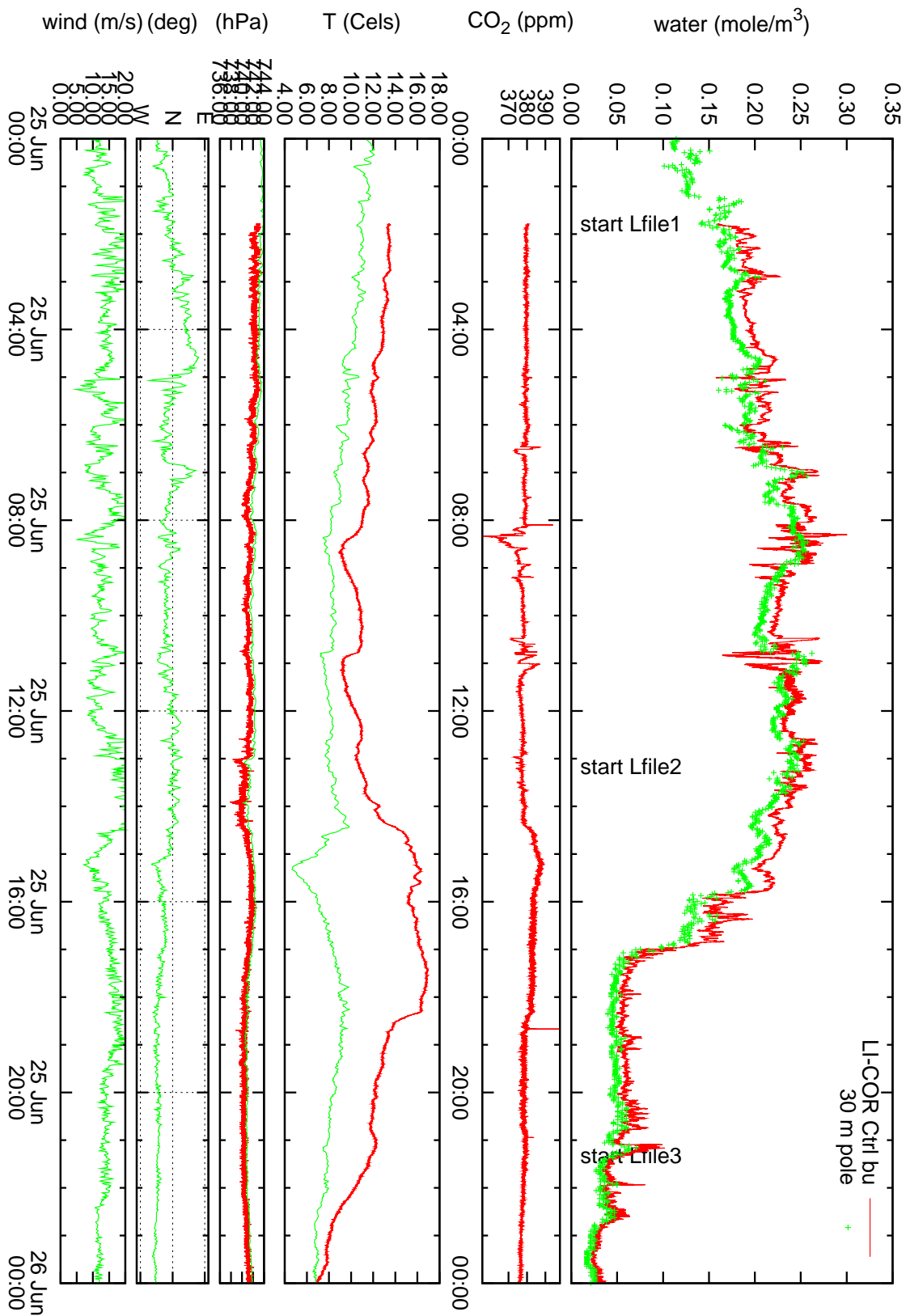
Figure 2: LI-COR water number density near the VLTI control building roof in comparison with weather pole data for the first 24 hrs of data.
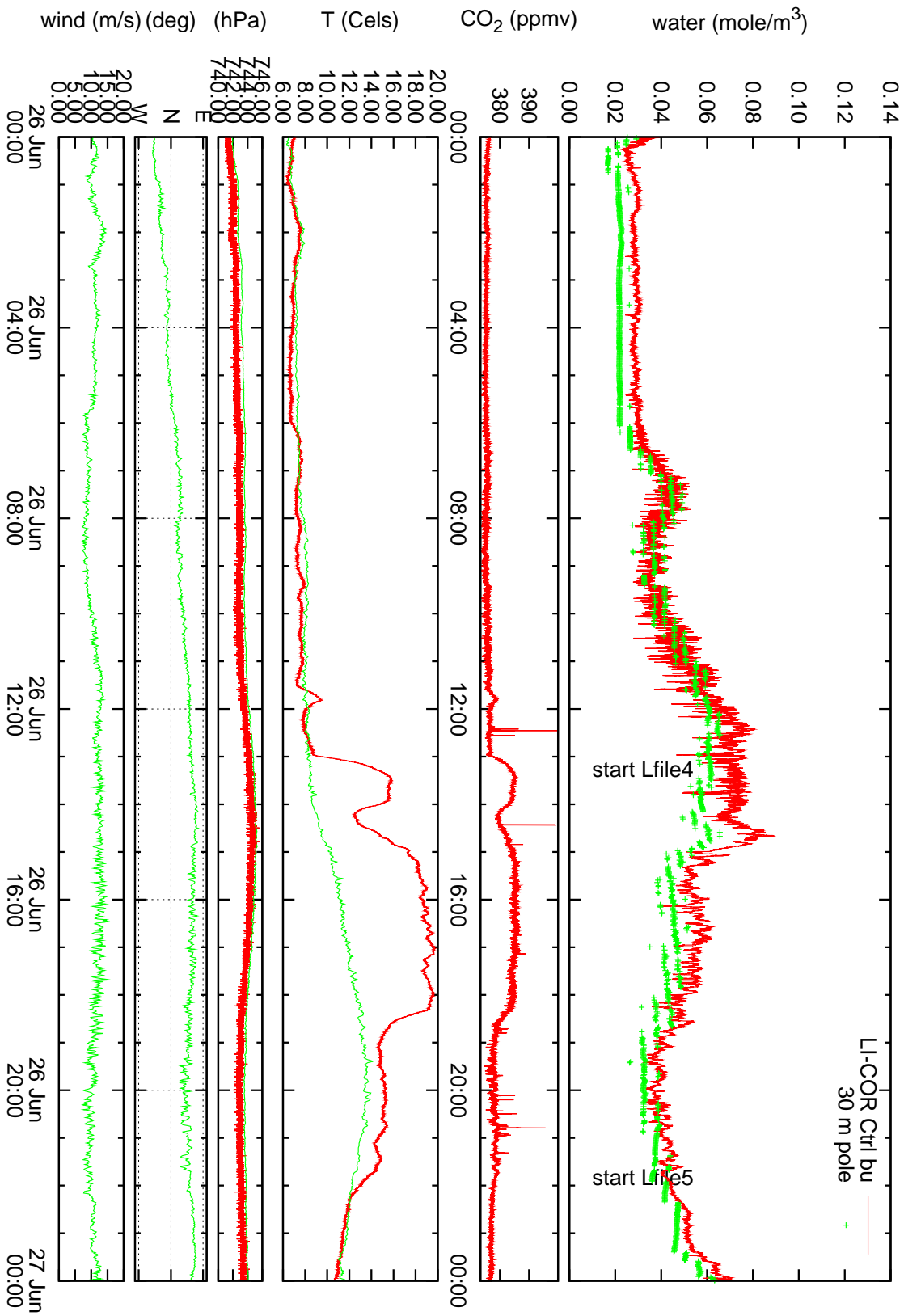
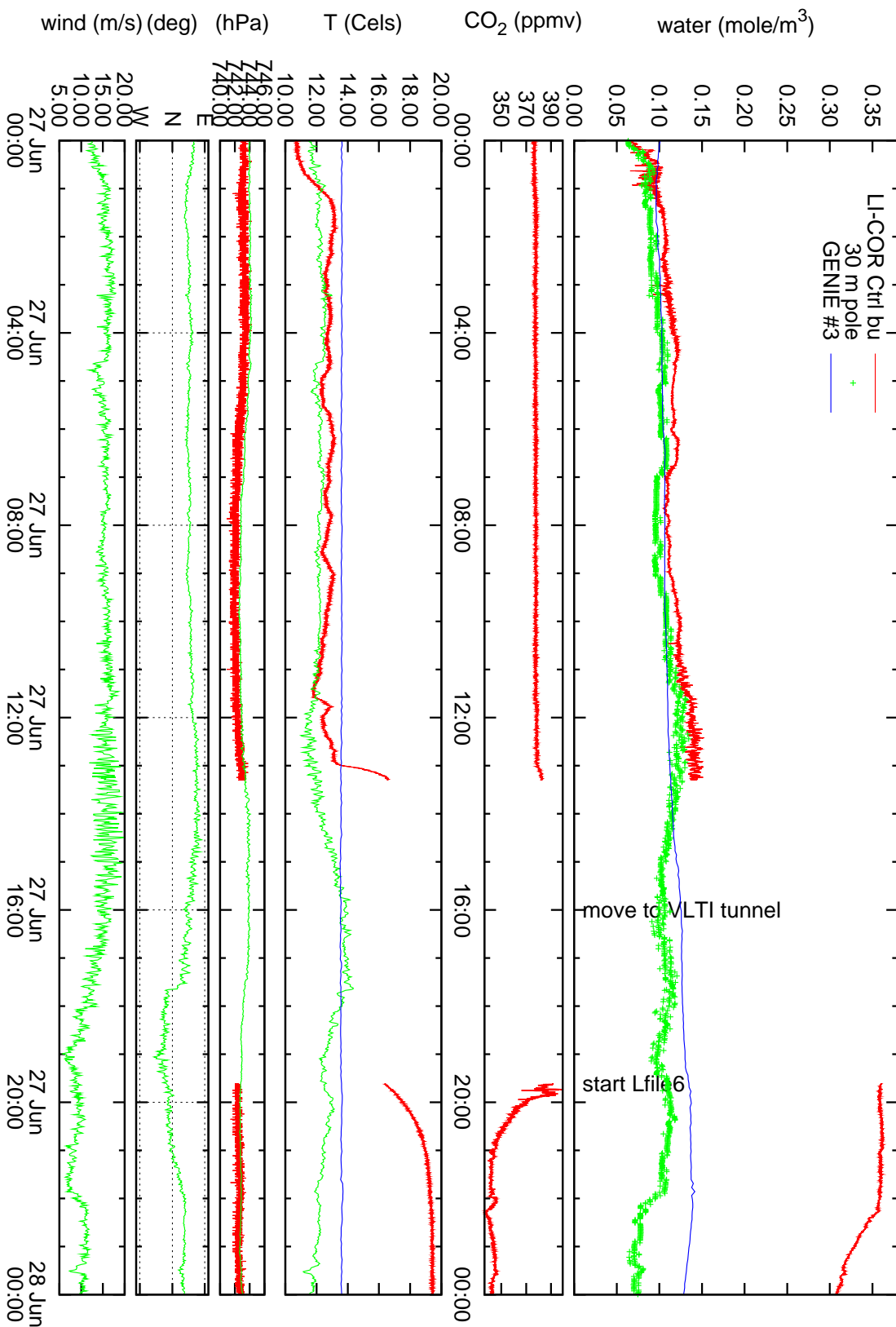Figure 3:   Water number density near the VLTI control building roof for the second 24 hrs of data.

Figure 4: Water number density near the VLTI control building roof for the third 24 hrs of data, the last 4 hrs in the VLTI tunnel.

The second group of files of Table 1: A comparison between the data measured by the LI-COR instrument and the third of the GENIE sensors, both in the VLTI tunnel near M15 and near the entrance to the VLTI laboratory is shown in Fig. 5. The GENIE data are also available from `http://www.strw.leidenuniv.nl/~mathar/vlti/`.

The final set of data was taken in the VST dome, summarized in Figs. 6–7, in an attempt to reach higher altitude less influenced by turbulence generated by domes and buildings.

Since the weather pole pressure is measured at roughly 3 m above ground, a small difference between the pressures of the ambient data server and those reported here is expected. At an approximate scale height of 9.7 km of the atmosphere, the reduction of the pressure at the VST dome, estimated at 25 m above ground, to the pressure measured roughly 3 m above ground is a factor of $e^{-22/9700} \approx 0.9977$. At 740 hPa this is a difference of 1.7 hPa, which is observed in Figs. 6–7.

The molar fraction of carbon dioxide is shown in units of (μmole per mole of air) during the campaign. It is near 380 ppmv during the first 2 1/2 days of outdoor measurements, and more strongly fluctuating with an average of 340 ppmv in the tunnel. Sunrise at this place and time was at 11:25 hours, sunset at 22:00 hours UT1, not applying any corrections for twilight or mountain altitude.

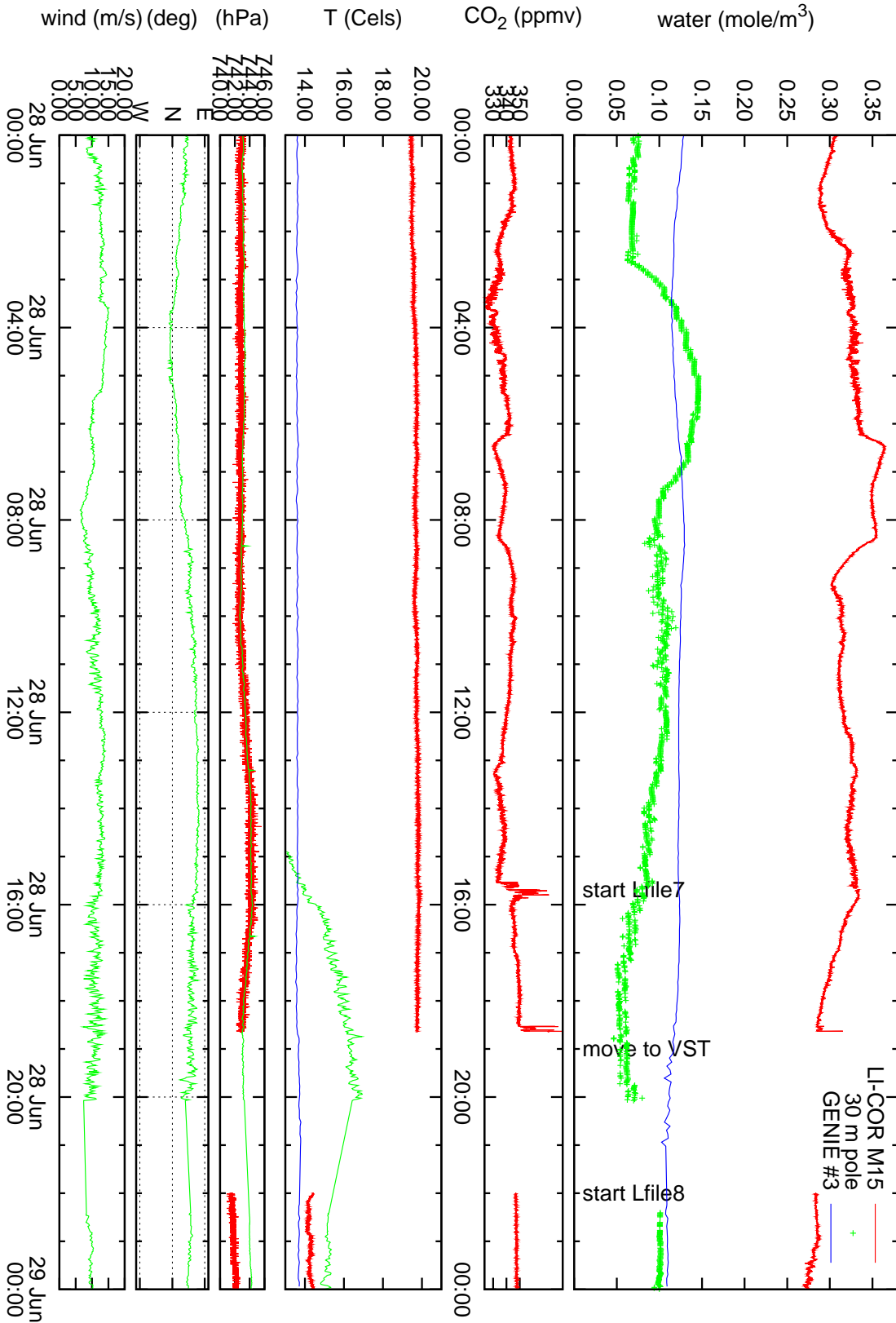Figure 5:   Number densities in the VLTI tunnel near the entrance to the VLTI laboratory. Red the LI-COR output, blue the GENIE humidity (converted from relative to absolute using the GENIE temperature), and green the humidity at the weather pole (converted from relative to absolute using the weather pole temperature).
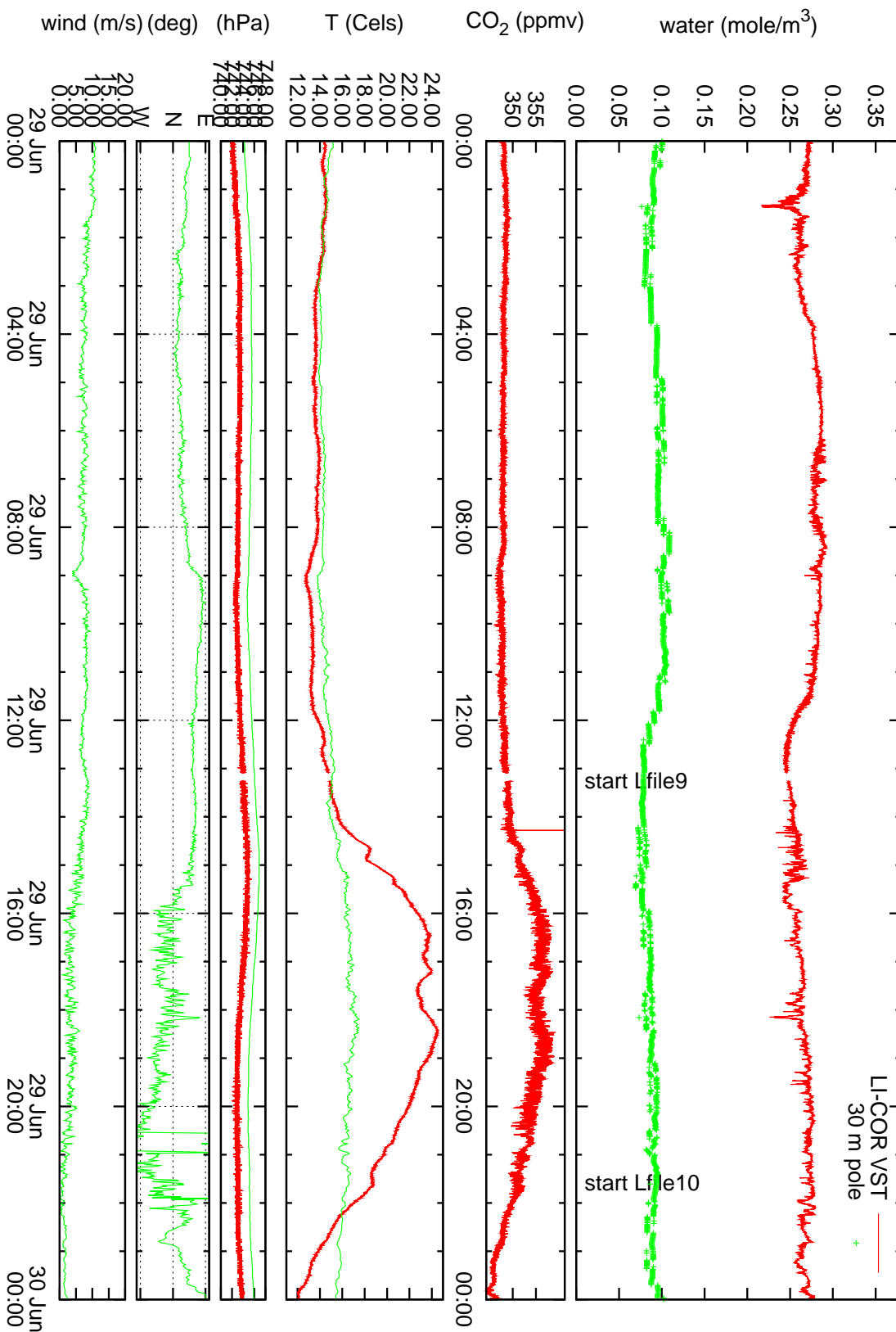
Figure 6: Number densities in the VST dome and from the ambient data server. Continued in Fig. 7.
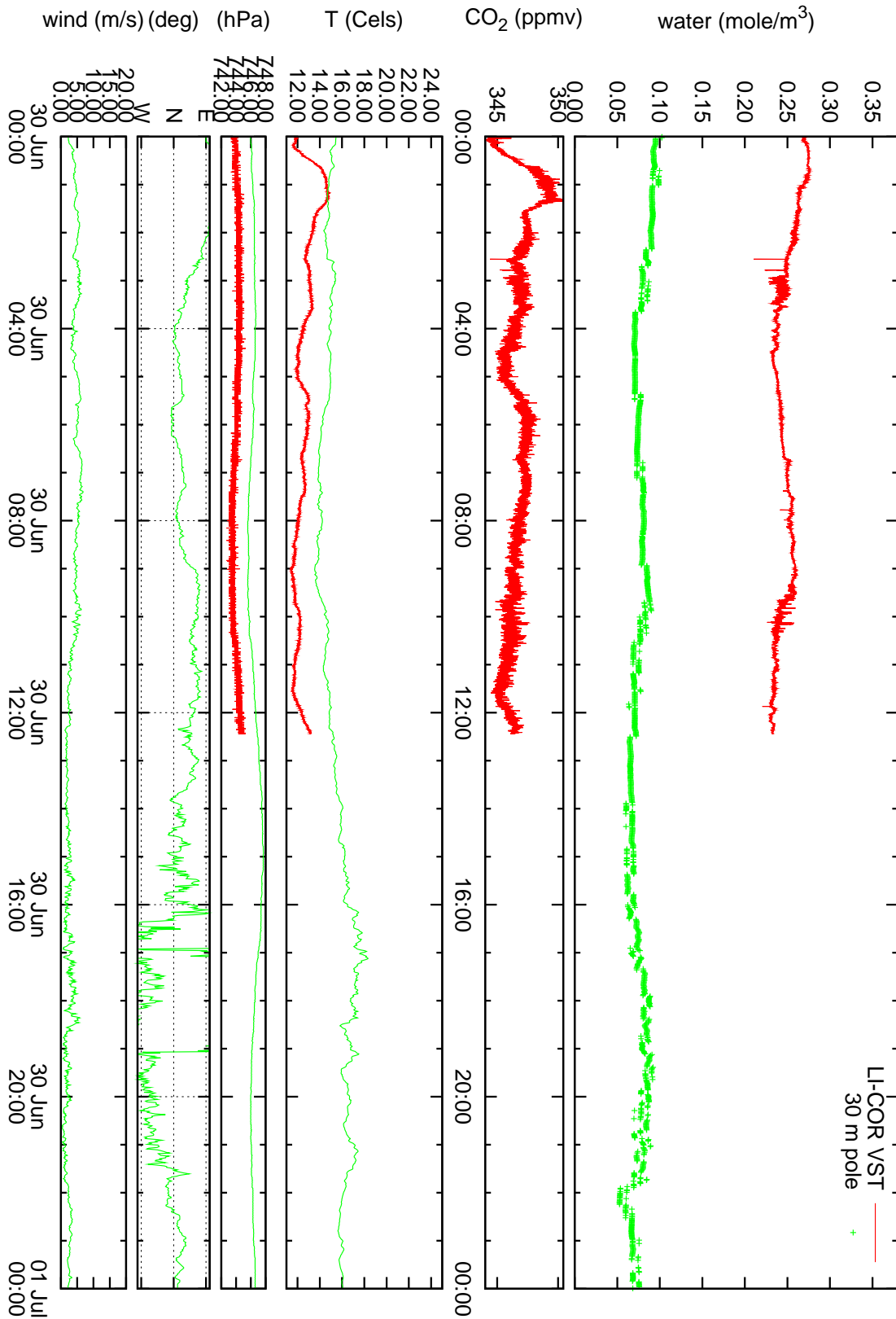
Figure 7: Number densities in the VST dome and from the ambient data server until the end of the campaign. In the lower two panels, the definition of wind direction becomes fuzzy at small wind speeds.

2.2 Tunnel Humidity and Temperature

Unrelated to the LI-COR data, the measurements of temperatures and humidities at four places in the VLTI tunnel and ducts are summarized in Figures 8–11. The surplus of the water molecular density relative to the weather pole data is a standard feature during the past two years (Appendix 6.1 in [13]) with unknown origin.

MIDI observations during these nights [16] may explain some of the fluctuations of some of the parameters in the three lower plots in these figures, since fluctuations in temperature/humidity are stronger in ducts which are in use and therefore not covered. This obviously is out of topic for this report here.

Figure 8: Data of the four temperature/humidity sensors in the DL tunnel on June 26. MIDI was active on the U34 baseline until 08:25.

Figure 9: Data of the four temperature/humidity sensors in the DL tunnel on June 27. MIDI was active on the U23 baseline from 01:20 until 07:30.

Figure 10: Data of the four temperature/humidity sensors in the DL tunnel on June 28. MIDI was active on the U34 baseline from 04:50 until 09:50 and on the U23 baseline from 23:50.
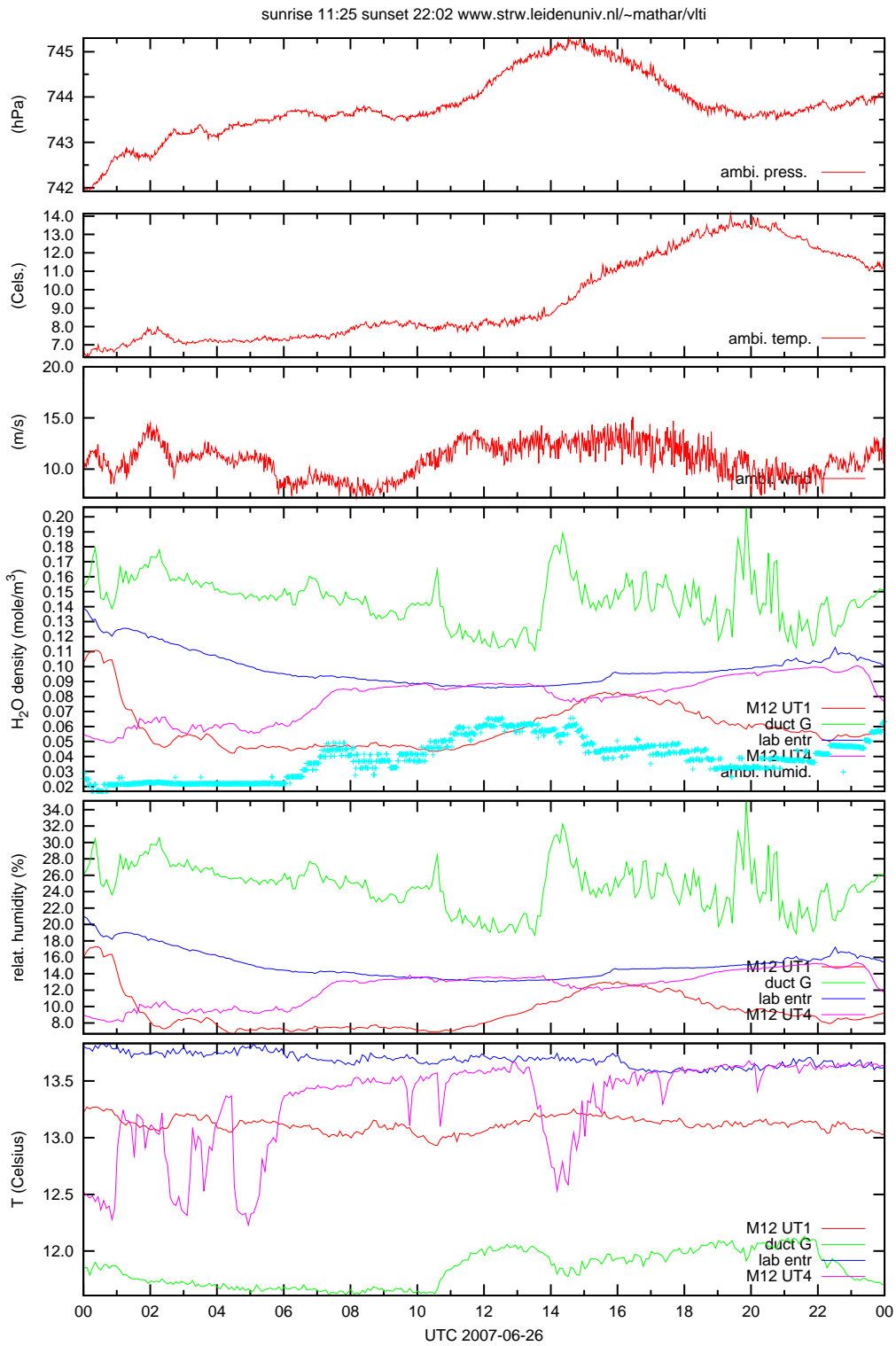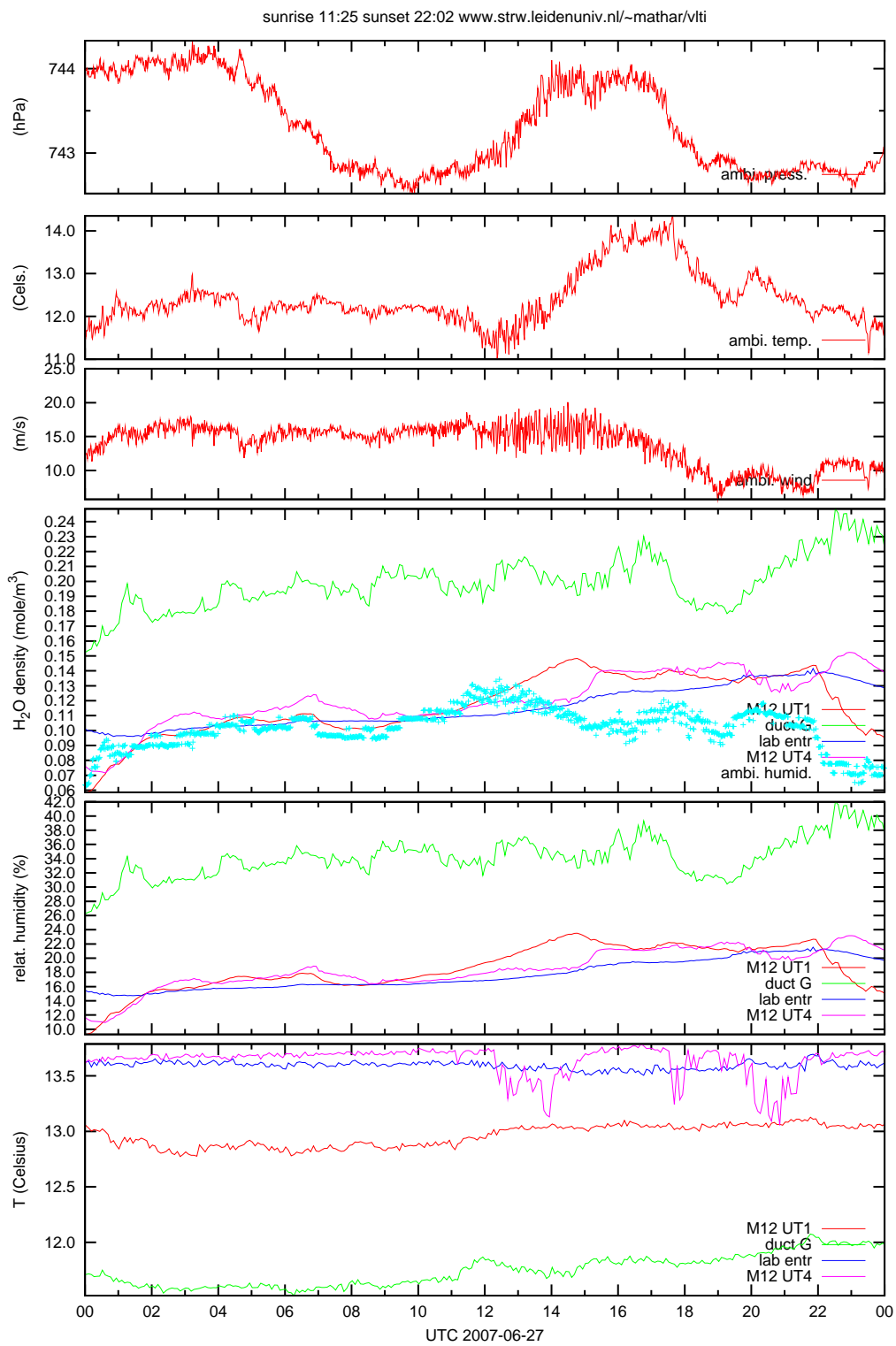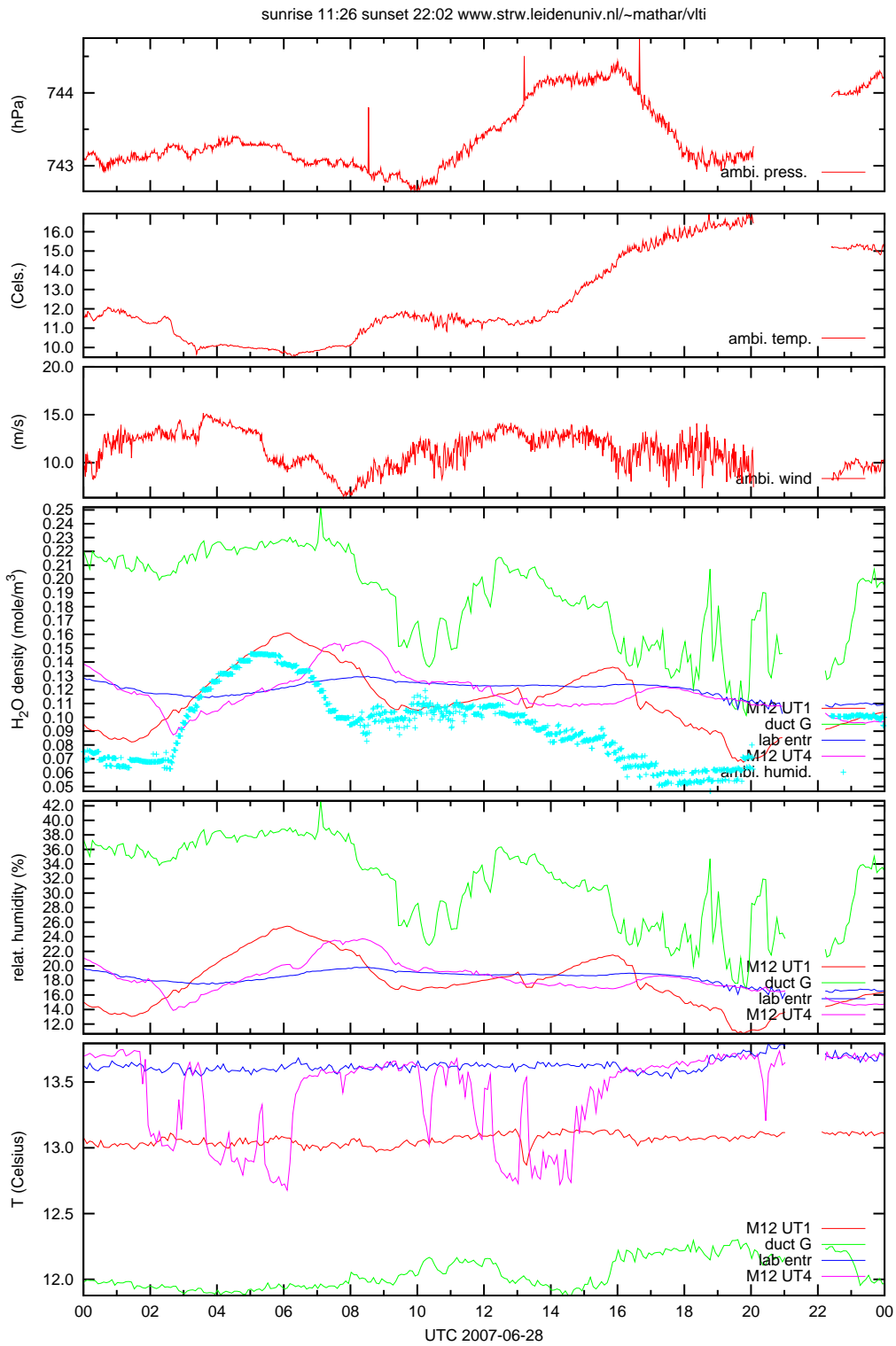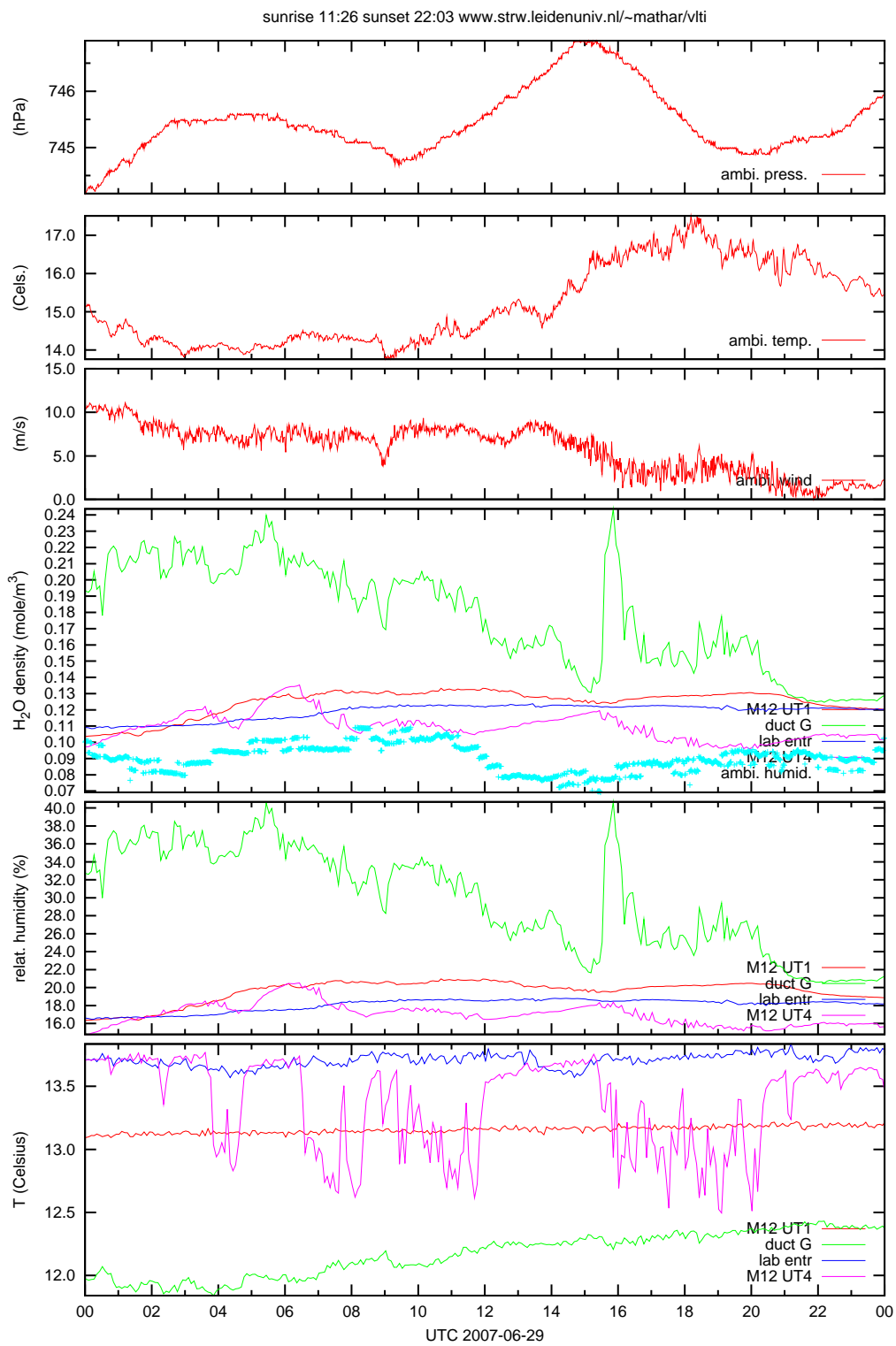
Figure 11: Data of the four temperature/humidity sensors in the DL tunnel on June 29. MIDI was active on the U23 baseline until 08:30.

2.3   Humidity Correction

The LI-COR humidity densities measured from 27 Jun 20:00 on (Lfile6–Lfile10, in the tunnel and in the VST) as shown at the end of Figure 4 up to Figure 7 are approximately a factor of 2.5 too large. The reason is unknown.[1] The overestimation of the water density has as a consequence that the CO$_2$ densities become roughly 10% too low. This "anti-correlation" is a correction to the fact that the CO$_2$ and H$_2$O bands do not provide completely separate information on the two molecular species but do overlap; this software correction is build into the LI-COR software [4].

2.3.1   Magnitude

Supposed an ad-hoc correction to the LI-COR data taken in the tunnel and on the VST is in order, the best linear fit to map the LI-COR absolute humidity back to those of the alternative devices is given in Fig. 12.
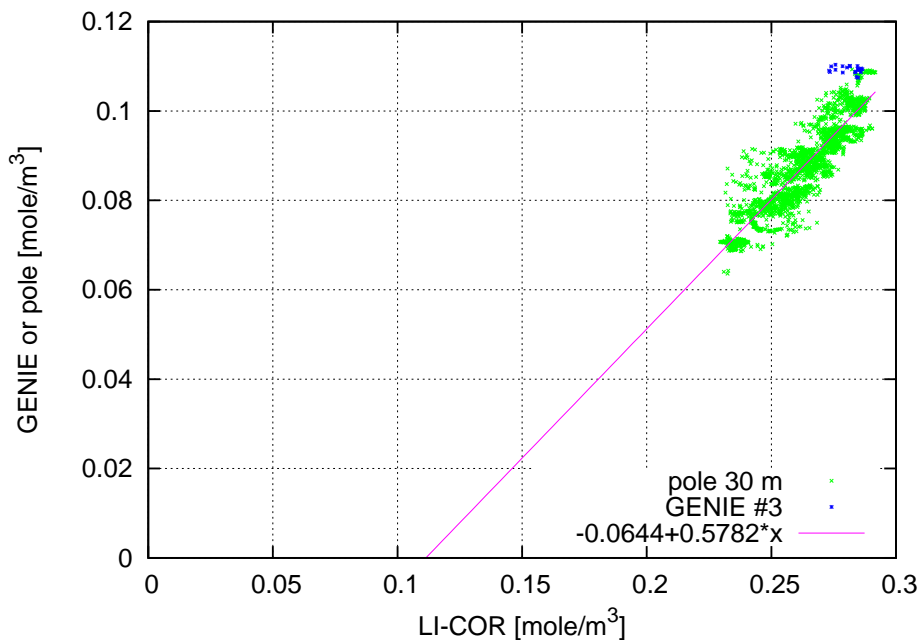

Figure 12: The number densities measured with LI-COR in the tunnel and on the VST are correlated with the GENIE data and with the weather pole data. This paraphrases Figs. 5–7.

Though the relation between the raw absorptance and the number density computed by the software is slightly nonlinear (Fig. 13), this still implies that the water absorptances for the measurements in tunnel and VST had been too large by a factor of ≈ 2.

One may also ask whether the measurements of the GENIE sensors are compatible with those of the weather pole. The GENIE sensors installation report [2] tells us that data had been taken at a common

---

[1]More accurately speaking, the transmission in the water spectral channel rose roughly by a spurious 1 percent. The data produced by the instrument are mutually consistent with the calibration data of the manufacturer. An error of having unintentionally changed instrument parameters from the GUI during the campaign is therefore unlikely. There is no evidence that the LI-COR electronics or mechanics of the probe had been damaged while moving the equipment from the VLTI control building into the VLTI tunnel.
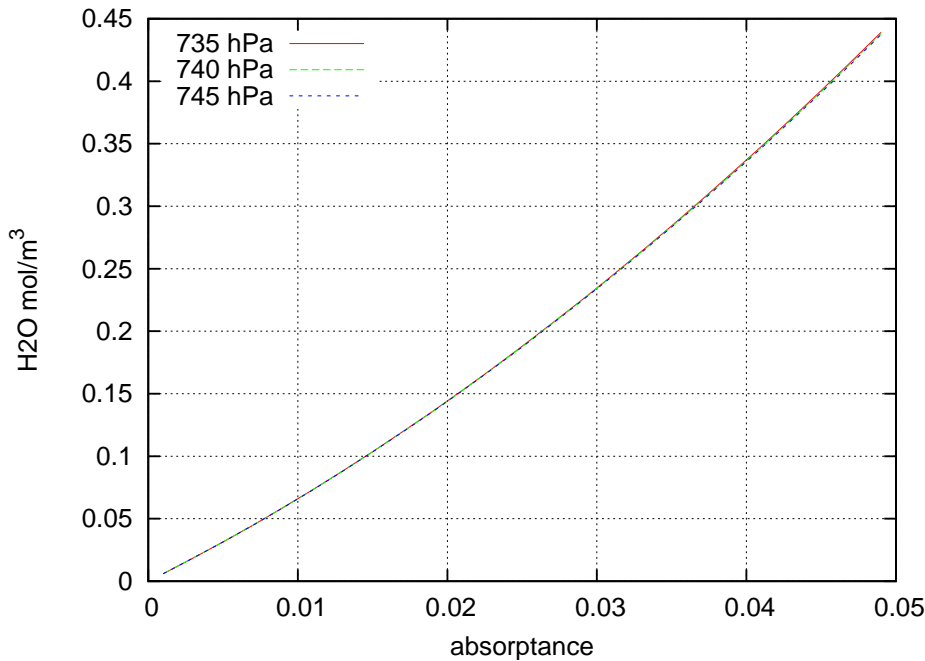
Figure 13: The relation between LI-COR absorptance α_{H2O} in the water band and the number density ρ_{H2O} from the fourth order polynomial calibration curve, [4, 2-13]. There is no constant term in the polynomial, and the coefficients for the linear through fourth power from the calibration certificate of 2006-10-23 are 5.95562×10^3, 4.57481×10^6, and -1.73017×10^8, with a "span" parameter of 1.00284. The result hardly depends on the ambient pressure in the applicable pressure range.

time and place at a height of 2 m at the weather station—which is incompatible with the height of 30 m reported by the web page http://archive.eso.org/eso/ambient-database.html—but we have no further information on quantitative results drawn from this.

2.3.2 Search for Causes

1. The raw data (absorptance column) of the data files are too large for water after moving the instrument to the tunnel, and this bias was also found when the LI-COR instrument was tested back in Leiden on July 20 at water densities near 0.92 mole/m^3. Starting from the raw data, the derived data (number density and mixing ratio) are correct with respect to the calibration parameters and auxiliary inputs (pressures and temperatures). (One finds that the span parameter in the second and third VST file is is slightly different from the parameter in other files, truncated to three significant digits from 1.00284 to 1.00. The impact on the number density and mixing ratio is in the sub-percent range and not relevant. It therefore is unlikely that one of the computer crashes has reset some of the calibration parameters.

2. In Fig. 4, the water channel data are too large immediately after the setup in the tunnel, whereas the carbon dioxide drops by 40 ppmv within an hour. Temperature and CO_2 are correlated, but as Fig. 20 points out, correcting for the temperature reading would even deteriorate (decrease) the CO_2 mixing ratio.

2.4   Recalibrated Data

Conversion of the tunnel and VST Data with the fit suggested in Fig. 12,

$$\rho_{\text{H2O}}^{C} = -0.0644\text{mole} \cdot \text{m}^{-3} + 0.5782\rho_{\text{H2O}} \tag{1}$$

transforms Figs. 2–7 to Figs. 14–26. The purple color for the transformed data indicates

- the fit (1) has been applied to re-calibrate the water molecular number density on a point-by-point basis,

- that the carbon dioxide level has been re-calculated taking into account this change in water absorptance, plus taking the temperature not from the LI-COR sensor inside its electronic box but from the external (weather tower or GENIE, respectively) sensors, linearly interpolated on their sparse time axis sampled at once per minute (weather tower) or once per five minutes (GENIE).

A comparison between the carbon dioxide content in Fig. 14 and the one in Fig. 26 reveals that the absolute data are still inconsistent: the 375 ppm of the first outdoor data sets are expected,[2] but there is no reason for the level to drop to a mean of 350 five days later. A reduction of the CO$_2$ mixing ratio in the tunnel might be expected by estimating the dilution associated with LN evaporation from other instruments, see Sect. 6.3.4 in [13]. Putting numbers on the size of the effect is difficult by merely calculational means given the lack of further input data, so the LI-COR CO$_2$ measurements are as close as we can get to estimates of the fluctuations.

---

[2] The seasonal change of the mixing ratio is small south of the equator [10, 23]. Any CO$_2$ exhaust by fuel burning for air conditioning of the telescopes or related to the base camp energy consumption is not very relevant due to the Northern wind direction.
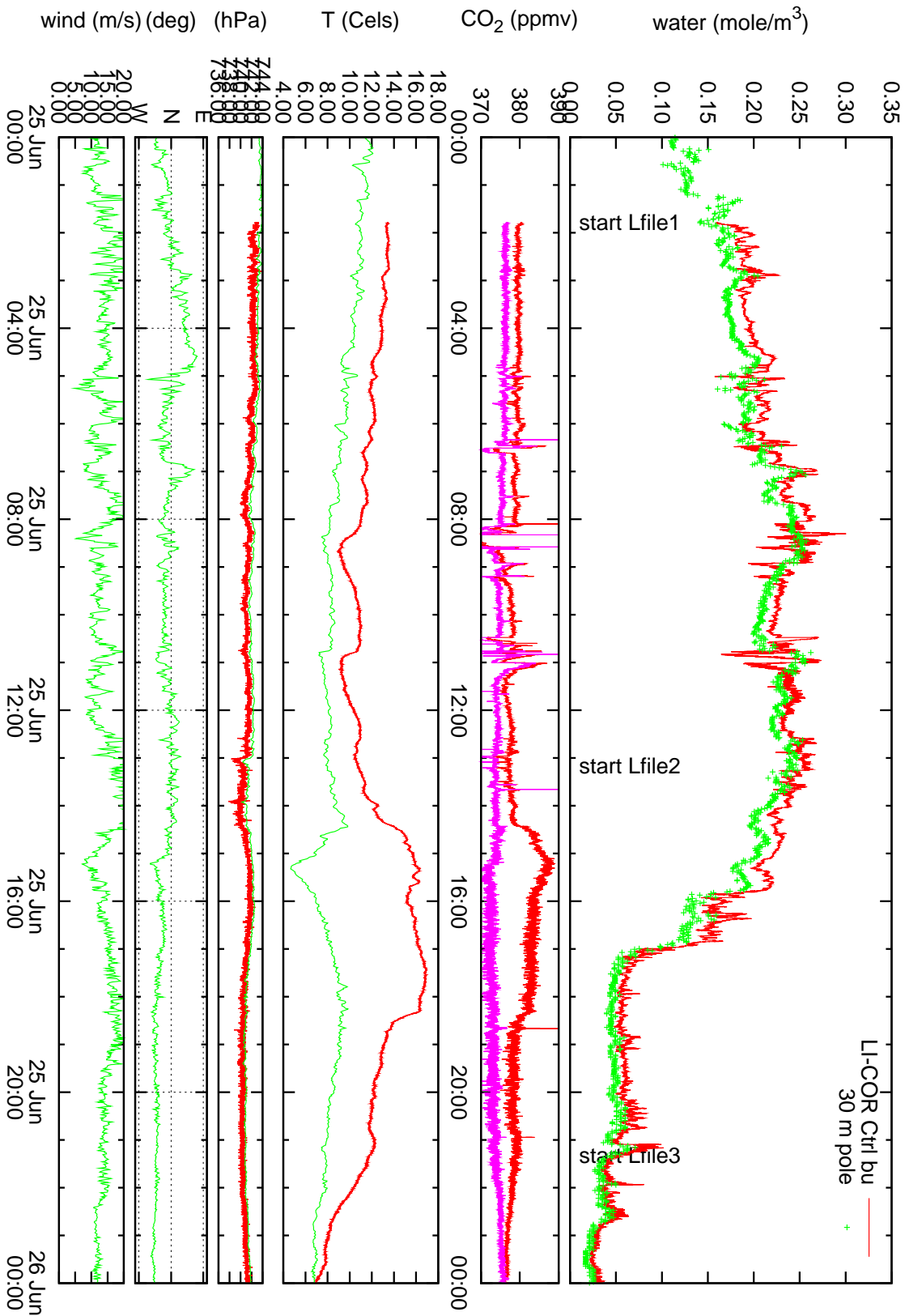
Figure 14: LI-COR water number density near the VLTI control building roof in comparison with weather pole data for the first 24 hrs of data. Continued in Fig. 17.

Figure 15: A 4 hours subsection of Fig. 14, and also input data to Fig. 29 (VLTI Control building).

Figure 16: A 4 hours section of Fig. 14 and also input data to Fig. 30 (VLTI Control Building).
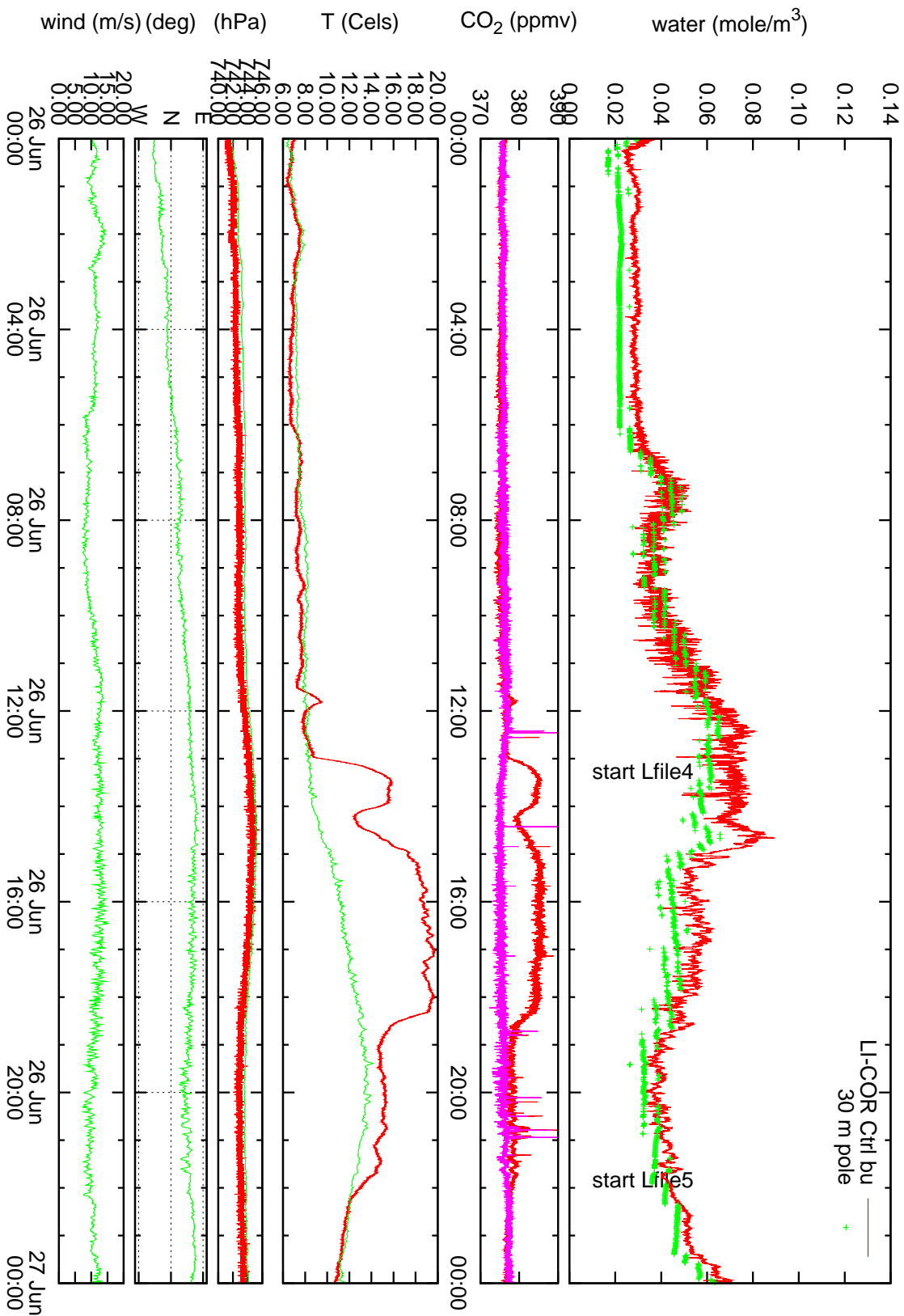
Figure 17: Water number density near the VLTI control building roof for the second 24 hrs of data. Continued in Fig. 20.
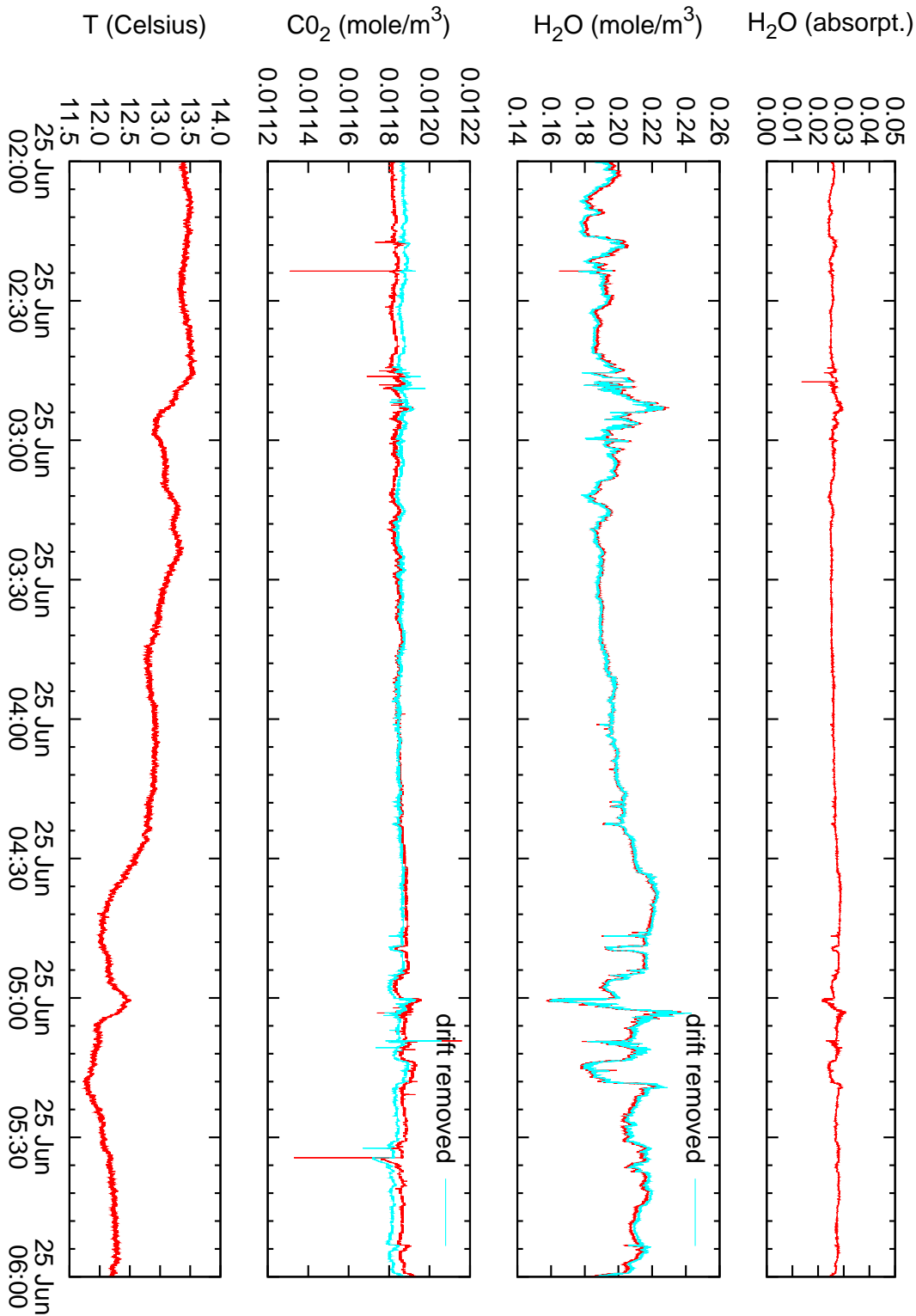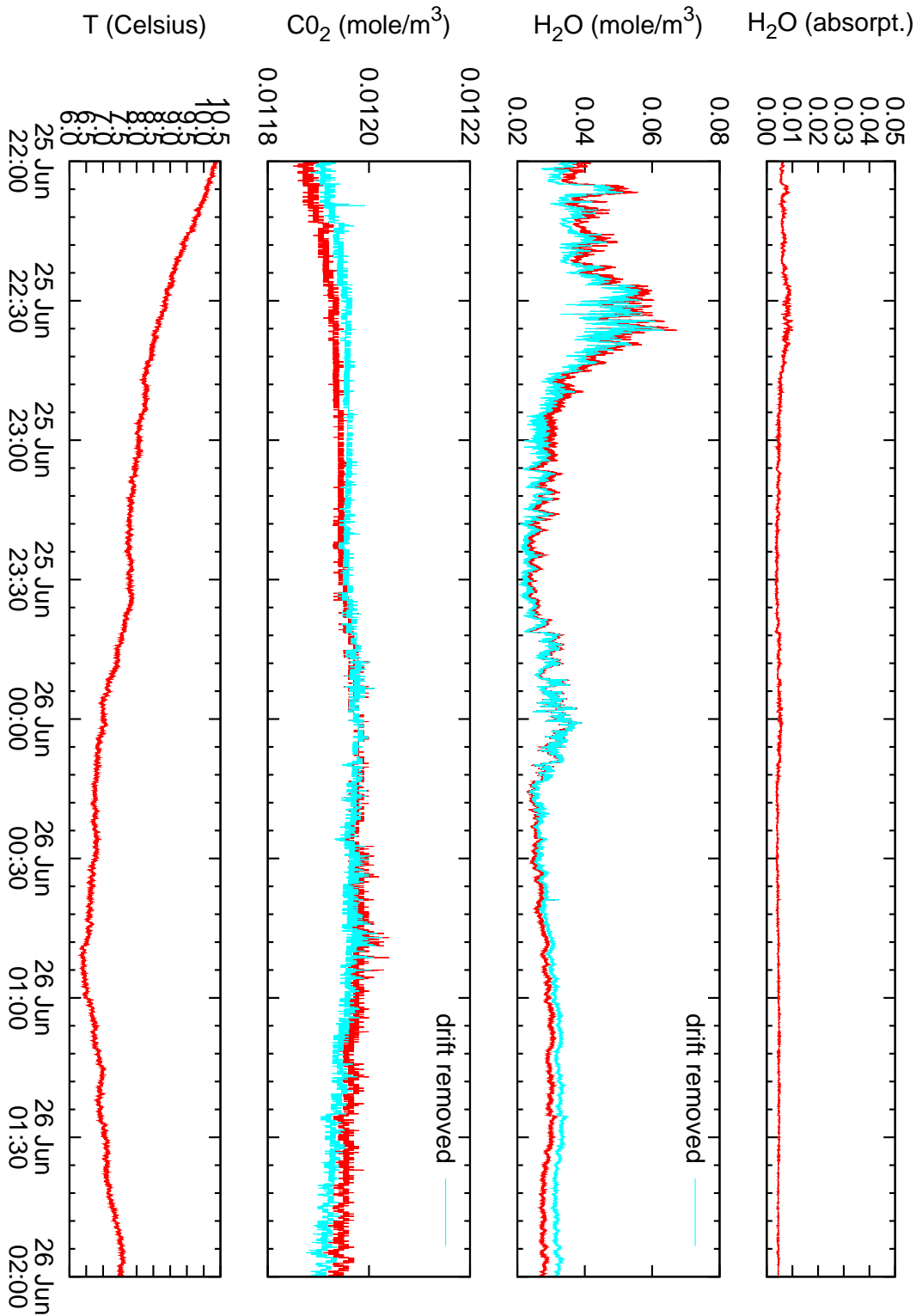
Figure 18:   A 4 hours subsection of Figs. 14 and 17 and also input data to Fig. 31 (VLTI Control building).
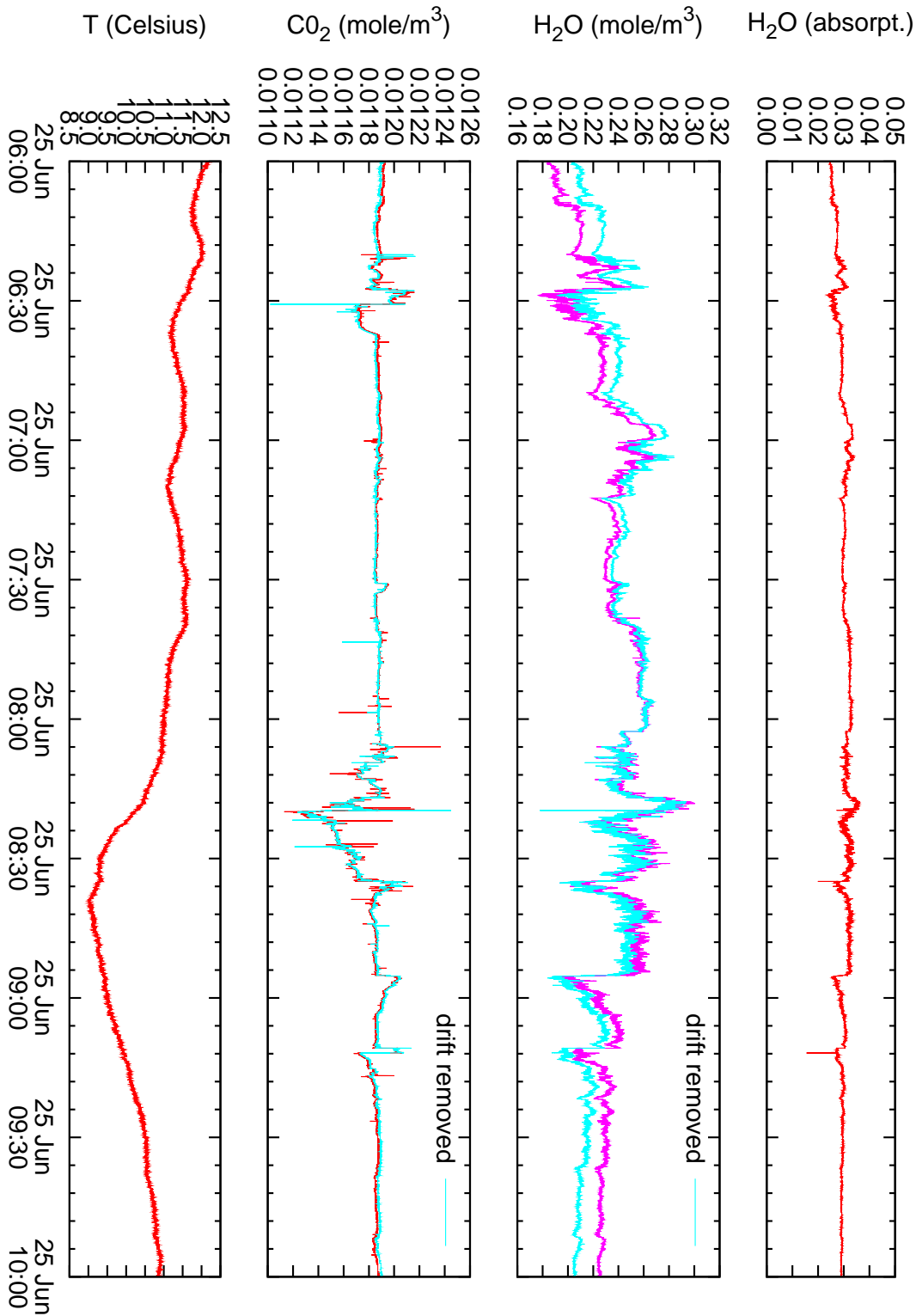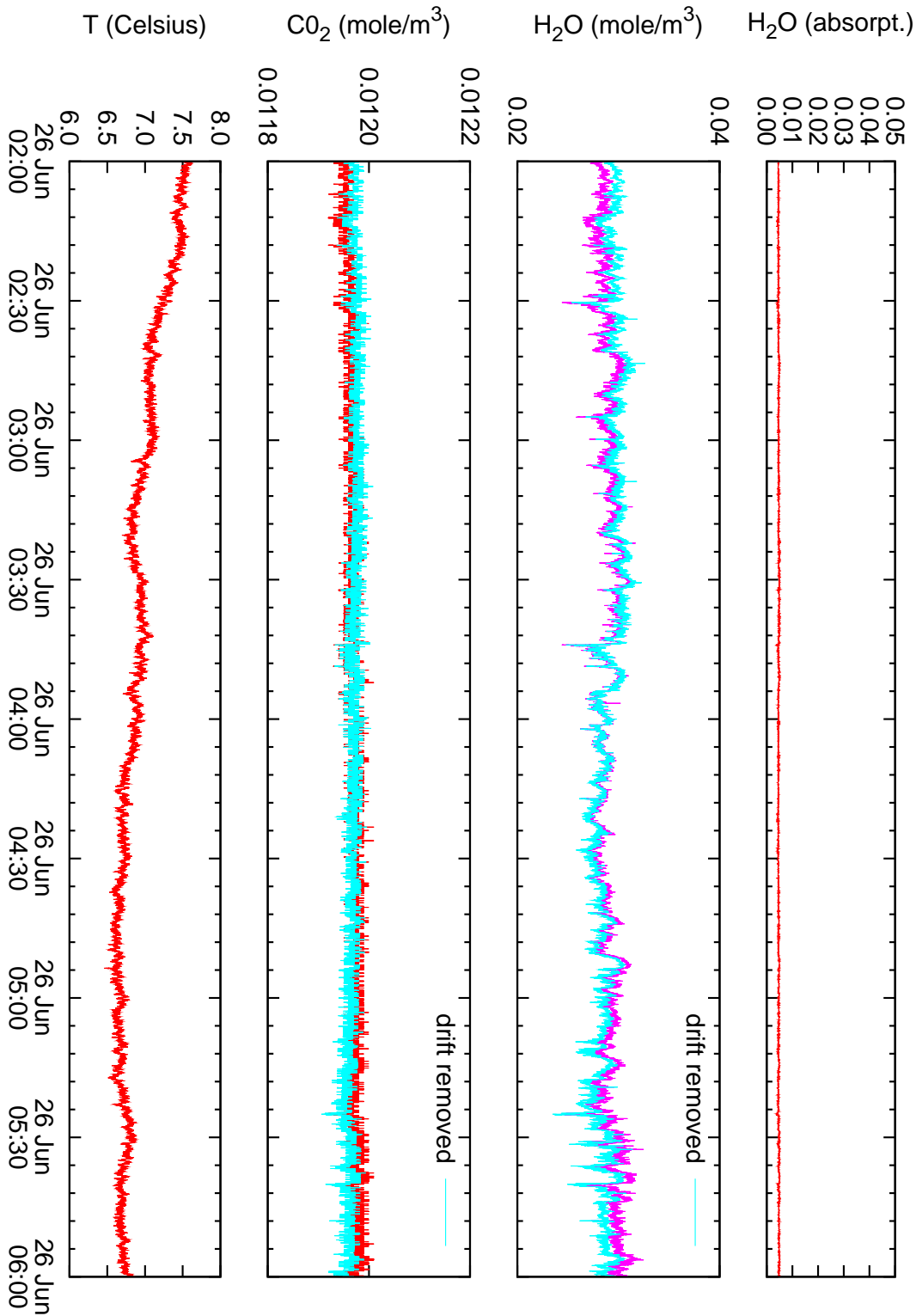
Figure 19: 4 hours subsection of Fig. 17 and also input data to Fig. 32 (VLTI Control building).
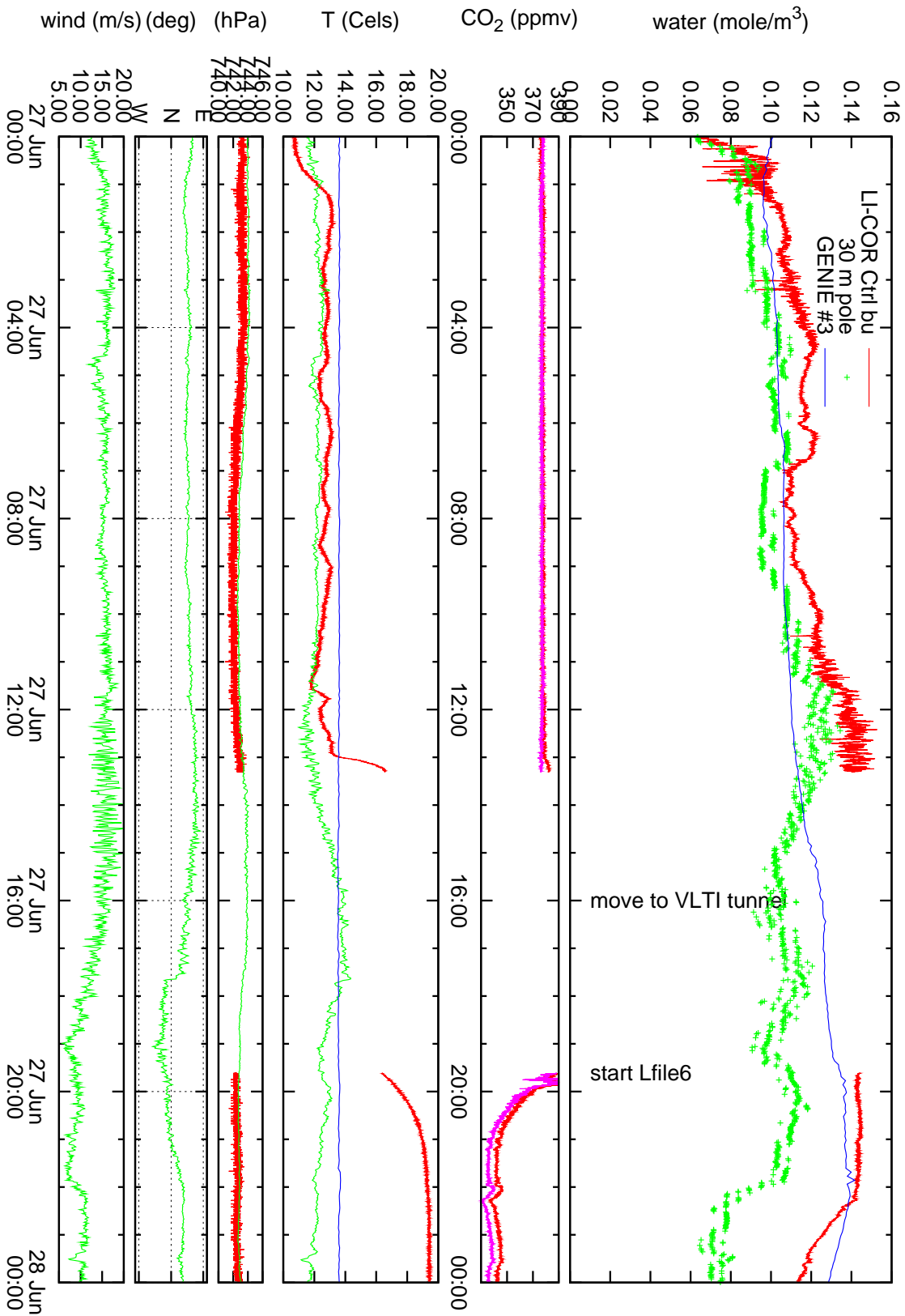
Figure 20: Water number density near the VLTI control building roof for the third 24 hrs of data, the last 4 hrs in the VLTI tunnel including the correction (1). Continued in Fig. 22.
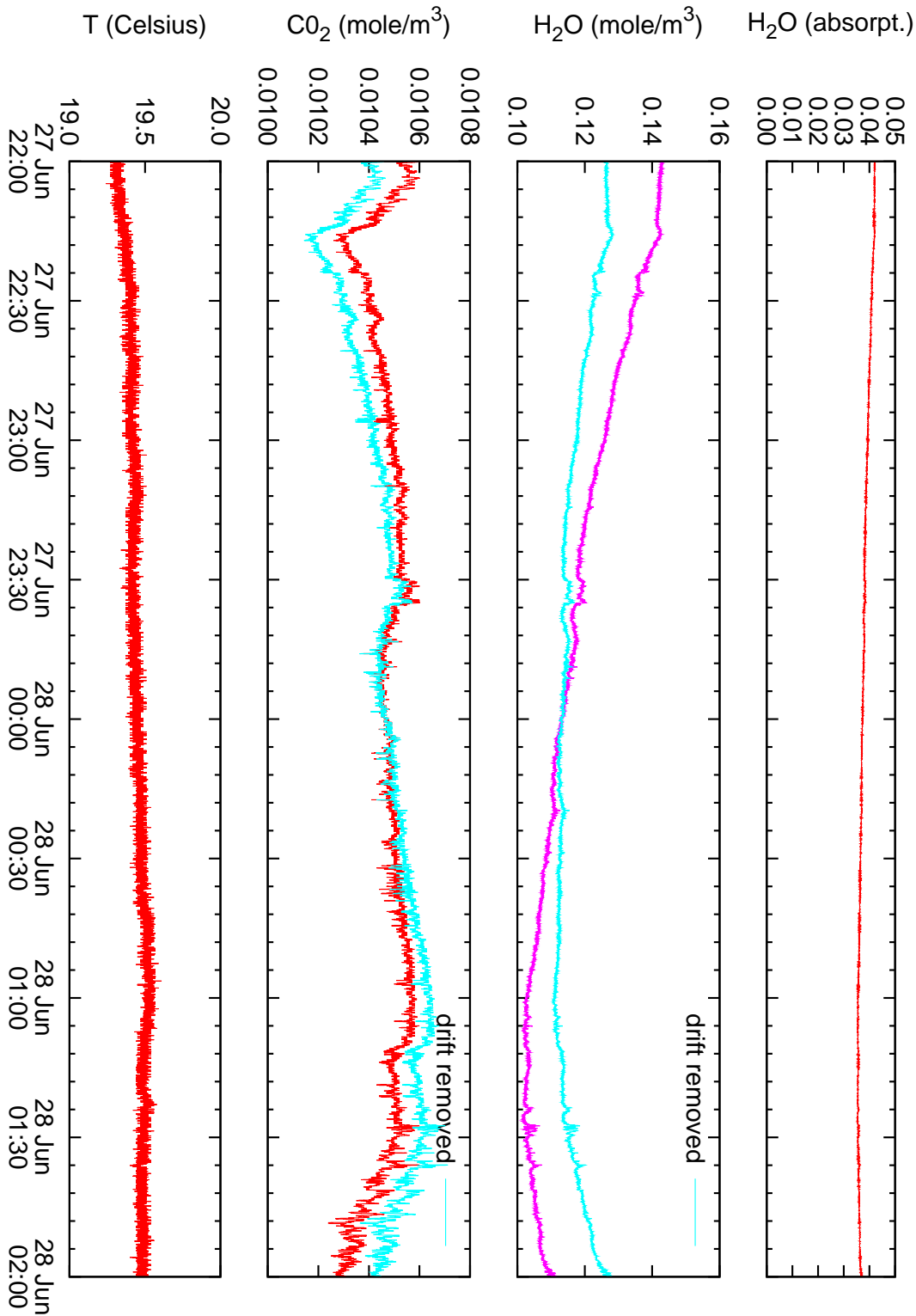
Figure 21:   4 hours subsection of Fig. 20 and 22 and also input data to Fig. 37 (tunnel).
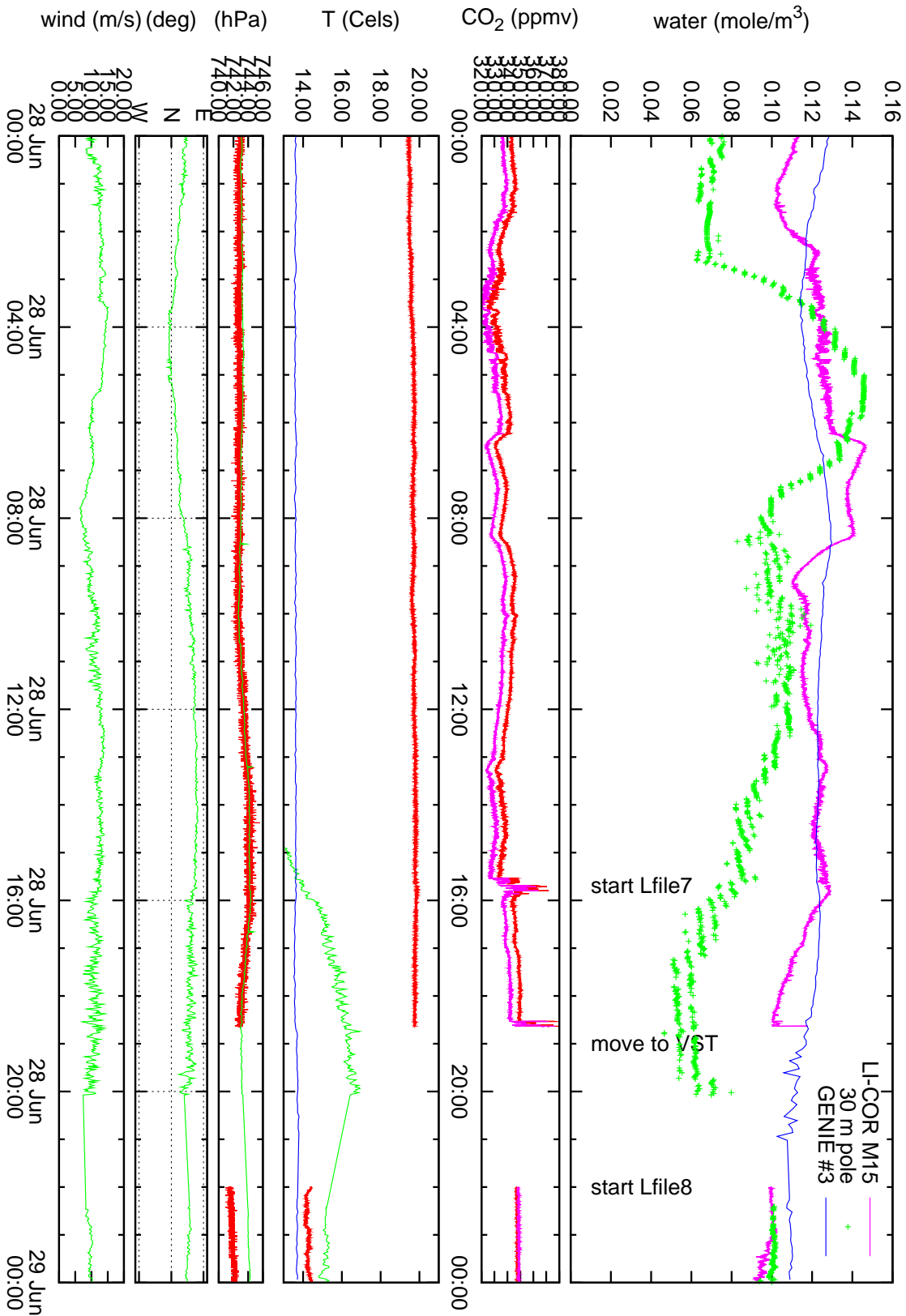
Figure 22: Water number density in the VLTI tunnel near the entrance to the VLTI laboratory. Red the LI-COR output including the correction (1), blue the GENIE humidity (converted from relative to absolute using the GENIE temperature), and green the humidity at the weather pole. Continued in Fig. 25.

Figure 23:   4 hours subsection of Fig. 22 and also input data to Fig. 38 (tunnel).
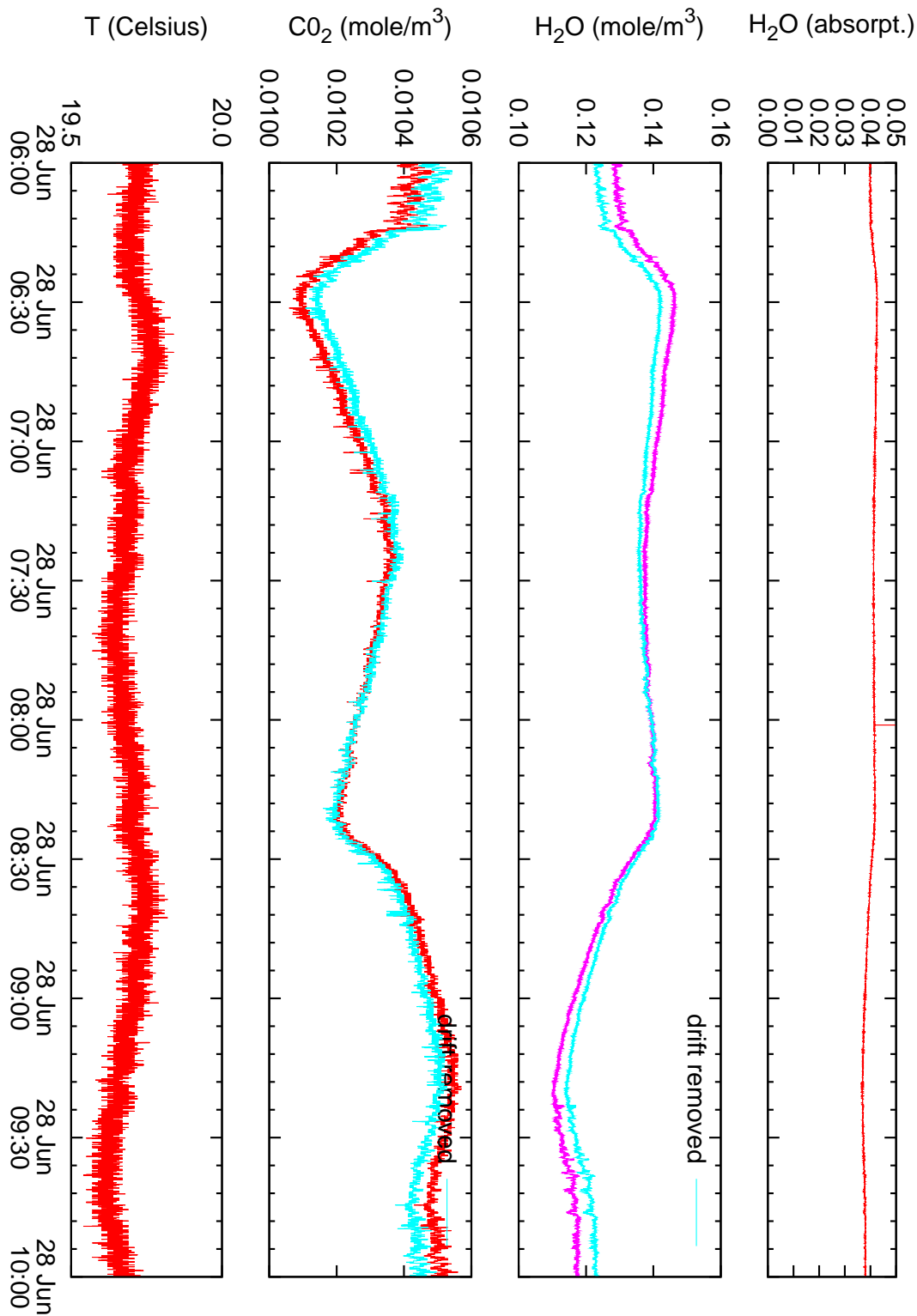
Figure 24: 4 hours subsection of Fig. 22 and also input data to Fig. 39 (tunnel).

Figure 25: Water number density in the VST dome after the correction (1), and from the ambient data server. Continued in Fig. 26.

Figure 26:   Water number density in the VST dome after the correction (1) and from the ambient data server until the end of the campaign.

Figure 27: 4 hours subsection of Fig. 26 and also input data to Fig. 44 (VST).

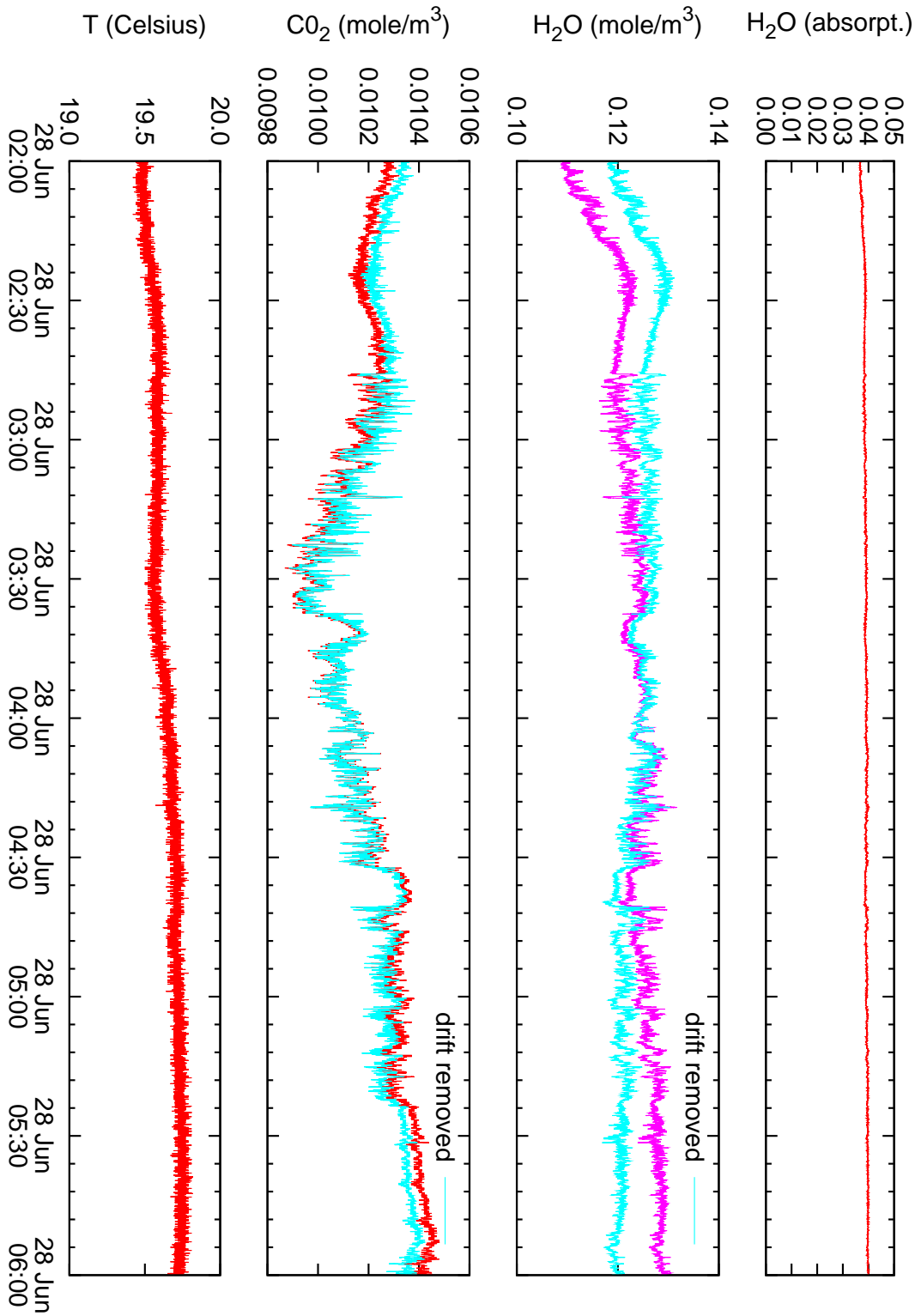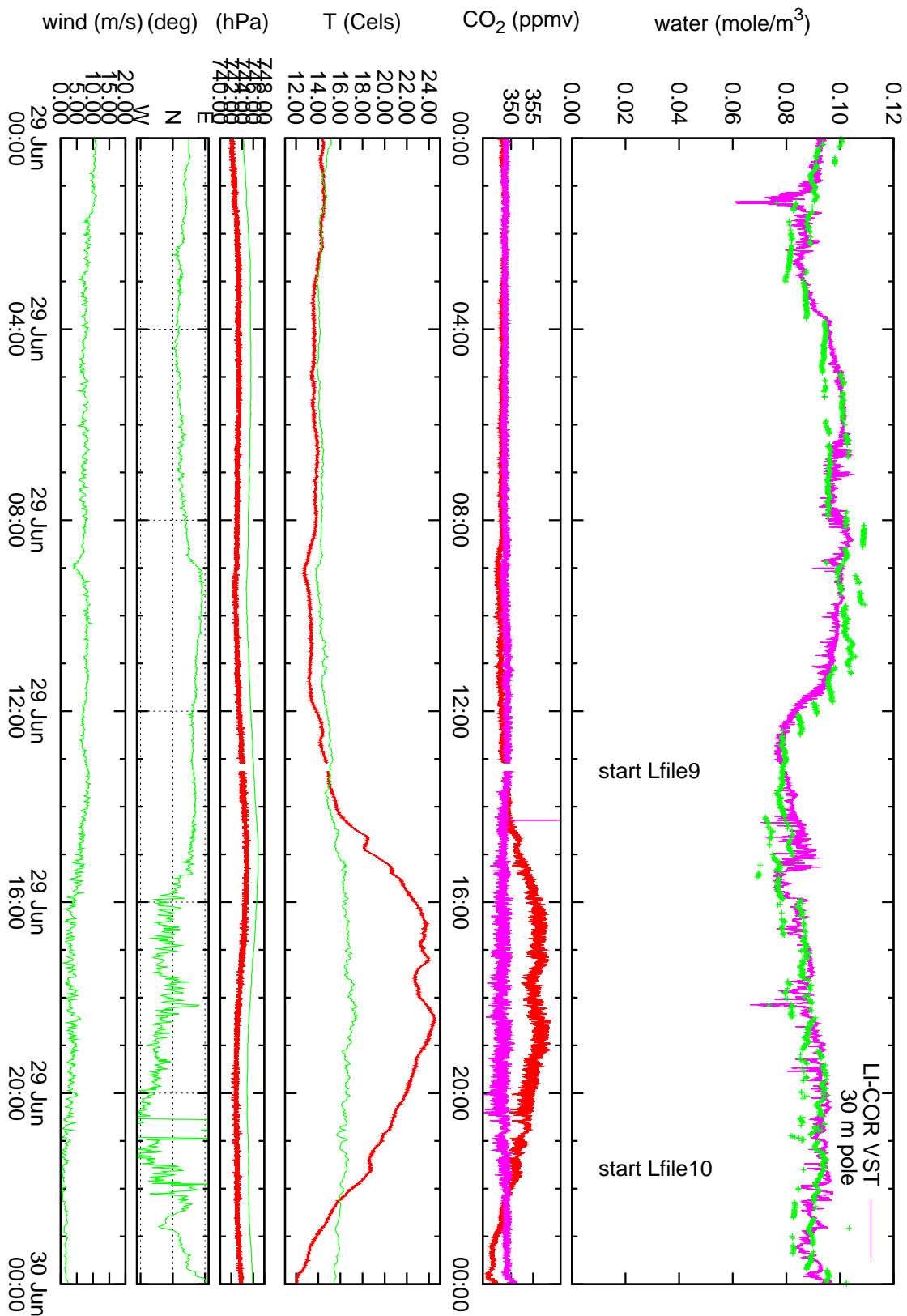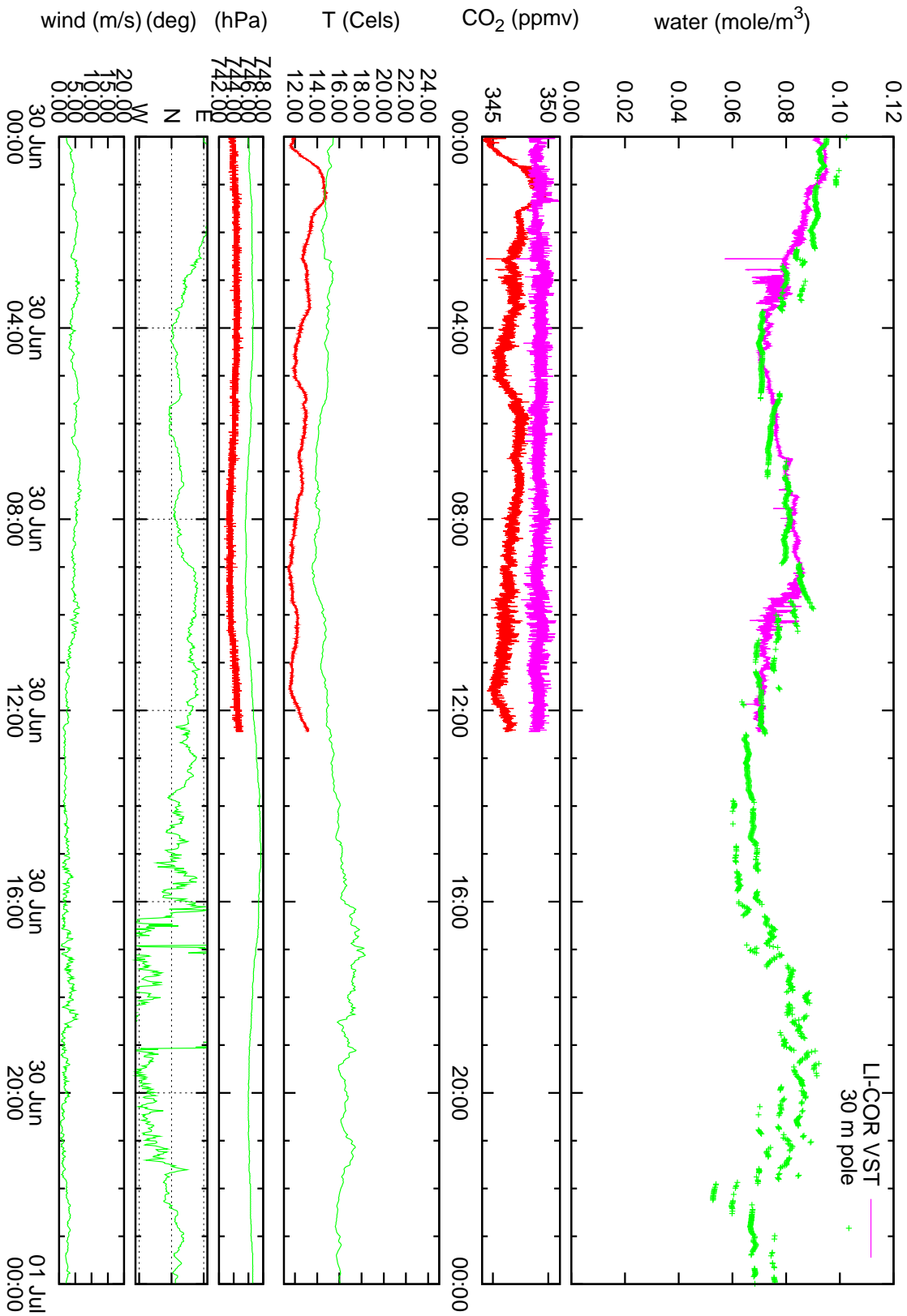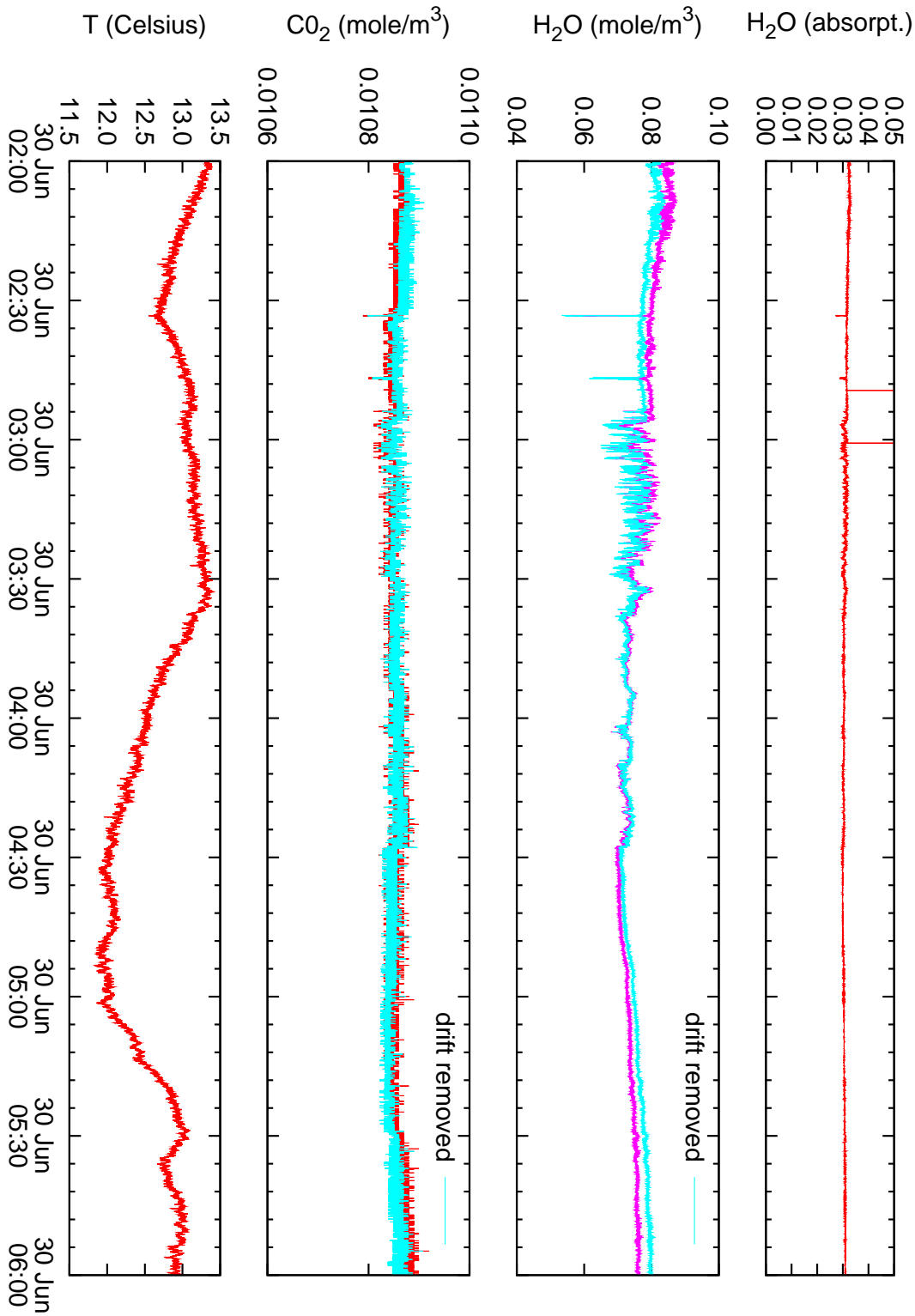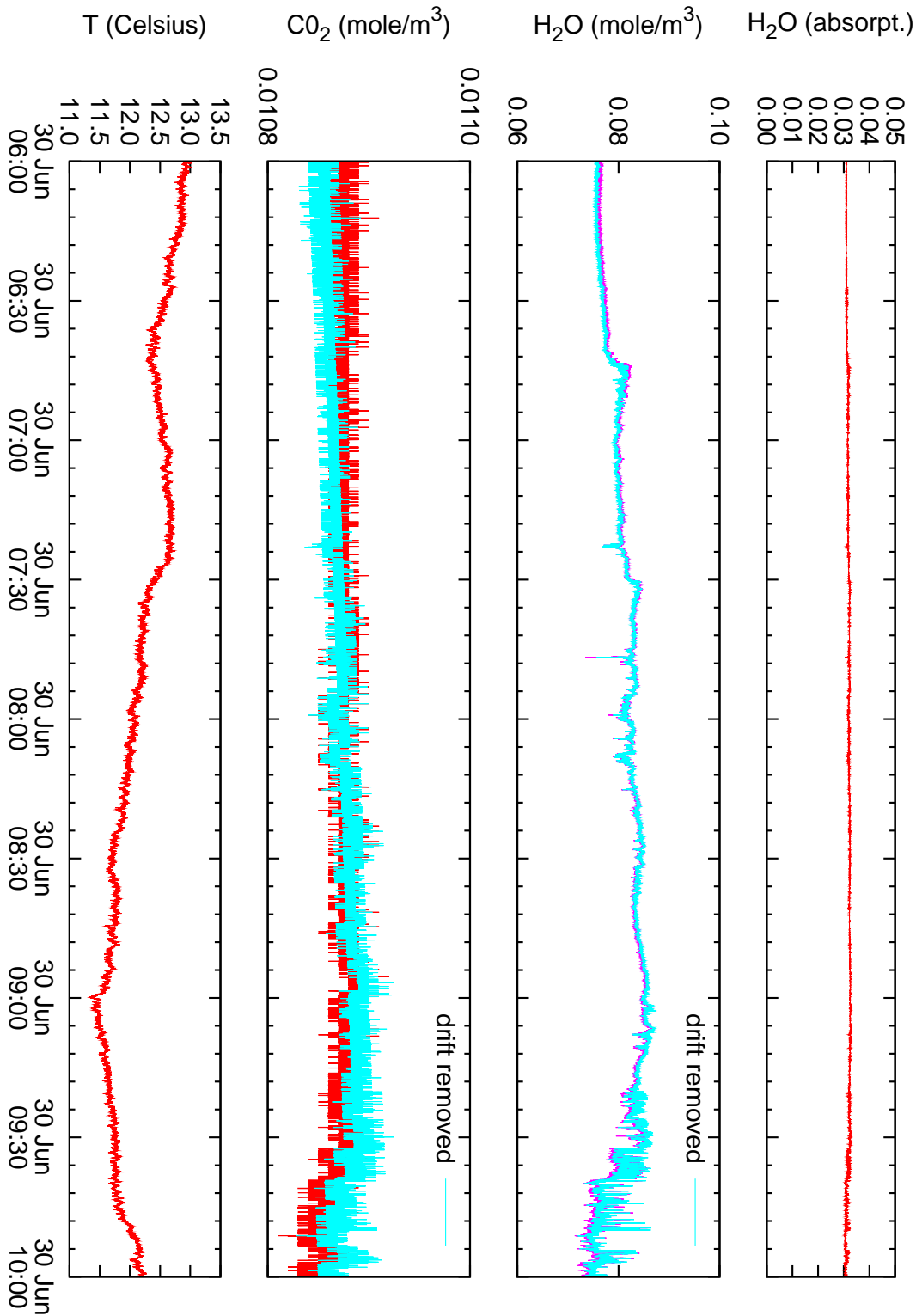Figure 28: 4 hours subsection of Fig. 26 and also input data to Fig. 45 (VST).

3   SPECTRA, AUTOCORRELATIONS

3.1   Near VLTI Control building

Power spectral densities sampled over time intervals of 4 hours for the first site, outside the VLTI control building, shown in Fig. 2, are presented in Fig. 29–36. The 2-sided PDFs of functions f are defined as

$$\mathrm{PDF}_f(\nu) = \frac{\left| \int_0^T f(t) e^{2\pi i \nu t} dt \right|^2}{T}, \tag{2}$$

where $T = N\Delta t$ is the full time interval (not the temperature) of the sampling. This is defined on both sides of the frequency axis; one will also find this in the literature multiplied by 2 to pile up all the energy on the positive frequencies,[3] but this has obvious disadvantages if one wants to build auto-correlations or structure functions.

The monitoring interval of 4 hours for each chunk is arbitrary to a large extent. It is long enough to keep the number of spectra to be plotted in check (17 of these spectra are extracted in this script, intervals of 2 hours would easily have doubled that count), but smaller than time constants of global weather parameters. Since we will finally be more interested in night time data, and these have a bias toward being calmer because energy injection by the sun into the atmosphere is missing, we show only spectra obtained during the night.

If one removes the long-time drift by subtraction of a one-parametric slope (App. 5.4, Version B), one ends up with the light blue lines. In some of the spectra one will find knees in the slopes of power laws close to 5 Hz. These might be caused by having set an intermediate filter bandwidth in the LI-COR outputs (page 3-29 in [4], configuration file parameter `BW` in the `OUTPUTS` section) to 5 Hz.

The inverse Fourier transform with the Wiener-Khinchin Theorem transforms these into auto-correlation functions. The structure function

$$\mathcal{D}_f(\Delta t) = \langle (f(t + \Delta t) - f(t))^2 \rangle \tag{3}$$

follows immediately by computing twice the difference of the auto-correlation at time zero and later on.

A Kolmogorov power density function has an exponent of $8/3 \approx 2.7$, variable β in Appendix 5.2. Following the standard theory, this is reduced to an exponent of $5/3 \approx 1.7$ for the 2D structure after integration over the line of sight of a telescope pupil, see page 293 in [19] and Section 5.2 in [16].

---

[3]. . . actually this ambiguity is hardly ever documented. . .
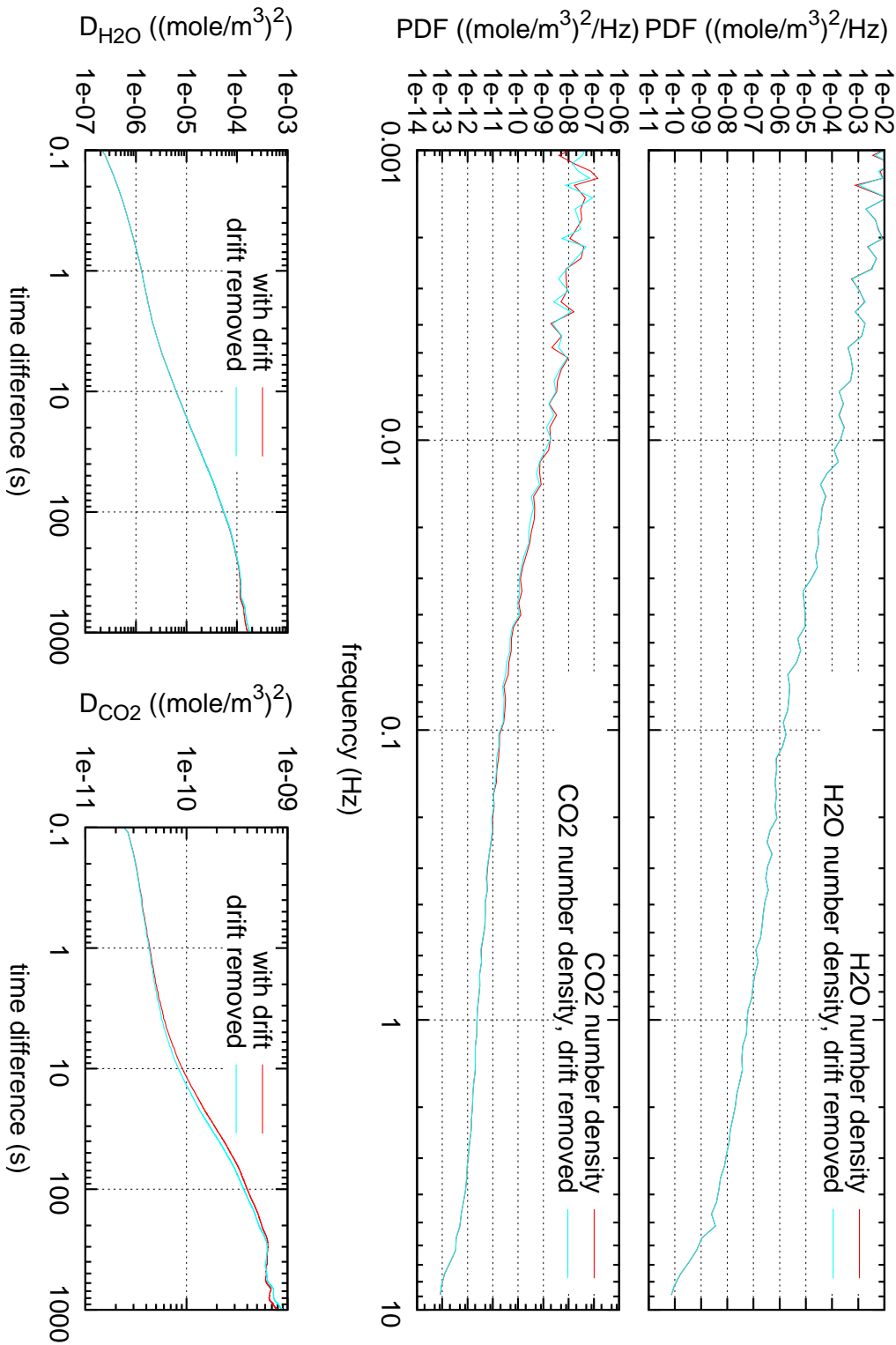
Figure 29: PDF of water and CO_2 number densities near the VLTI control building roof top over four hours. The input data are in Fig. 15. Average wind velocity 14.5 m/s. Average humidity 0.182 mole/m^3.
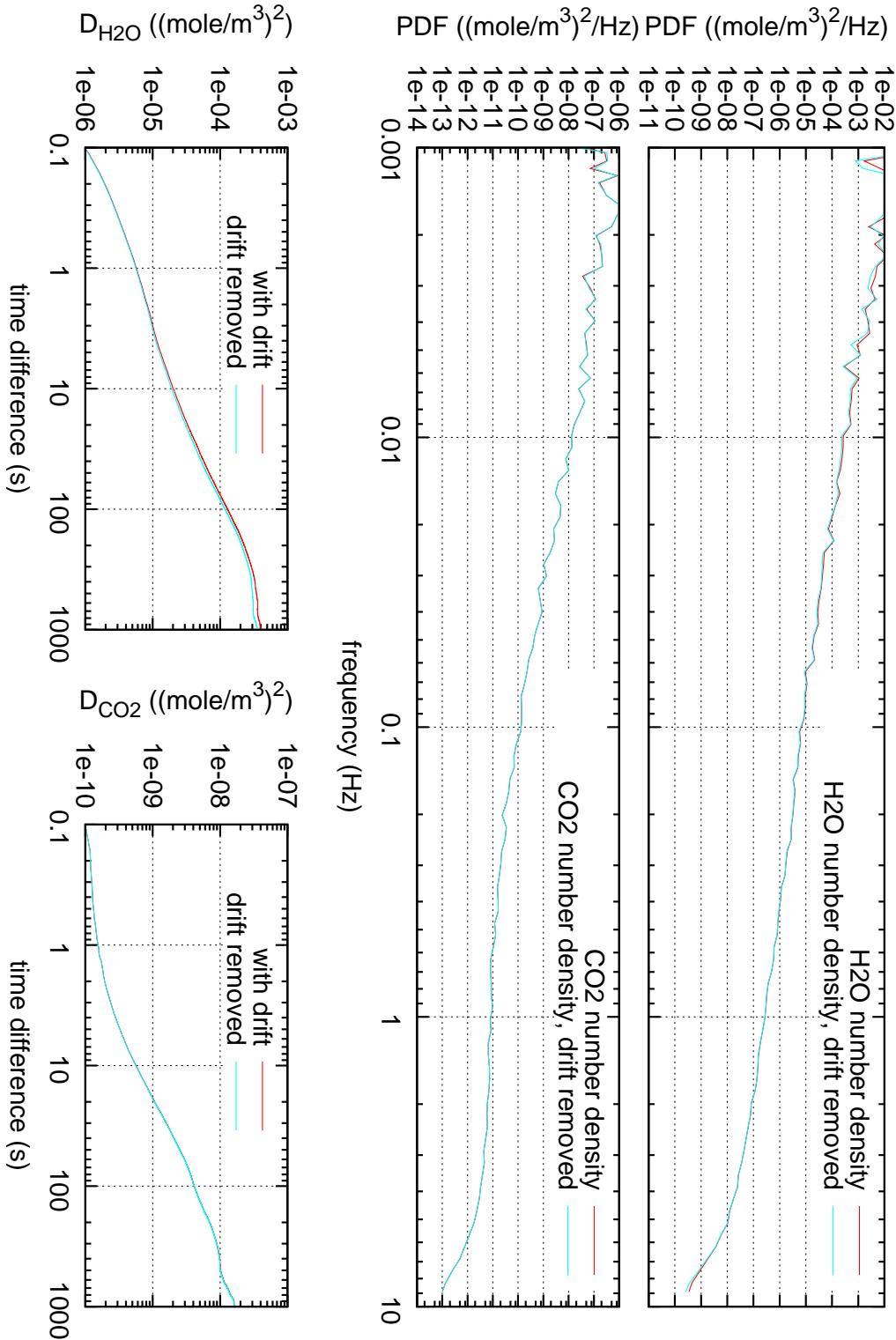
Figure 30: PDFs of water and CO₂ number densities near the VLTI control building over four hours. The input data are in Fig. 16. Average wind velocity 12.9 m/s. Average humidity 0.223 mole/m³.
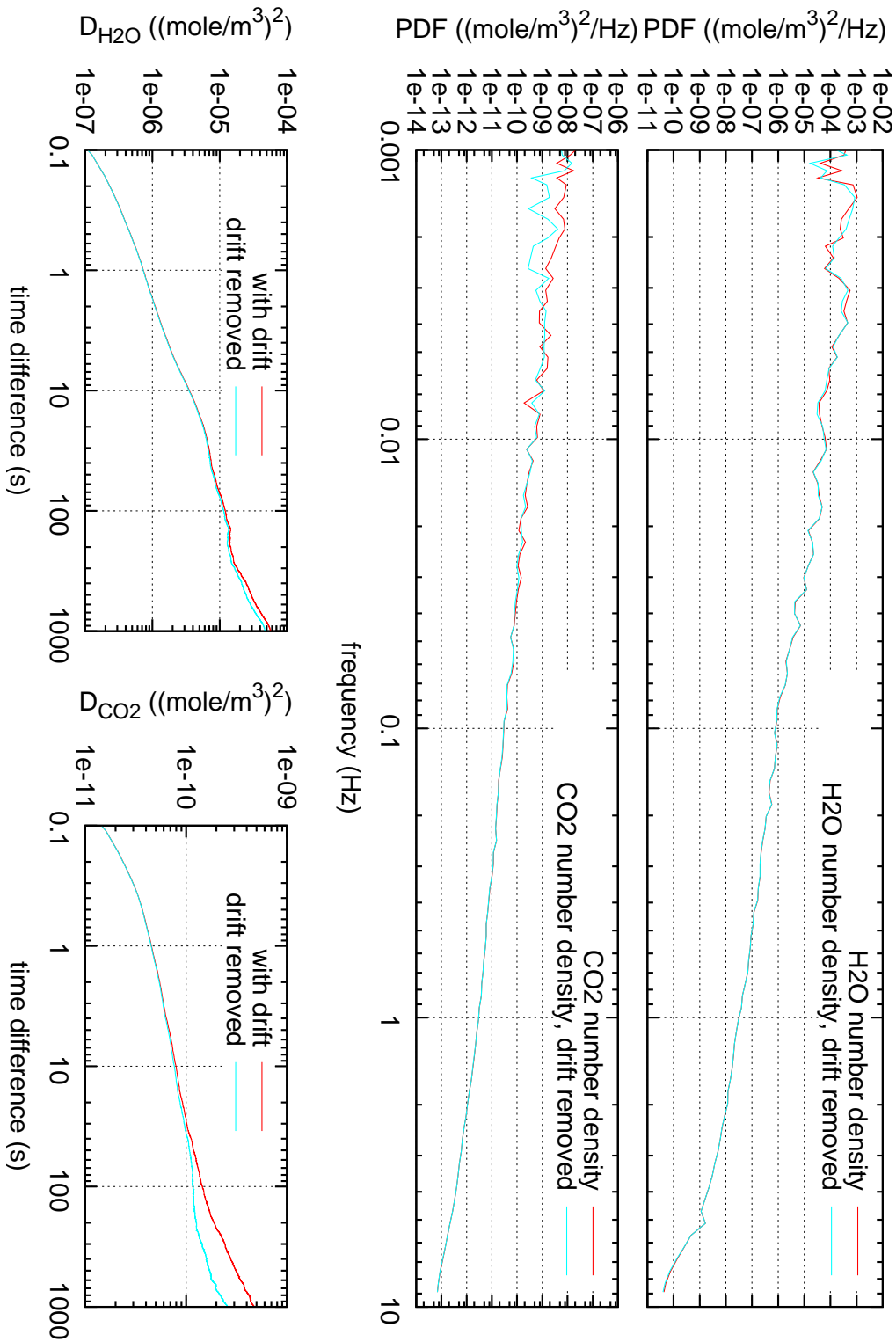
Figure 31: PDFs of water and CO_2 number densities near the VLTI control building roof top over four hours. The input data are in Fig. 18. Average wind velocity 11.5 m/s. Average humidity 0.024 mole/m^3.
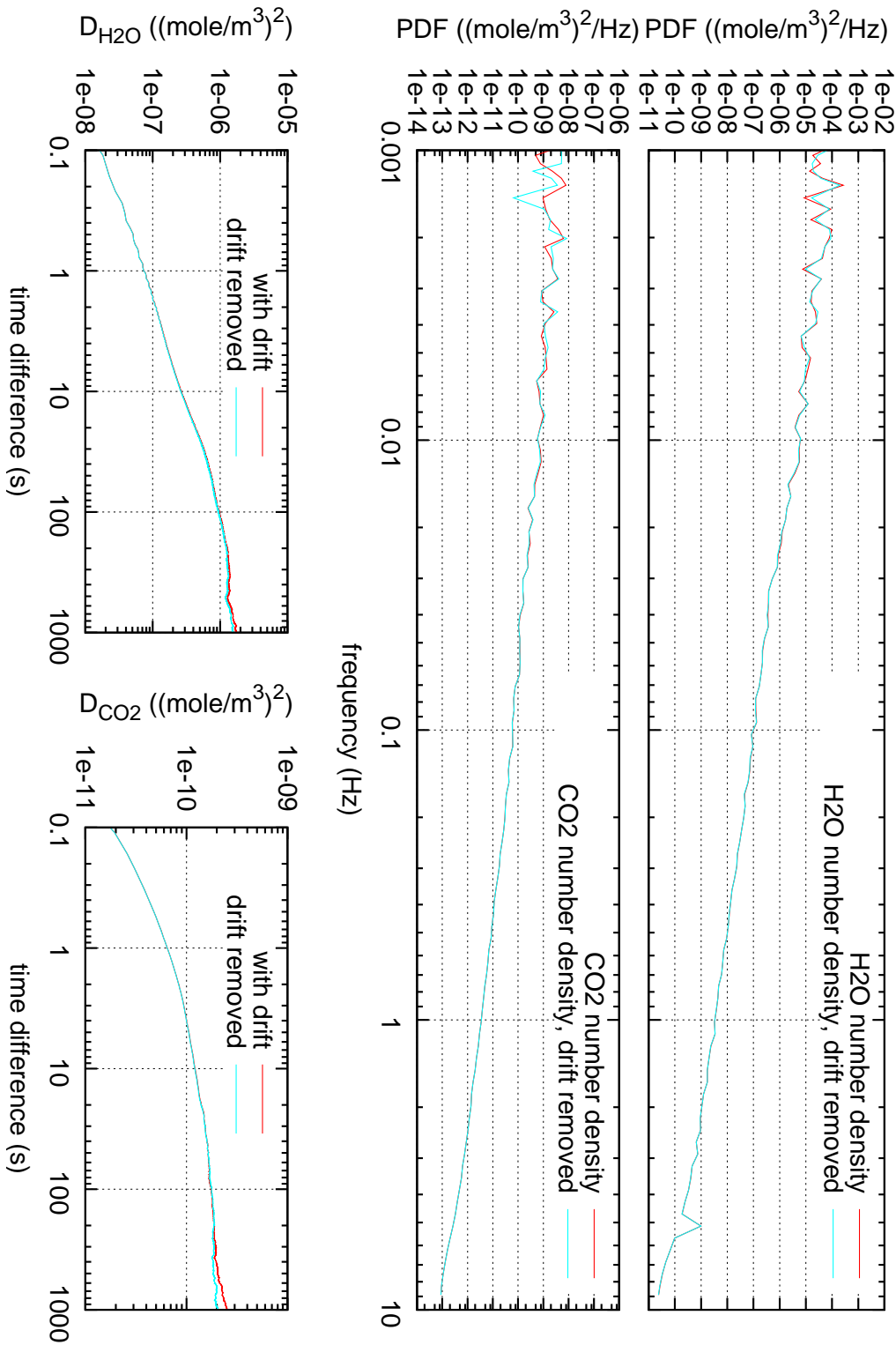
Figure 32:   PDFs of water and CO$_2$ number densities near the VLTI control building roof top over four hours. The input data are in Fig. 19. Average wind velocity 11.1 m/s. Average humidity 0.022 mole/m^3.
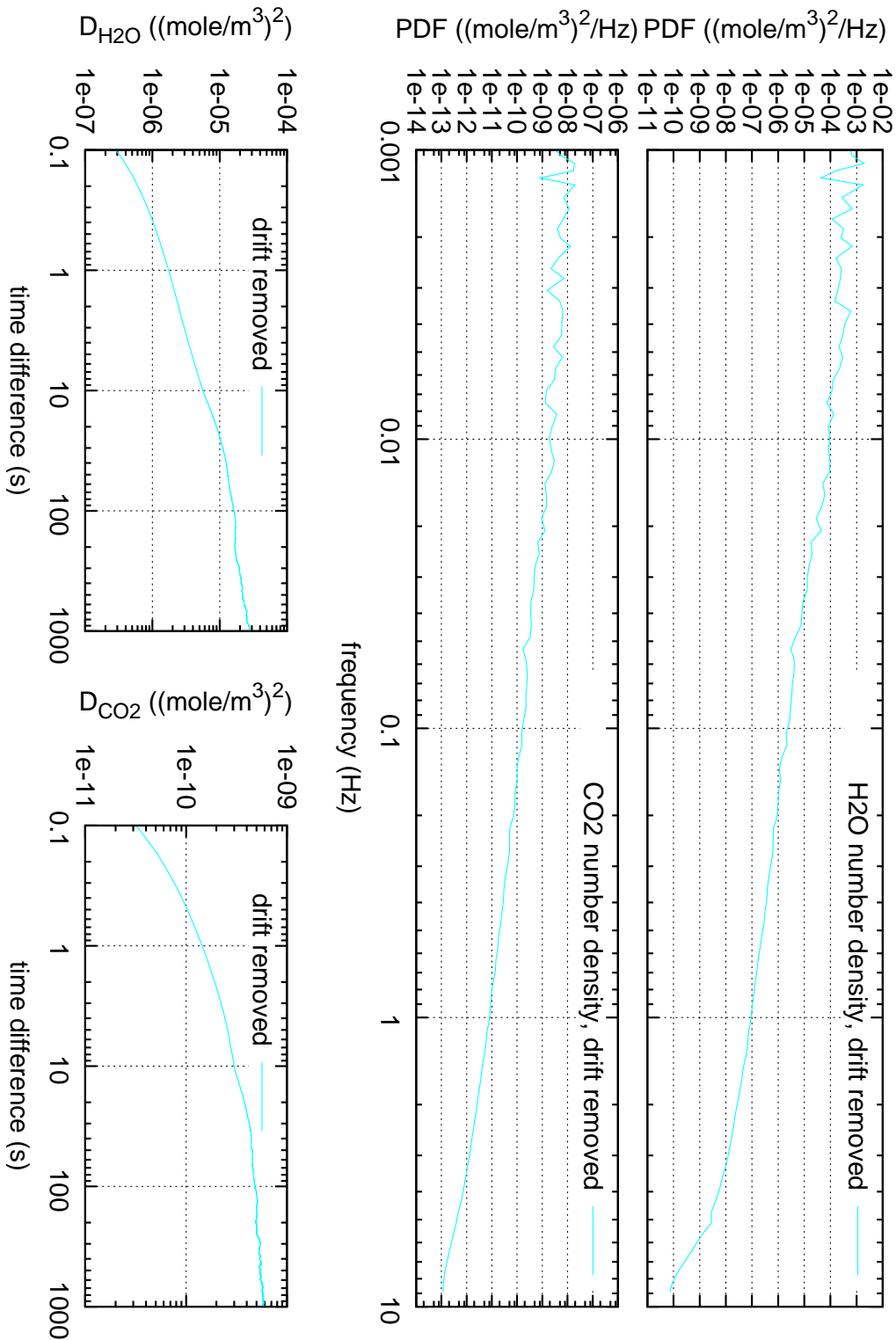
Figure 33: PDFs of water and CO_2 number densities near the VLTI control building roof top over four hours. Average wind velocity 8.7 m/s. Average humidity 0.037 mole/m^3.
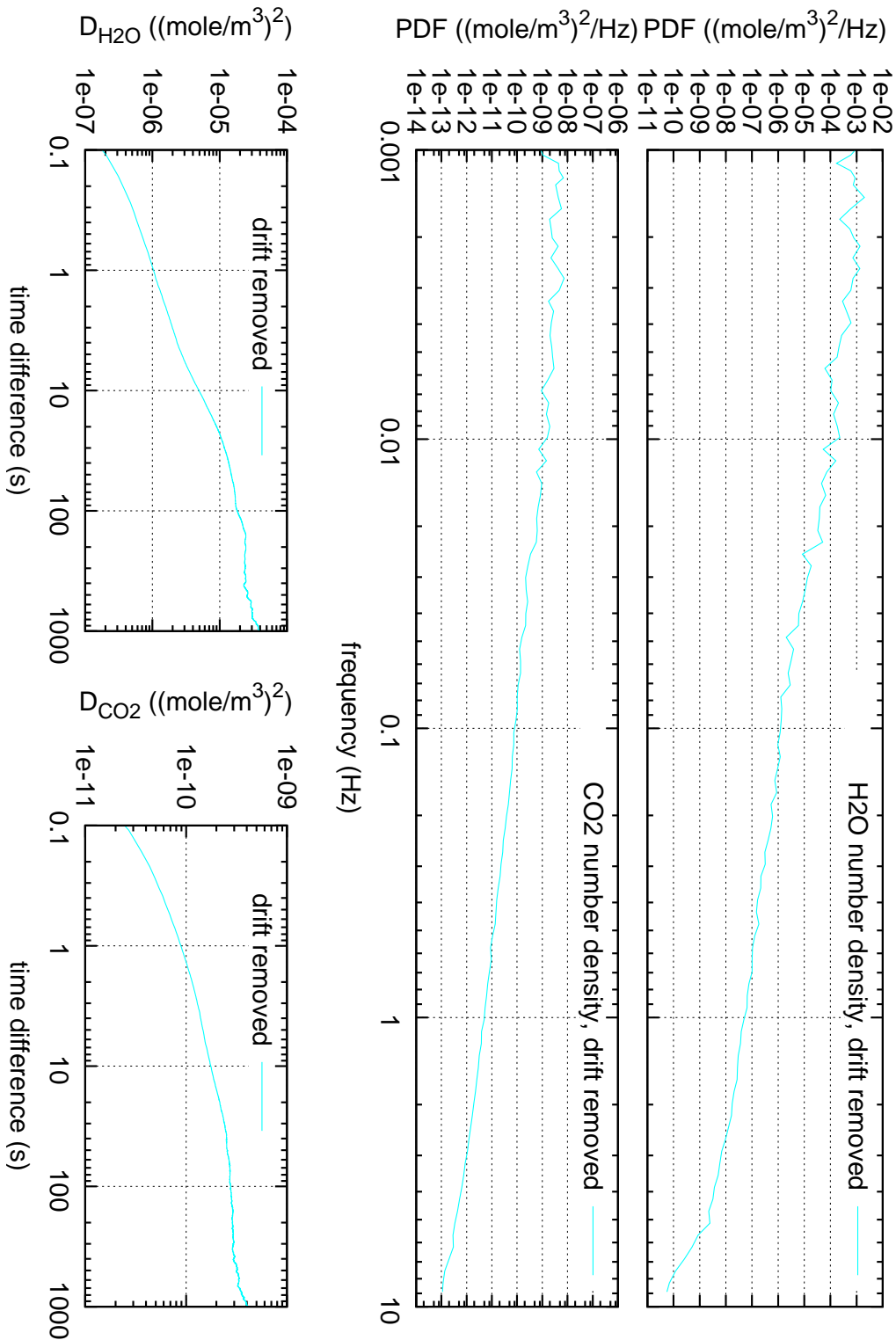
Figure 34: PDFs of water and CO$_2$ number densities near the VLTI control building roof top over four hours. Average wind velocity 12.7 m/s. Average humidity 0.066 mole/m^3.
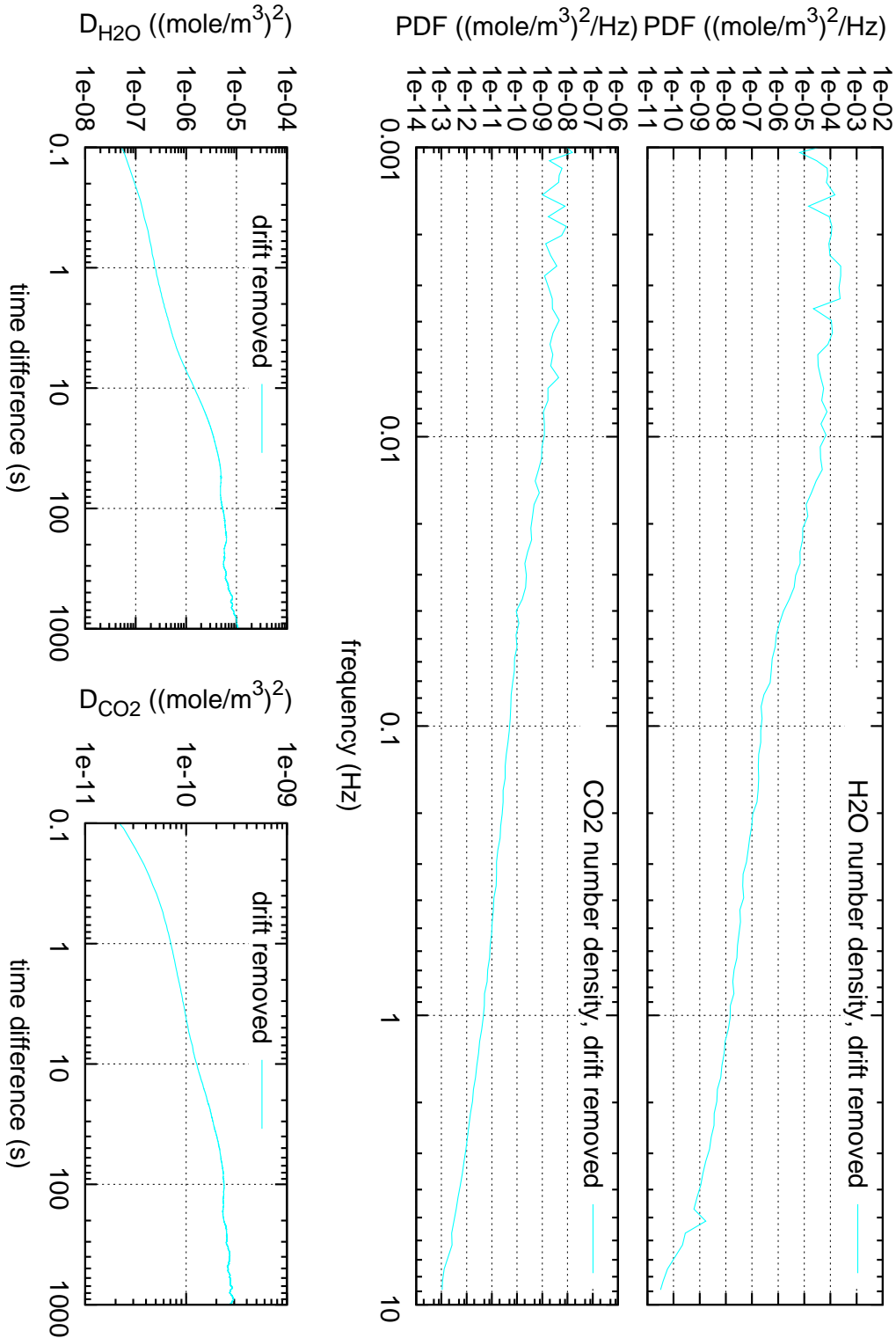
Figure 35: PDFs of water and CO_2 number densities near the VLTI control building roof top over four hours. Average wind velocity 15.7 m/s. Average humidity 0.099 mole/m^3.
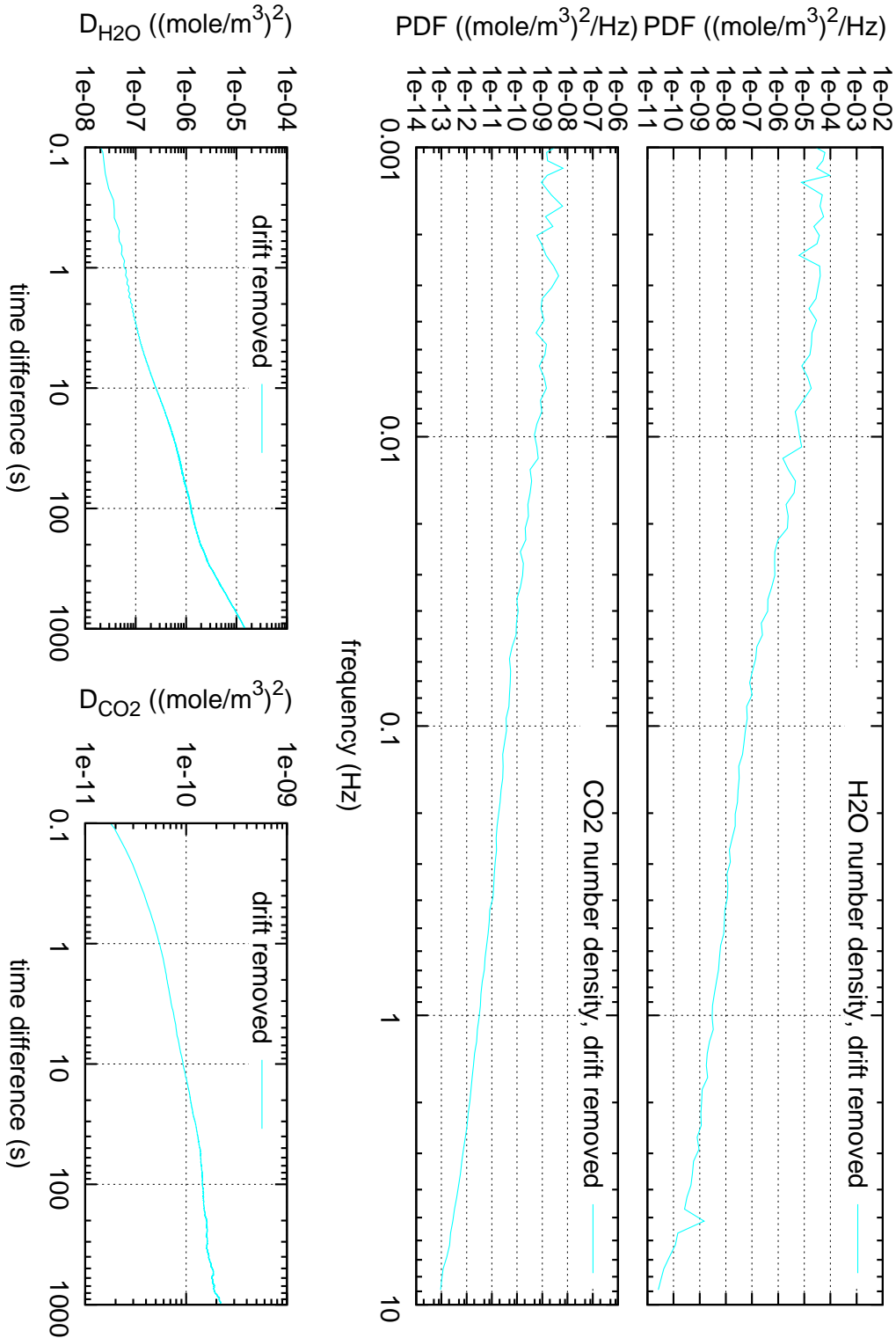
Figure 36:   PDFs of water and CO₂ number densities near the VLTI control building roof top over four hours. Average wind velocity 15.5 m/s. Average humidity 0.101 mole/m³.

3.2   VLTI Tunnel

For comparison, PDFs subsampled at 10 Hz over a time interval of 4 hours in the tunnel, selected from Figs. 20–22 and including the correction (1), are shown in Fig. 37–39.

At lower frequencies, VLTI tunnel power spectra are known from Fig. 49 of [13].
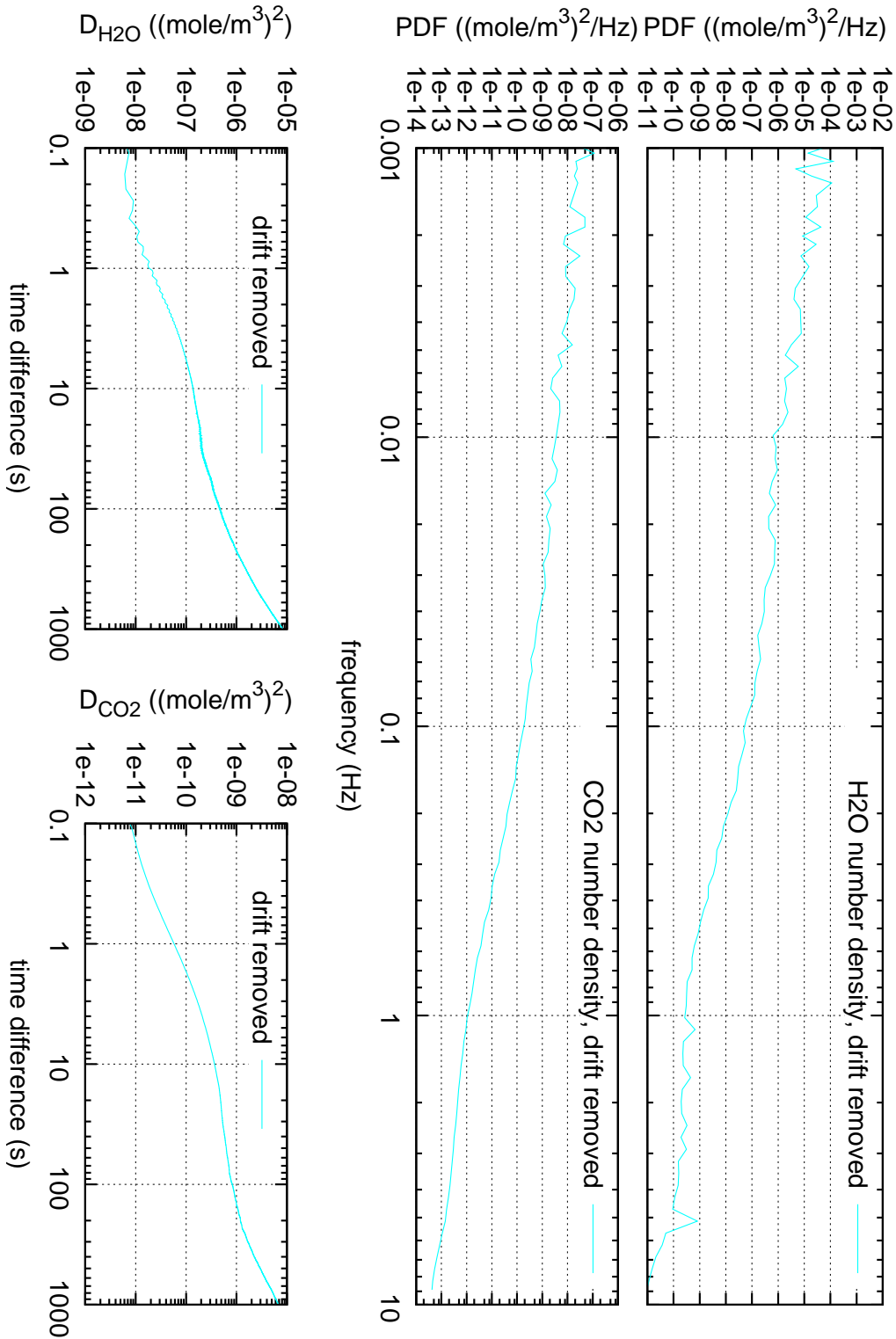
Figure 37: PDFs of water and CO$_2$ number densities over four hours in the tunnel. The input data are in Fig. 21.
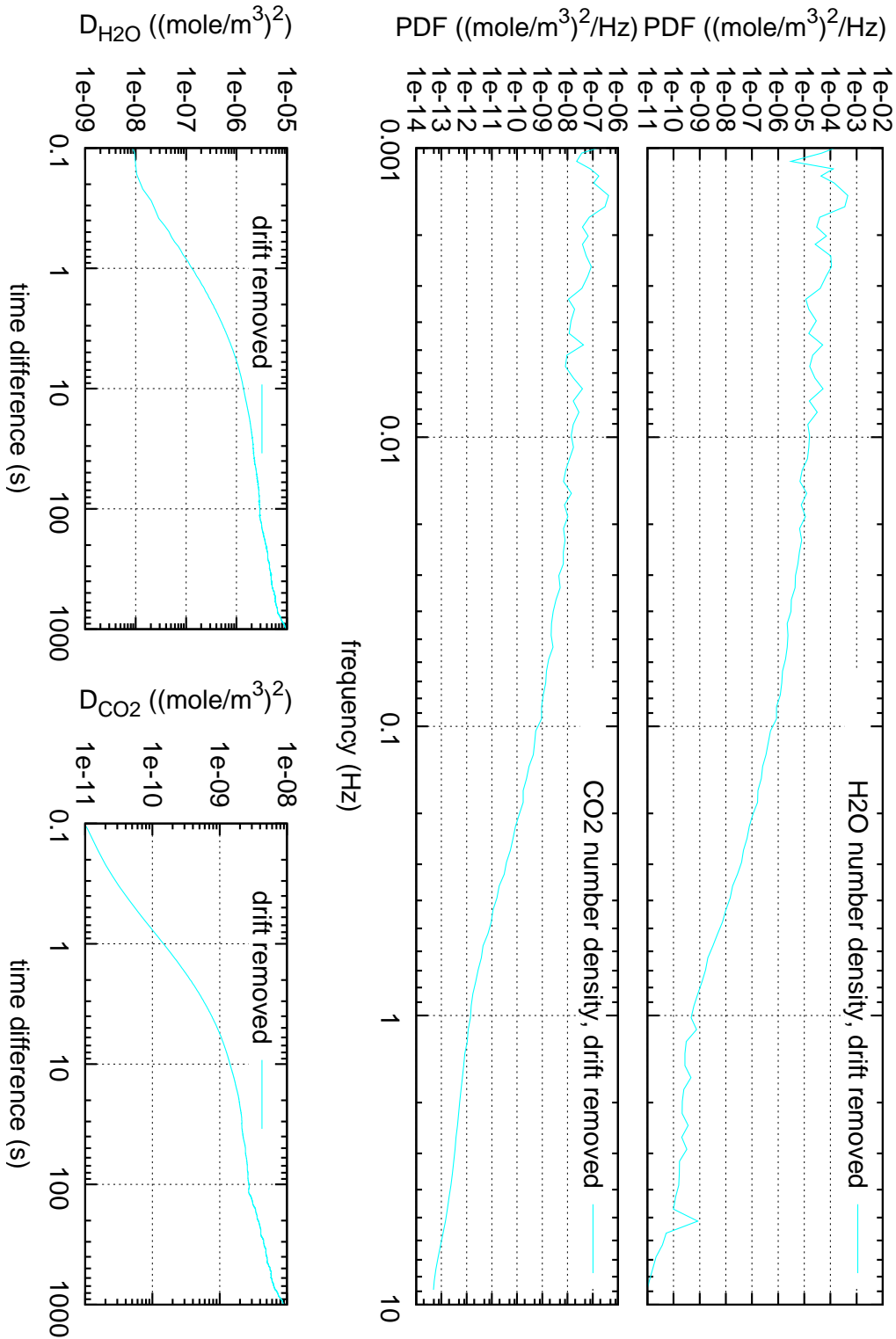
Figure 38: PDFs of water and CO$_2$ number densities over four hours in the tunnel. The input data are in Fig. 23
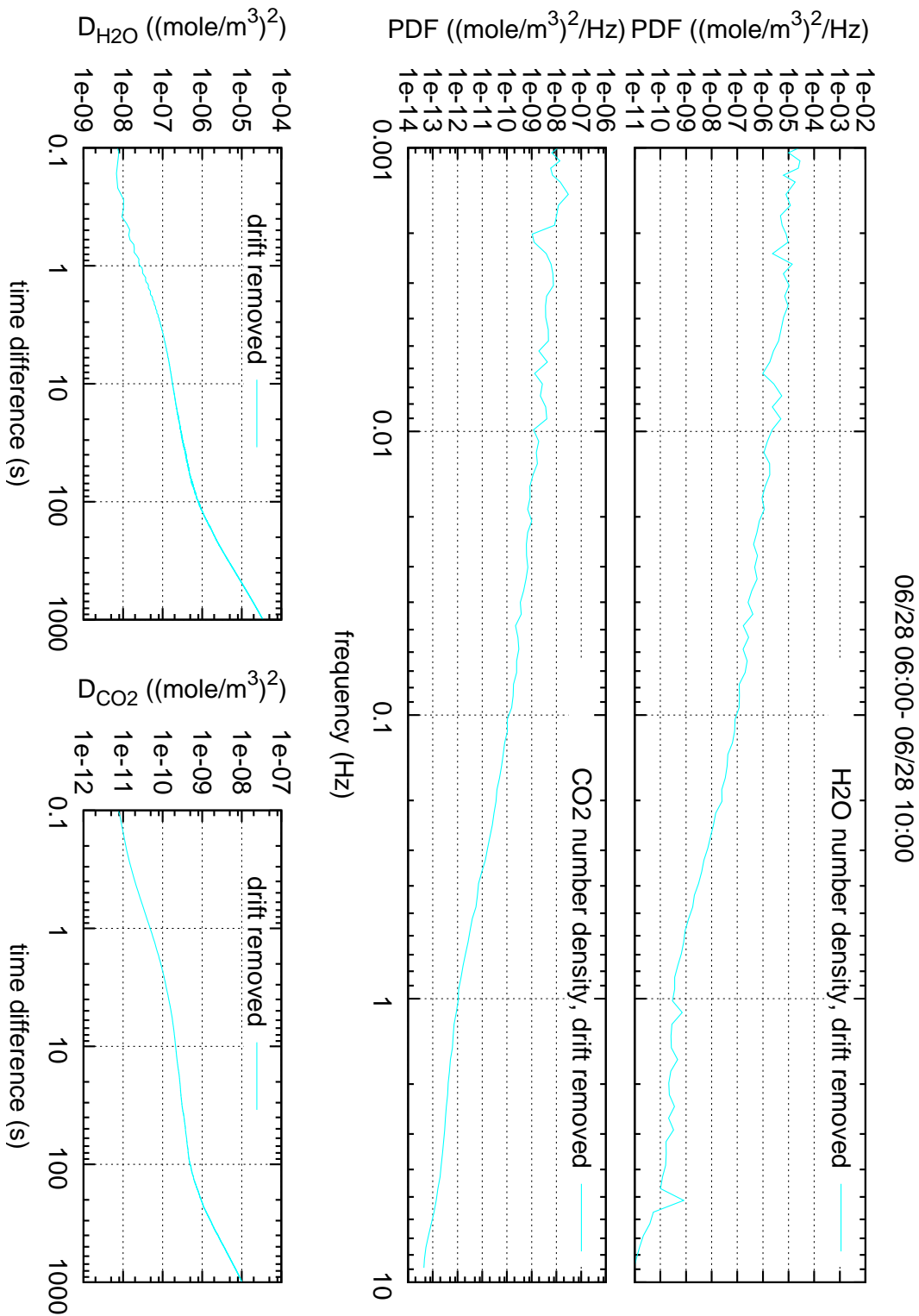
Figure 39: PDFs of water and CO_2 number densities over four hours in the tunnel. The input data are in Fig. 24

3.3 VST Dome

Finally PDFs over time intervals of 4 hours in the VST Dome, and including the correction (1), are shown in Fig. 40–45.
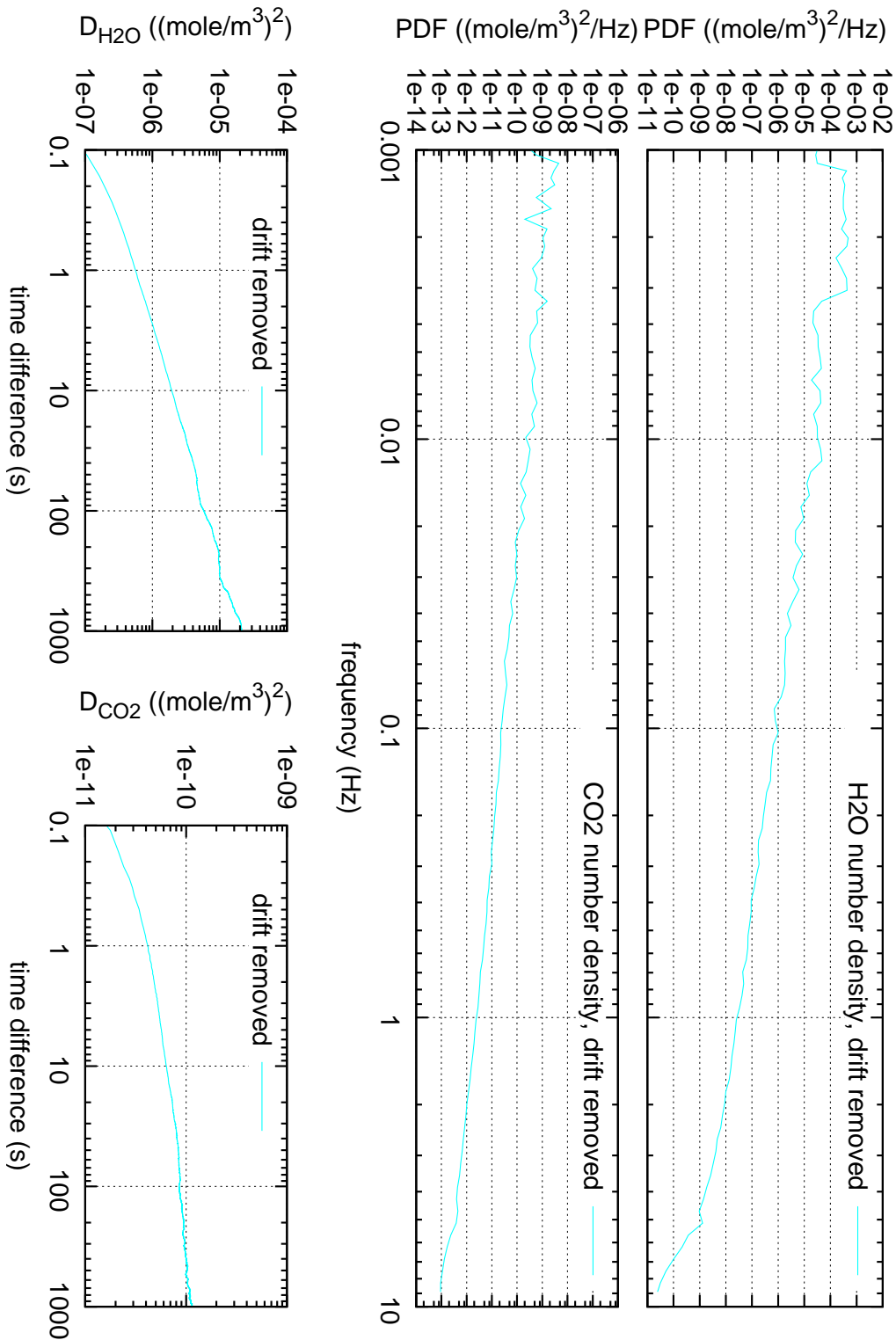
Figure 40: PDFs of water and CO$_2$ number densities over the four hours on the VST. Average wind velocity 9.6 m/s. Average humidity 0.093 mole/m^3.
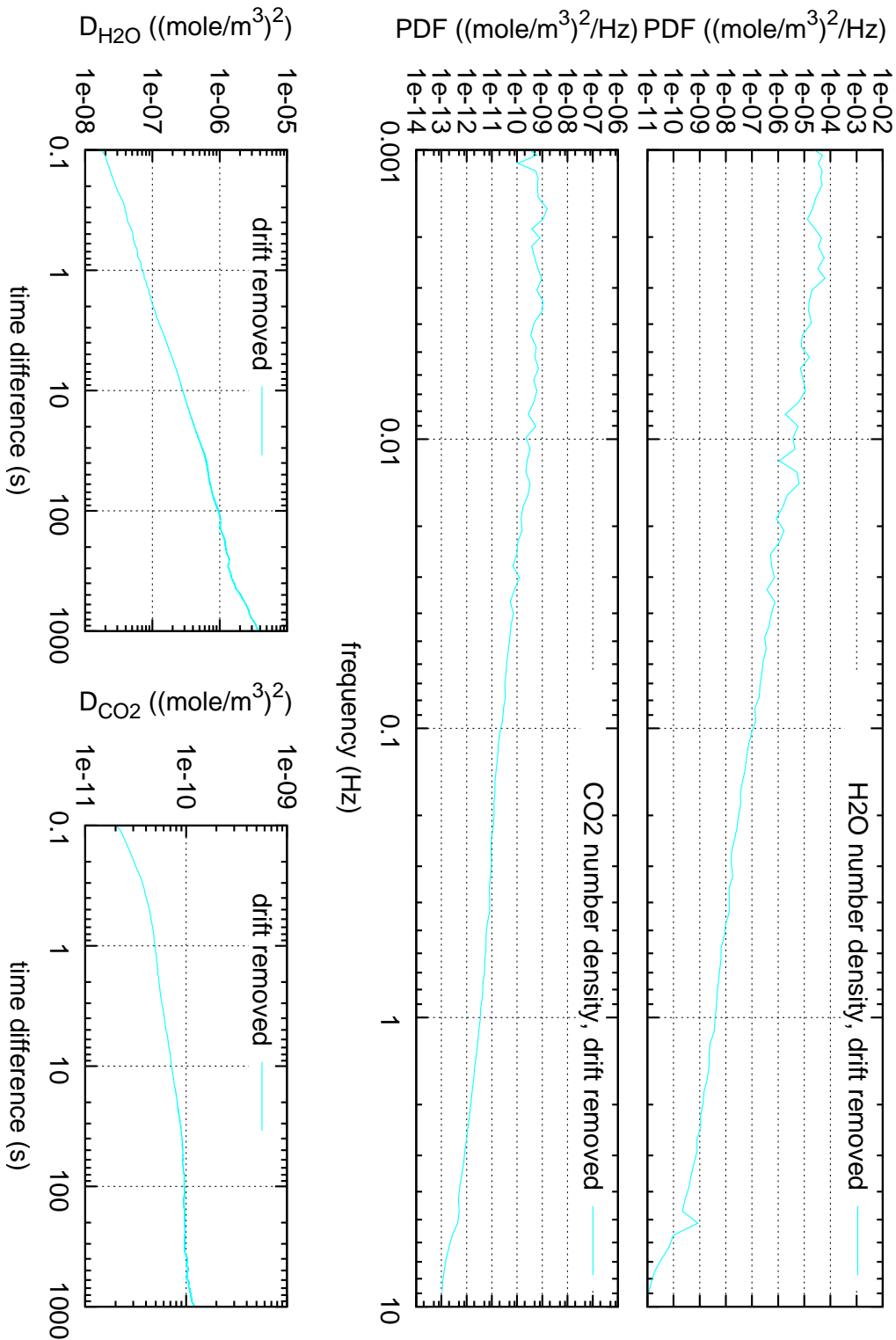
Figure 41: PDFs of water and CO_2 number densities over four hours on the VST. Average wind velocity 7.4 m/s. Average humidity 0.093 mole/m^3.
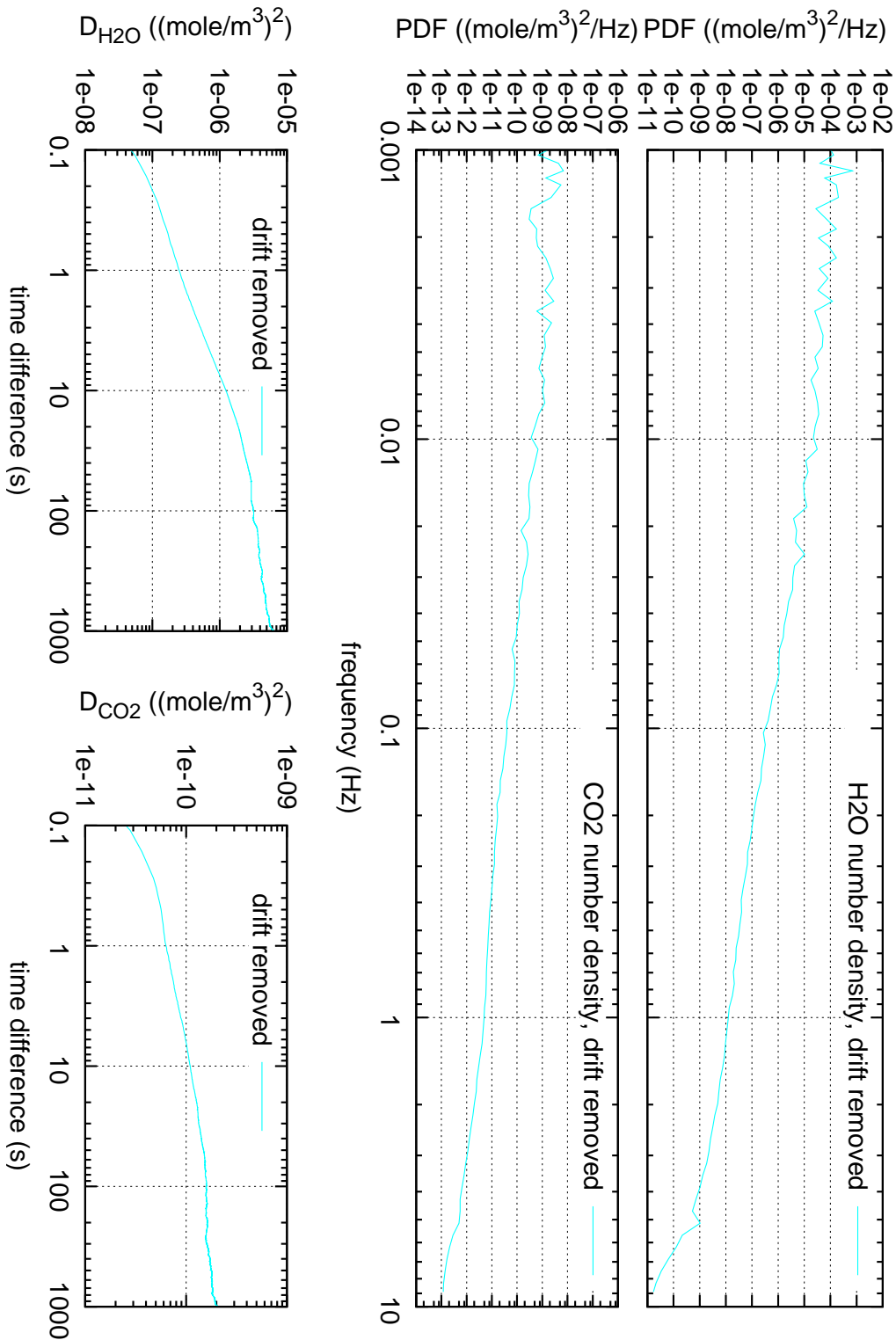
Figure 42:   PDFs of water and CO₂ number densities over four hours on the VST. Average wind velocity 7.2 m/s. Average humidity 0.101 mole/m³.
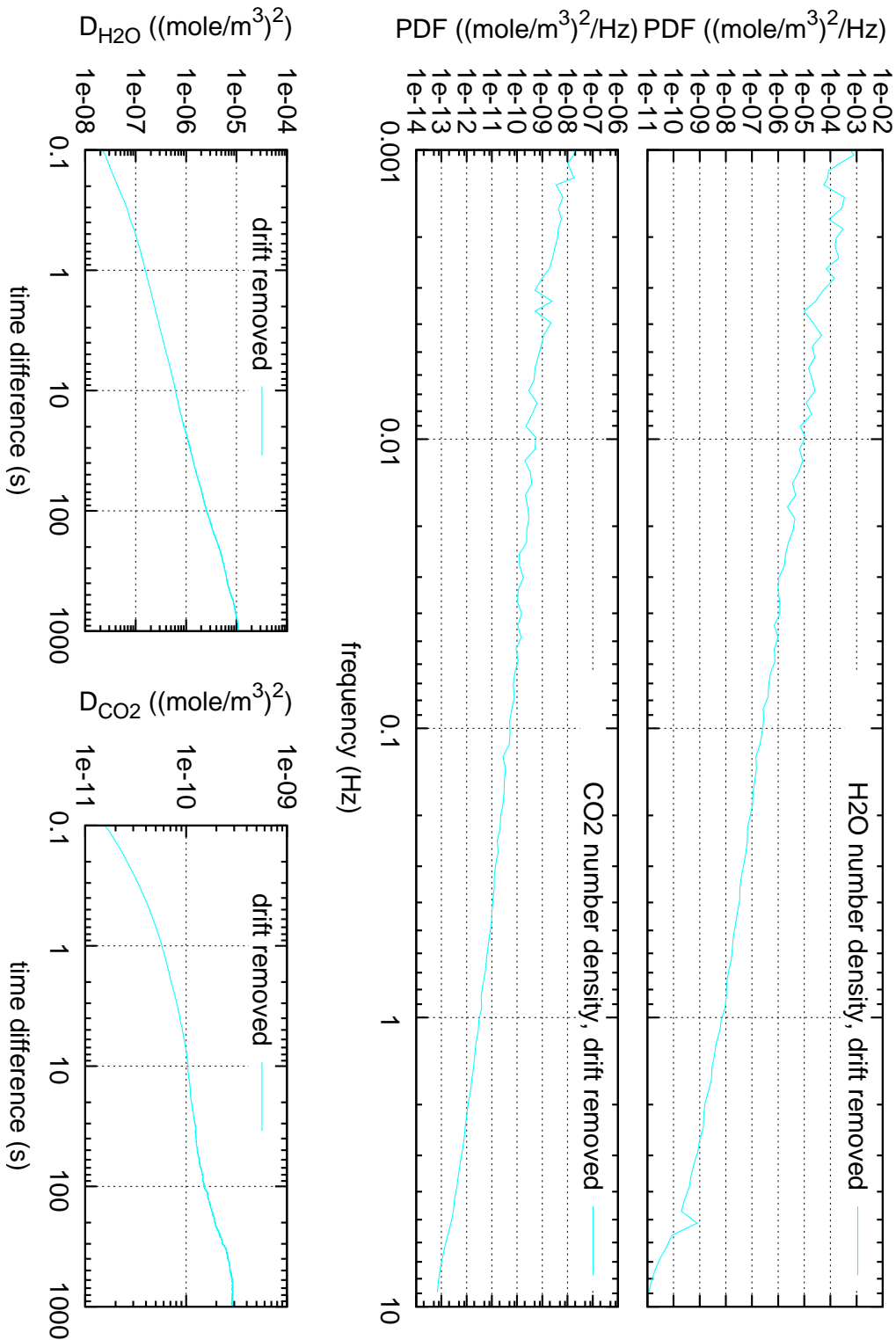
Figure 43: PDFs of water and CO_2 number densities over four hours on the VST. Average wind velocity 2.9 m/s. Average humidity 0.091 mole/m^3.
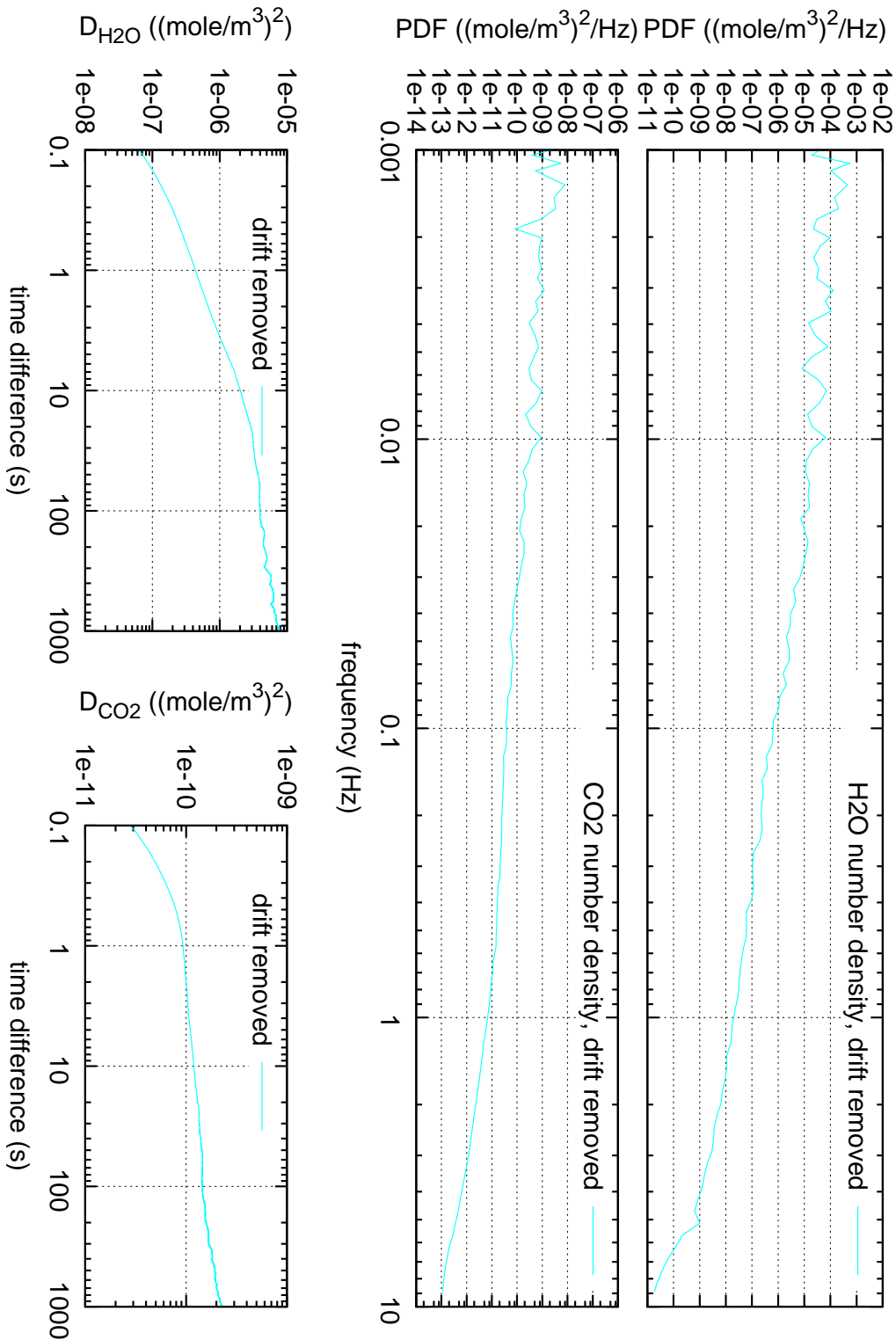
Figure 44:   PDFs of water and CO₂ number densities over four hours on the VST. The input data are in Fig. 27. Average wind velocity 4.8 m/s. Average humidity 0.077 mole/m³.
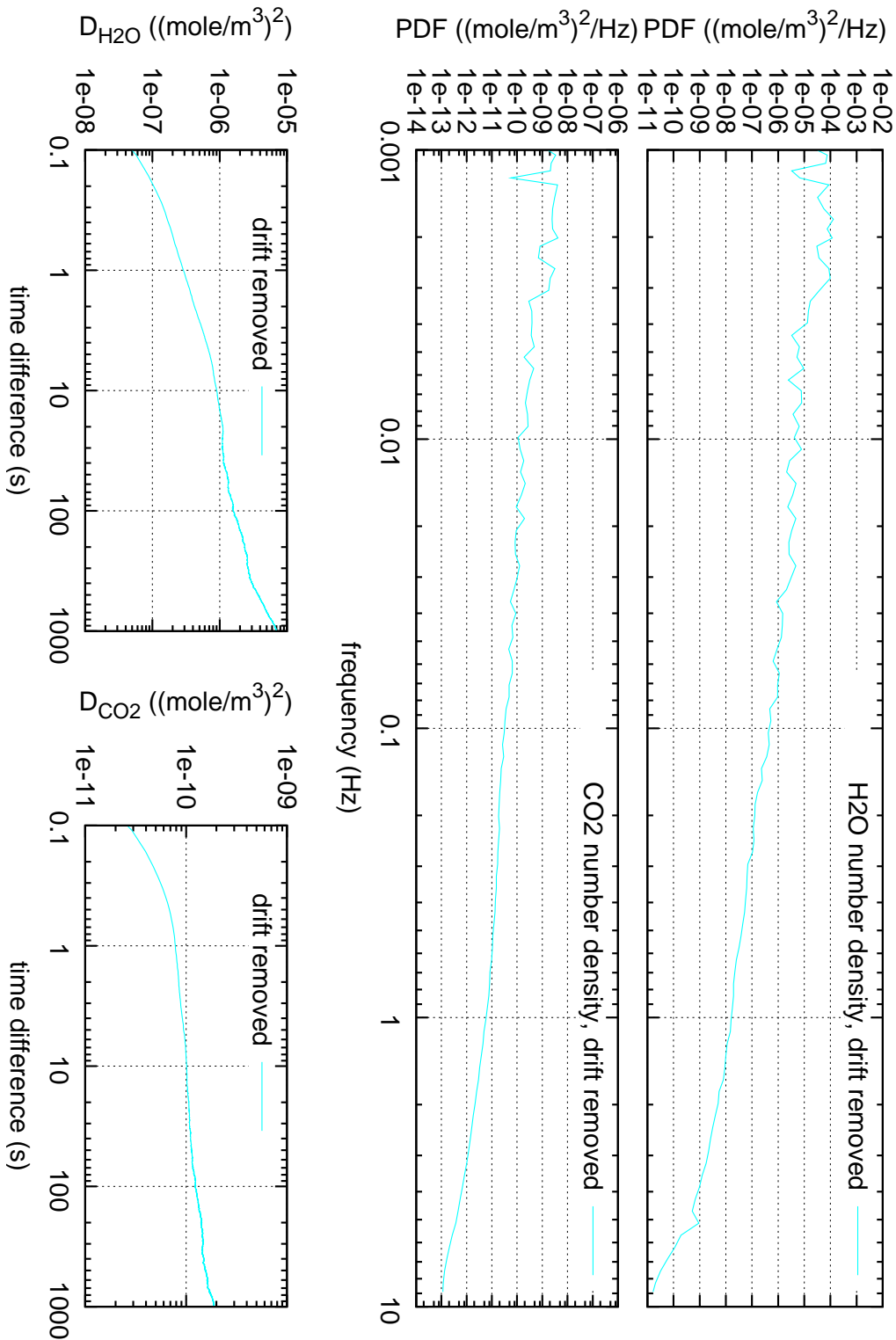
Figure 45: PDFs of water and CO_2 number densities over four hours on the VST. The input data are in Fig. 28. Average wind velocity 5.1 m/s. Average humidity 0.080 mole/m^3.

3.4   Synopsis

3.4.1   Outdoors

Figure 46 shows the structure functions of the previous plots that were obtained outdoors, those *not* gathered in the tunnel. The upper part of the figure shows the carbon dioxide data with two different ordinate scales. The ordinate to the right shows the fluctuations in the same units as before (number density fluctuations of CO$_2$), the ordinate to the left has the numbers multiplied by the square of 2051, that is the factor $c^2 \approx 4.207 \times 10^6$ obtained in section 5.1,[4] which is equivalent to showing the fluctuations in the entire "dry" section of air, including nitrogen, oxygen and so forth. Comments:

- On large time scales, the upper plot of Figure 46 is merely showing pressure and temperature changes. At Paranal conditions near 743 hPa and 31 mole/m^3, the relative daily variation of the pressure is of the order 1.5/743, that is $1.5/743 \times 31$ mole/m$^3 \approx 0.06$ mole/m^3. The square of this is $\approx 3.9 \times 10^{-3}$ (mole/m^3)^2, and this is actually the cap for the long-term fluctuations seen in the upper plot.

- At first sight, there seems to be a discrepancy between the large relative fluctuations (order of 10%) of the water content in figures like Figure 15 or 16, the comparatively small fluctuation (order 1 %) of carbon dioxide in the same figures, and the inverted dominance of the dry component [order 5×10^{-4} (mole/m^3)^2 at time differences of 1 second] over the water component [order 5×10^{-7} (mole/m^3)^2 at time differences of 1 second]. This discrepancy is only apparent, because the earlier figures show the relative fluctuations; water represents typically only 1/2 to 1 % of the total air density, and (the square of) this is the missing factor.

---

[4] ...or the square of inverse of the 380 ppmv of typical CO$_2$ content
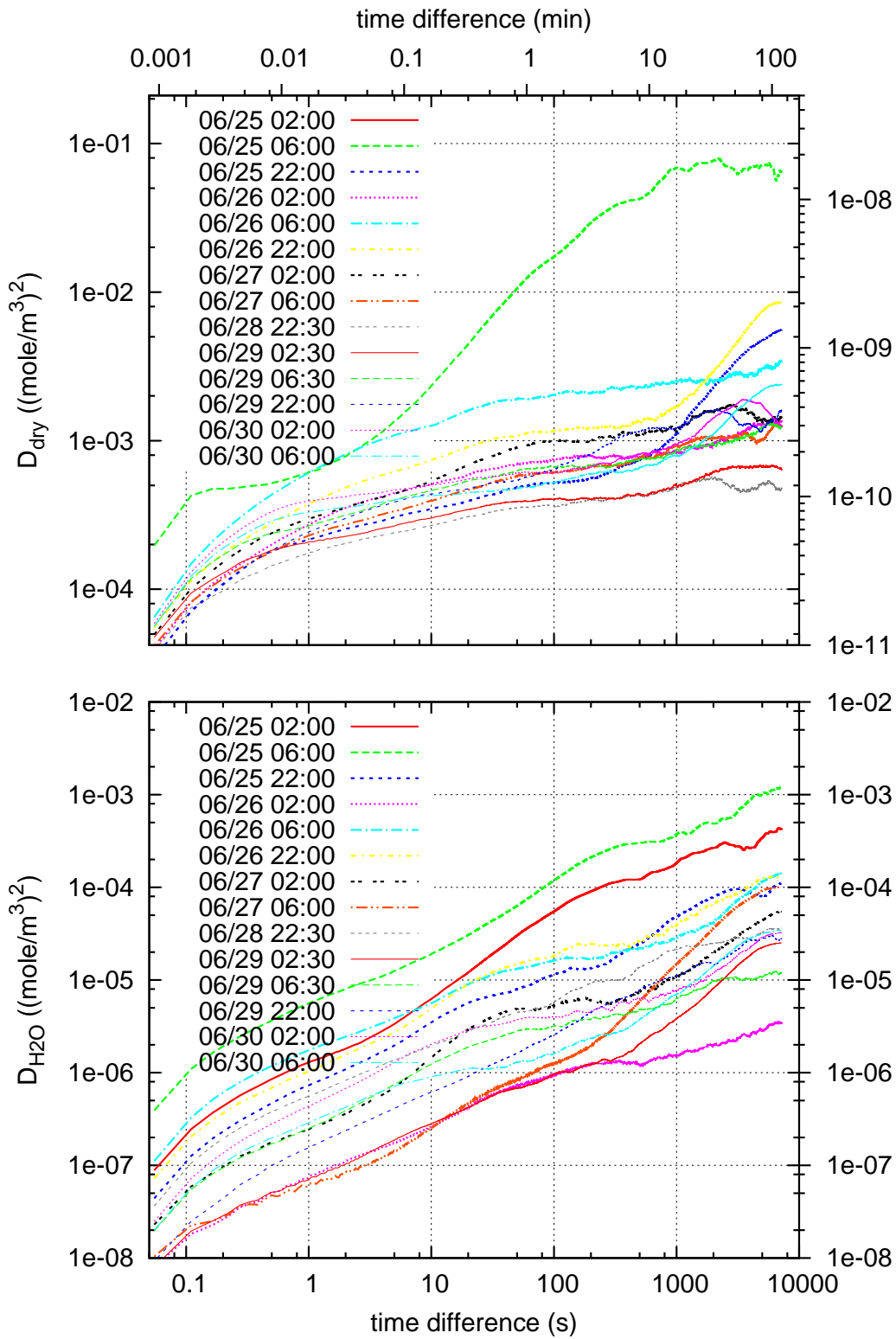
Figure 46: The structure functions of Figures 29–36 and 40–45 combined and on more extended time scales. The labels are day and hour of the start time. The eight curves with the thicker lines represent the VLTI roof-top data, the curves with the leaner lines represent the VST dome data.

One may conjecture that the scatter in the structure functions of figure 46 is largely from different wind speeds which transport eddies of a more uniform size by the LI-COR detector. To test this, the same data are converted from time to length scales by multiplying the abscissa axis of each curve with the individual (average) wind velocity over the four hours, which yields Figure 47. We see that this does not lead to closer/more compact alignment of the various curves of the various days—in fact the fluctuations of the CO$_2$/dry (upper) part of the figure becomes even less "universal" than the measurement as a function of time difference. The conjecture turns out to be wrong over this period of measurements, which means the turbulence was intrinsically weaker or stronger on time *and* length scales throughout the campaign.

Another conclusion from Figure 47 in comparison with template structure function derived from von-Karman power densities, Figure 55, is that there is no indication of a finite outer scale in the fluctuations of water vapor, that is, no flattening of $\mathcal{D}$ at larger time or space differences.[5]. Fitting to such a finite outer scale appears to be more promising for the "dry" component, the upper plot in Figure 47, but also remains elusive: according to the model in Figure 55, the transition from a power index $\beta - 2$ to the plateau is made with one decade on the abscissa axis, but this extends over four or more decades in Figure 47. Also, the initial steep ascend at spatial distances below 2 m might be an artifact of the 20 Hz (or even lower) low-pass filtering within the LI-COR instrument, and is not necessarily a well-proved feature.

---

[5]. . . in contrast to independent measurements over marine surfaces [20]
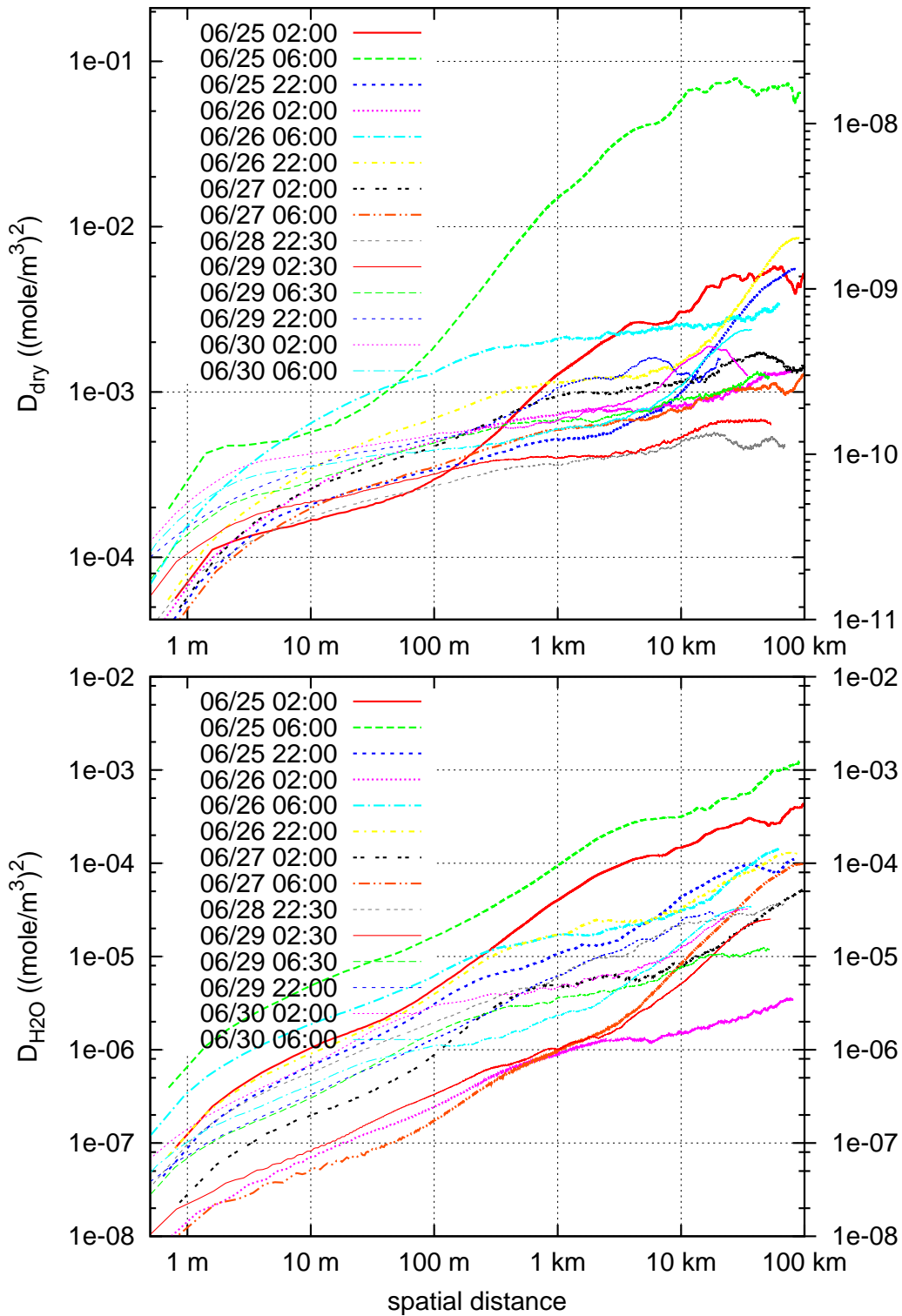
Figure 47: The structure functions as in figure 46 but the time axis converted to length scales by multiplication with the individual wind velocities. For this doubly logarithmic plot, this amounts to individual rigid shifts of the curves relative to Figure 46.

A final attempt to merge/reduce the water molecular fluctuations to a more universal curve is shown in Figure 48, based on the conjecture that the *relative* fluctuations—dividing the values of Figure 46 through the squared mean densities measured by the weather pole—might be closer to each other. Again, the curves reshuffle their positions, but the overall scatter remains the same, that is roughly two orders of magnitude at some point on the time difference axis.
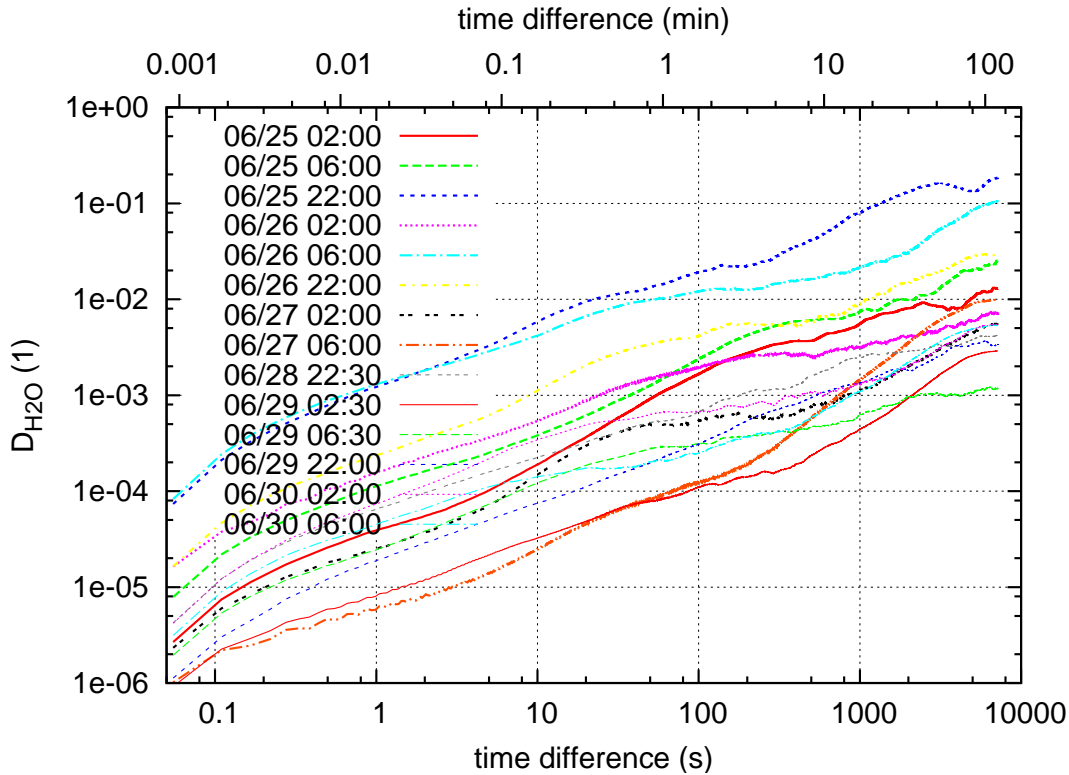
Figure 48:   The structure functions as in figure 46 have been been converted to relative fluctuations by dividing each curve through the square of the average number density over the corresponding 4-hr period. These average number densities are documented in the figure captions of Figures 29–36 and 40–45. Note that the value of 1.0 at the ceiling is some sort of theoretical maximum for any reduced structure function of this type.

Fits of the water vapor structure functions to the Kolmogorov spectral index of 2/3, Equation (17),

$$\mathcal{D}_\rho = C_\rho^2 (\Delta x)^{2/3} \tag{4}$$

work fairly well, represented by Figure 49. Straight lines are the fits. Measurements are the more wiggly companions of the same color and dashing pattern. C_ρ^2 is the only fitting parameter for each curve.

The fitting coefficients C_ρ^2 are gathered in Table 2. They are poorly correlated with the mean wind velocity during the 4 hours represented by each fit (Figure 50).
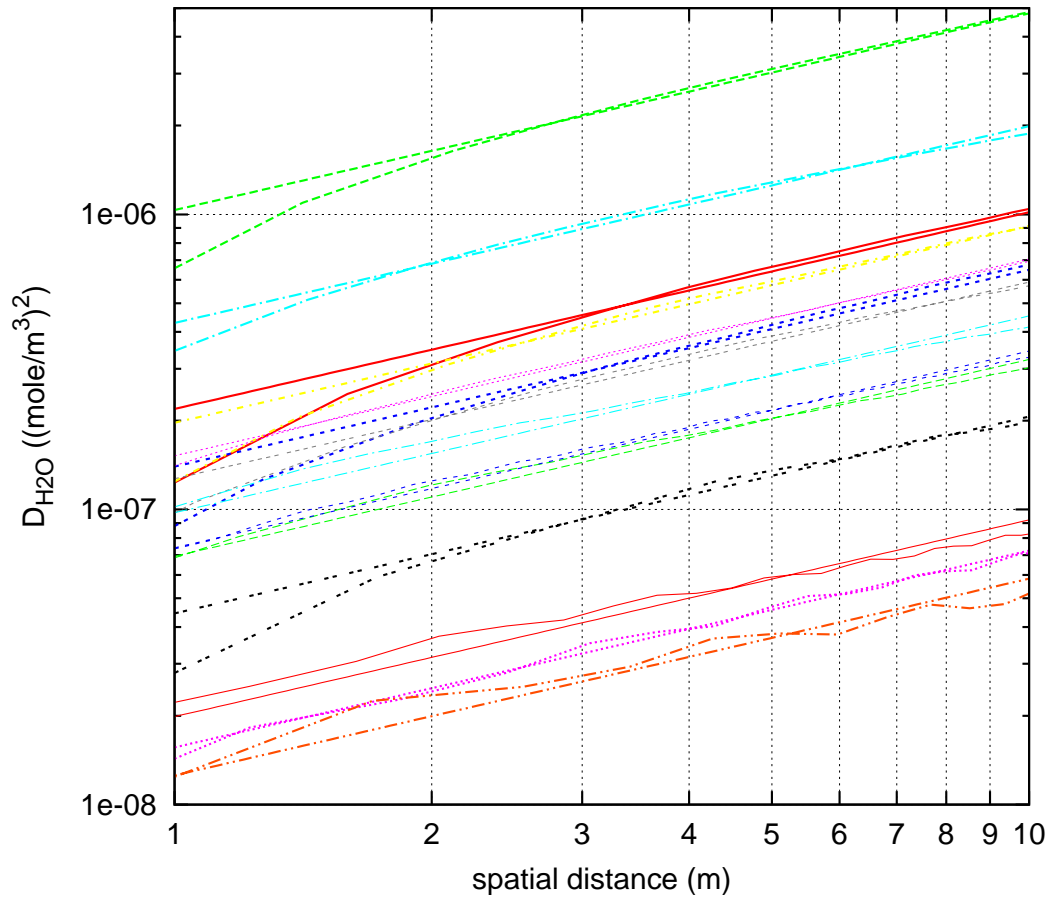
Figure 49: The initial range of the spatial structure functions from 1 to 10 m of Figure 47 is fitted to power laws $\mathcal{D}_{H2O} = C_\rho^2 (\Delta x)^{2/3}$ in the range 1 m $\leq \Delta x \leq$ 10 m.

start	Figure	label Fig. 50	C_ρ^2 (mole^2/m$^{20/3}$)
06/25 02:00	29	1	2.19×10^{-7}
06/25 06:00	30	2	1.03×10^{-6}
06/25 22:00	31	3	1.40×10^{-7}
06/26 02:00	32	4	1.56×10^{-8}
06/26 06:00	33	5	4.29×10^{-7}
06/26 22:00	34	6	1.97×10^{-7}
06/27 02:00	35	7	4.45×10^{-8}
06/27 06:00	36	8	1.26×10^{-8}
06/28 22:30	40	12	1.27×10^{-7}
06/29 02:30	41	13	1.99×10^{-8}
06/29 06:30	42	14	6.94×10^{-8}
06/29 22:00	43	15	7.42×10^{-8}
06/30 02:00	44	16	1.52×10^{-7}
06/30 06:00	45	17	9.75×10^{-8}

Table 2: Water structure function constants of the straight line fits of Figure 49.
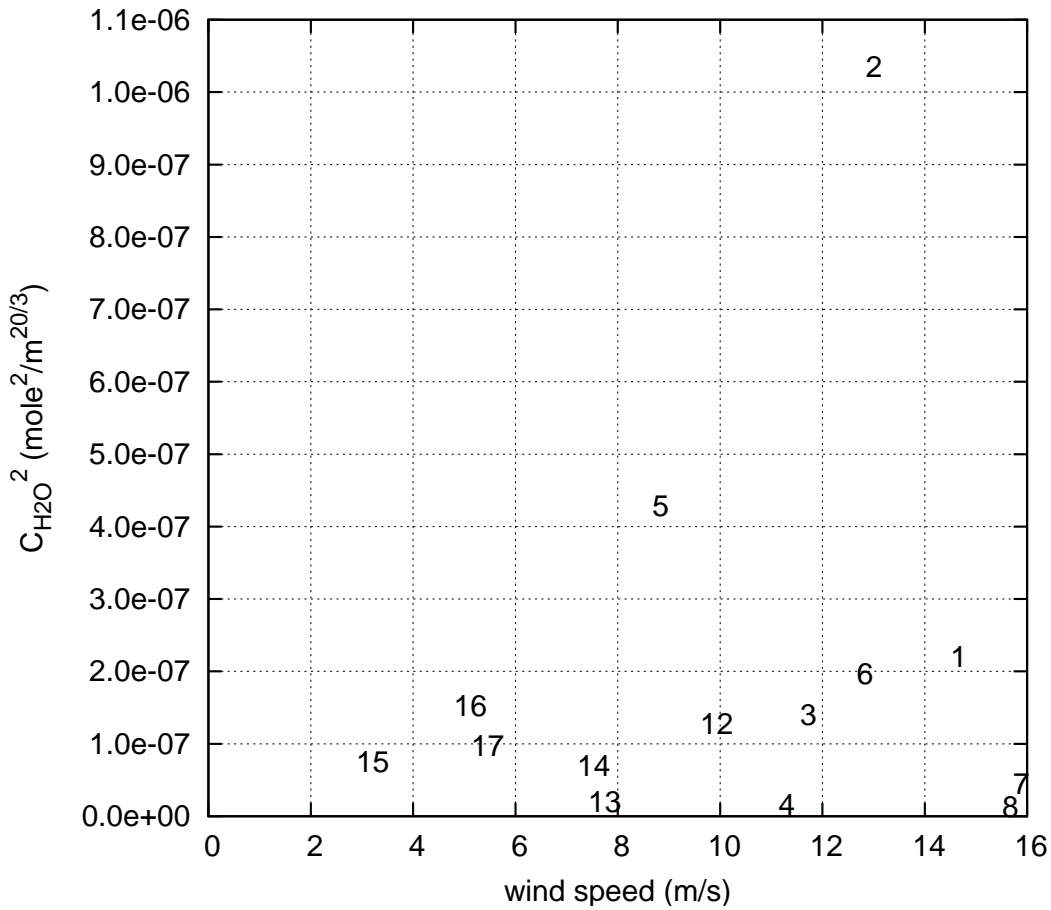
Figure 50: The constants of the Kolmogorov fit to the 3D water vapor structure functions of Table 2 are correlated with the mean wind speed of the water pole, as tabulated in the figure captions of Figures 29–36 (labels 1–8, Ctrl. building roof) and 40–45 (labels 12–17, VST dome).

3.4.2   Tunnel

The 14 structure functions computed over 14×4 hours from outdoors data (VLTI roof, VCS dome) are compared to the 3 structure functions computed over 3×4 hours in the tunnel in Figure 51. To the left, we show the outdoors data for water and carbon dioxide reproduced from Figure 46, and on the same scales to the right the tunnel data which summarize what is also shown in Figures 37–39.

The fluctuations of CO_2 are larger in the tunnel than outdoors for time differences above 1 second, and smaller for time differences below 1/2 second. The power index is very steep, approximately 1, for the carbon dioxide structure function in the tunnel.

Water vapor fluctuations are smaller in the tunnel than outdoors on timescales faster than 10 seconds.
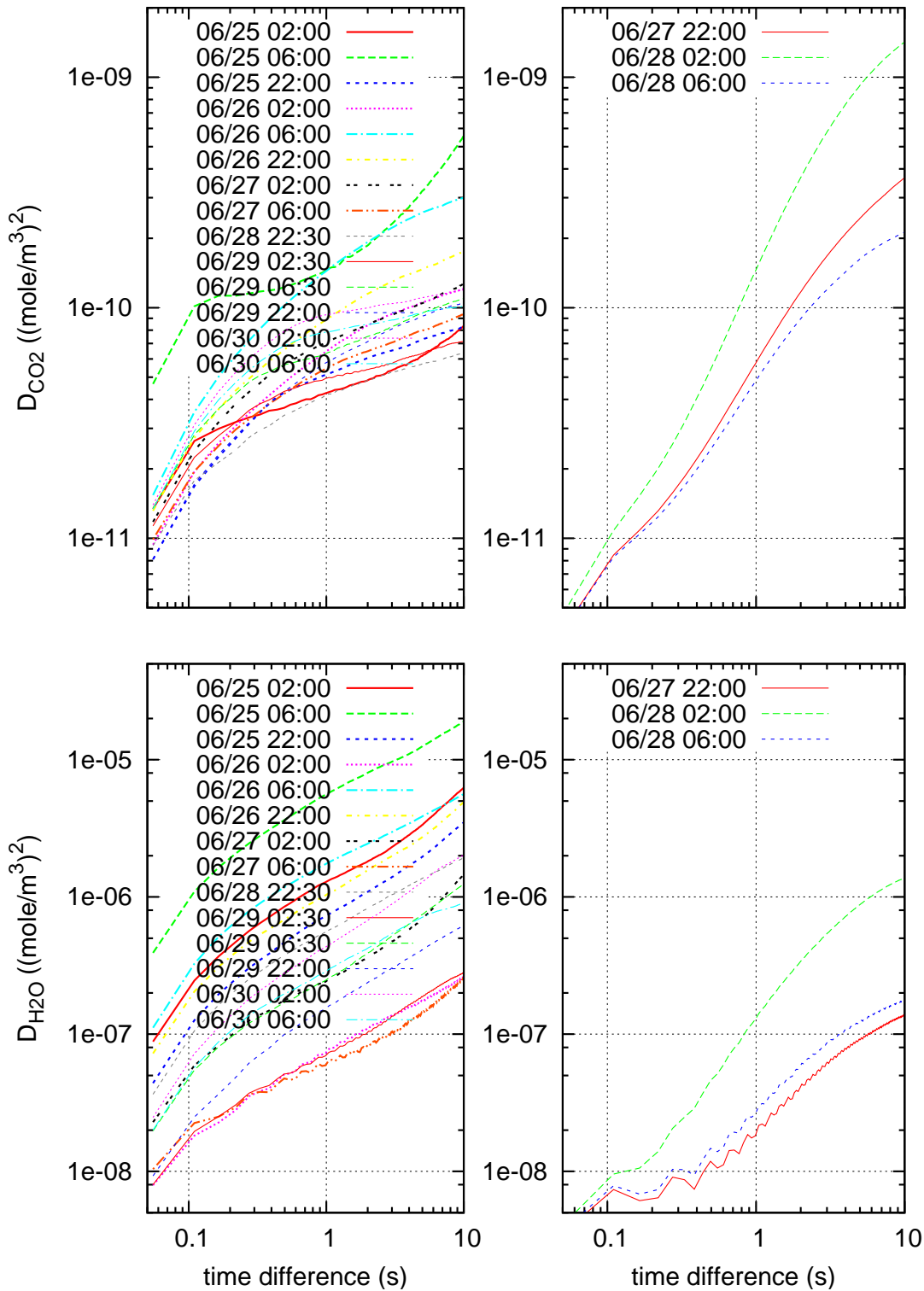
Figure 51: The first 10 seconds of the 14 structure functions of Figure 46 measured outdoors (left) are compared with the 3 measured in the tunnel (right). The labels are day and hour of the start time. On the left, the eight curves with the thicker lines represent the VLTI roof-top data, the curves with the leaner lines represent the VST dome data.

4 SUMMARY

The carbon dioxide and water vapor components have been measured at frequencies up to 20 Hz for 2 days and 12 hours near the westward edge of the VLTI control building roof, for 23 hours in the VLTI tunnel, and for 1 day and 14 hours in the hull of the VST dome. An obvious change in the performance of the 3-band gas analyser remains mysterious, but has been cushioned by re-scaling with the humidity data of the weather pole and/or GENIE sensors.

The first data were taken during rather wet conditions of 0.2 mole/m^3 of water vapor, followed quickly by rather dry conditions with number densities below 0.05 mole/m^3, ending on the last day with average densities near 0.1 mole/m^3. This contributed to structure function coefficient spreads of 2 orders of magnitude during different days of the campaign.

Carbon dioxide and water vapor structure functions are of different shape on all timescales slower than 1/2 second, indoors and outdoors. Water vapor fluctuations are genuinely stronger. This means (i) the 3D structure functions follow a 2/3-power law over 4 or even more orders of magnitude, with no sign of an flattening that would indicate a finite outer scale, (ii) they do not fit well-mixing models in the sense that they are not correlated to the carbon dioxide data (which we just take as tracers for the fluctuations of the entire "dry" section of the air) by scaling with the mean densities at any characteristic frequency. This can be interpreted as de-mixing and the presence of fractal bubbles (eddies not yet broken down, that is, from nearby sources) of water vapor in air.

Carbon dioxide density variations in the VLTI tunnel are much larger than outdoors, even during nights with no human activity. We conjecture that these are implied by nitrogen fluctuations caused by cooling liquids from VLTI instruments. This is correlated with the fact that the outdoors carbon dioxide content is close to the expected global average at that latitude, but too low on the average in the tunnel. The followup question is: What are the Nitrogen production/exhaust budgets of the VLTI instruments? Do they imply/explain the strong low-frequency variations of carbon dioxide in the tunnel (see Appendix 6.3.4 in [13])?

Carbon dioxide structure functions were outdoors more predictable than water vapor structure functions, with coefficients spreading only over half a magnitude during the days of the campaign. On scales of 2 m and longer, they are evidently flatter than the water structure functions. We interpret this as a different topology of mixing, but do not find the quick cross-over to a constant within approximately one decade of the abscissa axis that is mandated by von-Karman spectra with a single outer scale.

The measurement of fluctuations of both carbon dioxide and water clearly separates them in the sense that the fluctuations of refractive indices in the mid-infrared are dominated by water vapor fluctuations, although both components have comparable dipole oscillator strengths *on a per-molecule basis*.

Water vapor structure function coefficients measured outdoors are poorly correlated with the wind velocity obtained at the weather pole.

The two positions for the outdoor measurements are both close to edges of concrete constructions. This network is too fuzzy for any judgement on whether the water vapor turbulence might be smaller higher up the ground under more streamlined conditions, or perhaps further away from the mountain.

5   APPENDIX

5.1   Correlation of Mixing Ratios

One might expect that the mixing ratios of the water and the carbon dioxide molecules are anti-correlated if measured relative to one mole of air [6, 11]. The idea is that water replaces other gases indiscriminately. If we ignore inter-molecular virials (stay within the ideal-gas approximation) this hypothesis is

$$x_{\mathrm{N2}} + x_{\mathrm{CO2}} + x_{\mathrm{H2O}} = 1 \tag{5}$$

for the mixing ratios of the components, N2 denoting the "other" components like nitrogen, CO2 denoting carbon dioxide, and H2O denoting water. Supposed the "other" components are always well mixed with CO$_2$, $c \equiv x_{\mathrm{N2}}/x_{\mathrm{CO2}} \approx 0.781/380 \times 10^{-6} \approx 2050$ a constant, the equation predicts

$$x_{\mathrm{CO2}} = \frac{1}{1+c} - \frac{x_{\mathrm{H2O}}}{1+c}. \tag{6}$$

To reduce the water content by $\Delta x_{\mathrm{H2O}} \approx 0.008$, for example, the carbon dioxide content ought to rise by $\Delta x_{\mathrm{CO2}} \approx 0.008/2050 \approx 4 \times 10^{-6}$. Fig. 52 tests this hypothesis. The anti-correlation shows only for the first hours of the data (red color in the figure). The weak point of the hypothesis is that it cannot be validated if human (biological) activity changes the CO$_2$ content on the time scales the hypothesis is investigated.

Note that there is an anti-correlation built into the correction for the separation of overlapping absorption bands in the instruments [4], which—if exaggerated or done at wrong temperatures or pressures—would enhance or suppress such a result. This instrumental effect is to be removed prior to interpretation of mixing ratios.

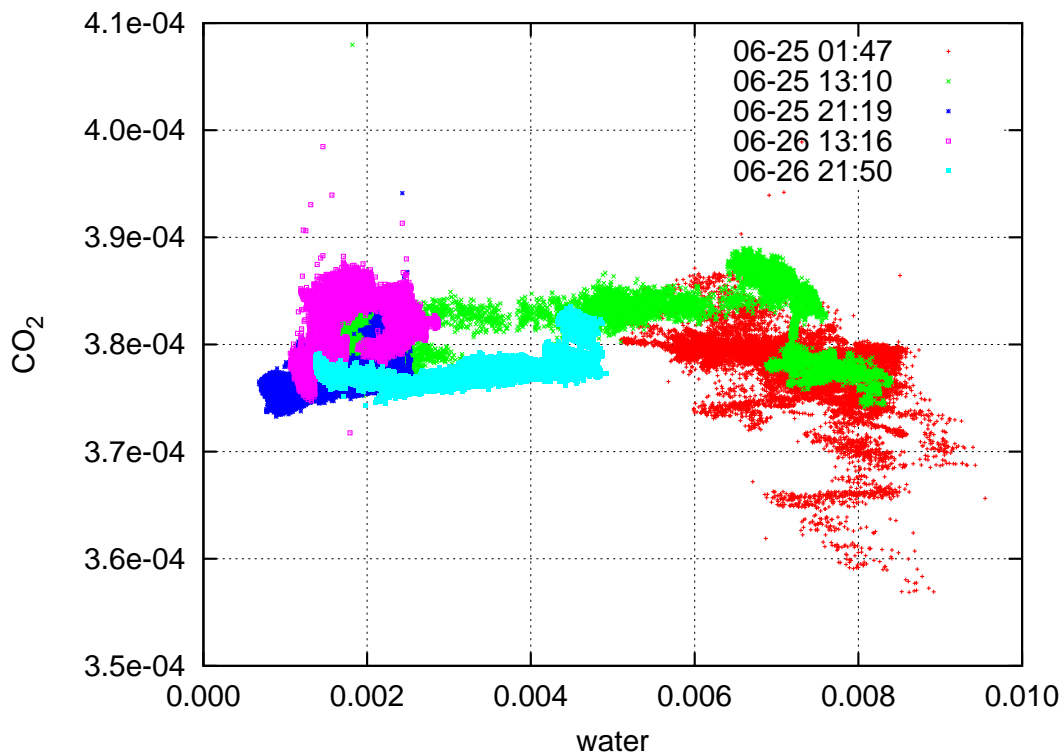Figure 52: The mixing ratio of water (in units of mole per mole of air) is plotted against the mixing ratio of carbon dioxide in the same units for the early measurements at the VLTI building. The time stamps of when these blocks of measurements start are in the upper right edge; the red dots are for the first data file, the green for the next file, etc. up to the light blue one for the fifth, as enumerated in Table 1.

5.2   Von-Karman Spectra

Power-density functions of the von-Karman type are [7, 9]

$$\text{PDF}_f(\nu) = \frac{1}{T} \left| \int_0^T e^{2\pi it\nu} f(t)dt \right|^2 = p_0(\nu^2 + \frac{1}{t_0^2})^{-\beta/2} \tag{7}$$

where p_0 denotes the strength of the spectrum, t_0 is an outer scale (in units of time), ν the frequency. The difference to the Kolmogorov spectra is that the power density stays finite at small ν and therefore remains Fourier-integrable (Fig. 53).
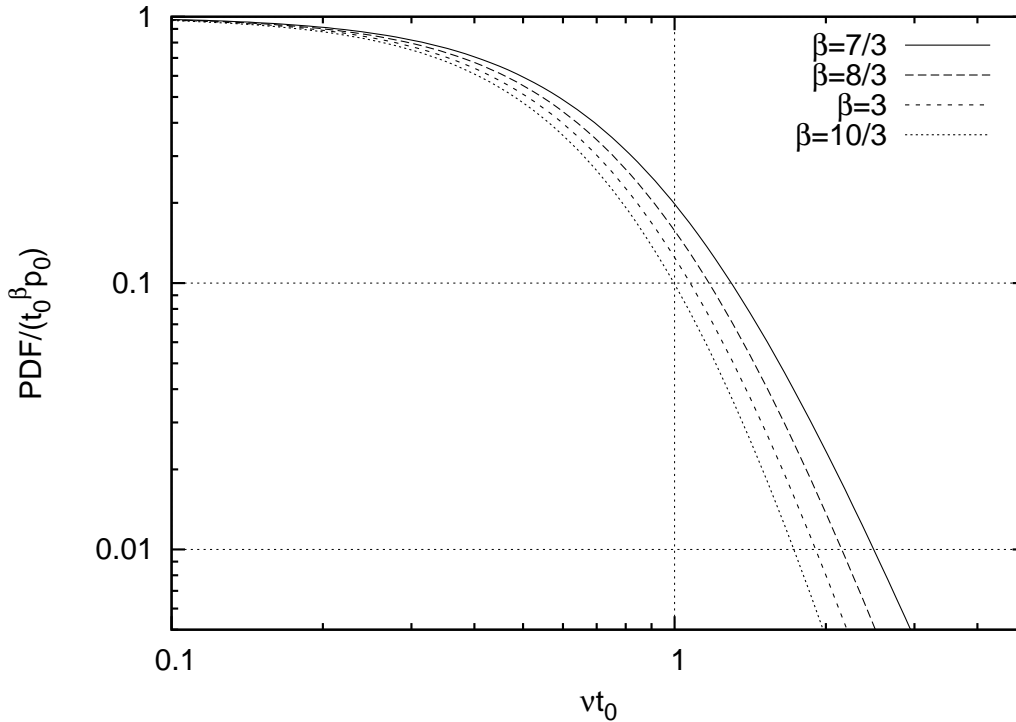
Figure 53:   Von-Karman type of a PDF with outer scale t_0 as a function of reduced frequency ν with four different exponents falling off $\sim \nu^{-\beta}$ at the blue end of the spectrum. The slope of the curves in this double logarithmic display is $-\beta/2$ at $\nu = 1/t_0$, $-4\beta/5$ at $\nu = 2/t_0$, and generally $-\beta(\nu t_0)^2/[(\nu t_0)^2 + 1]$.

We interpret this again as a 2-sided spectrum, PDF(ν)=PDF($-\nu$). The Fourier inversion of (7) is (up to the random phase factor hidden by having started only from a modulus) [8, 8.432.5]

$$f(t) = \sqrt{Tp_0} \int_{-\infty}^{\infty} e^{-2\pi i\nu t}(\nu^2 + 1/t_0^2)^{-\beta/4}d\nu = 2\sqrt{Tp_0}\frac{(\pi t_0^2)^{\beta/4}}{t_0\Gamma(\beta/4)}(t/t_0)^{\beta/4-1/2}K_{\beta/4-1/2}(2\pi t/t_0) \tag{8}$$

where K are the modified Bessel functions of the 2nd kind [1, §9.6]. $f(t)$ is displayed in Figure 54. To end up with a finite limit as $t \to 0$ we need to stay in the range $\beta > 2$.

For $t/t0 \to 0$ we have $(t/t_0)^{\beta/4-1/2}K_{\beta/4-1/2}(2\pi t/t0) \to \Gamma(\beta/4 - 1/2)/(2\pi^{\beta/4-1/2})$ [1, 9.6.9], therefore $f(0) = 4\sqrt{\pi p_0 T}\frac{\Gamma(\beta/4-1/2)}{\Gamma(\beta/4)}t_0^{\beta/2-1}$. Examples of the structure function

$$\mathcal{D}_f(\Delta t) = \langle\, |\, f(\Delta t) - f(0)\, |^2 \rangle \tag{9}$$

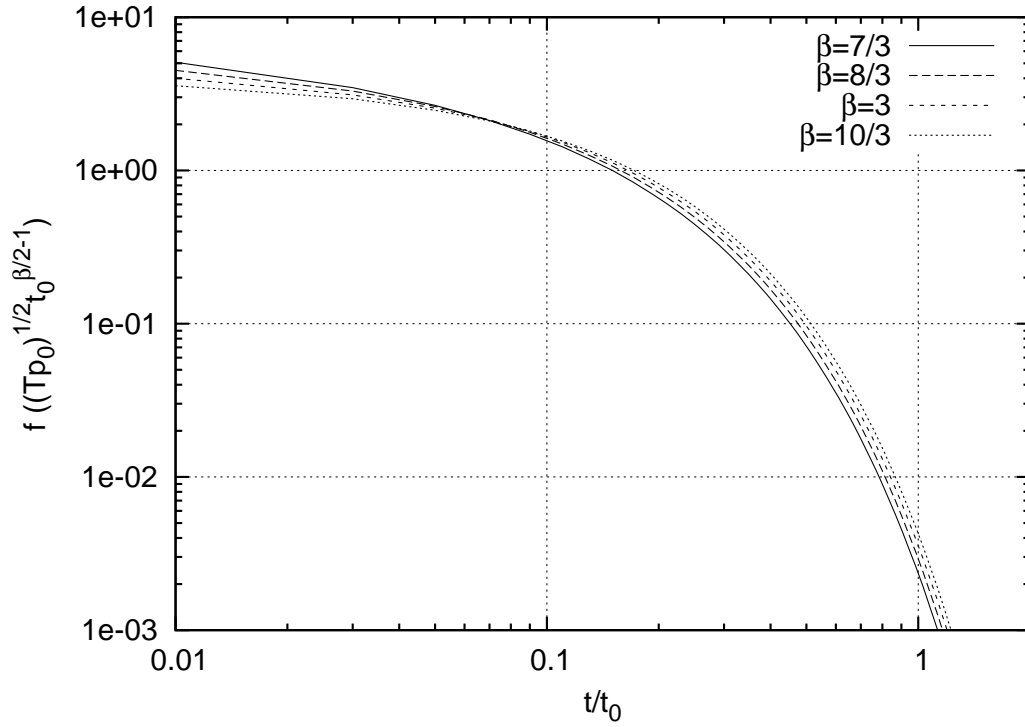Figure 54: The function $f(t)$ in (8) for the same exponents β as in Fig. 53, divided by $\sqrt{Tp_0}t_0^{\beta/2-1}$.

are in Figure 55. (Having dropped the unknown phase factor in (7) means that—with the shift theorem of Fourier transforms—the starting time has implicitly moved to $t = 0$.)

For large Δt,

$$\mathcal{D}_f(\Delta t \rightarrow \infty) = f(0)^2 = 16\pi p_0 T t_0^{\beta-2} \Gamma^2(\beta/4 - 1/2)/\Gamma^2(\beta/4) \tag{10}$$

The dominant terms at small Δt are worked out as follows: set $x \equiv t/t_0$ and $\kappa = \beta/4 - 1/2$ to simplify the notation. Elimination of $f(x = 0)$ is equivalent to eliminating the constant term in $x^\kappa K_\kappa(2\pi x)$. Essentially we need a small-x expansion of

$$x^\kappa K_\kappa(2\pi x) - \Gamma(\kappa)/(2\pi^\kappa). \tag{11}$$

Use [8, 8.485][1, 9.6.2]

$$\ldots = x^\kappa \frac{\pi}{2} \frac{1}{\sin \pi\kappa} \left[I_{-\kappa}(2\pi x) - I_\kappa(2\pi x) \right] - \frac{\Gamma(\kappa)}{2\pi^\kappa} \tag{12}$$

where [1, 9.6.10][8, 8.445]

$$
\begin{aligned}
I_{-\kappa}(2\pi x) - I_\kappa(2\pi x) &= \frac{1}{\Gamma(-\kappa+1)}(\pi x)^{-\kappa} + \frac{1}{\Gamma(-\kappa+2)}(\pi x)^{-\kappa+2} + \frac{1}{2\Gamma(-\kappa+3)}(\pi x)^{-\kappa+4} + \ldots \\
&\quad - \frac{1}{\Gamma(\kappa+1)}(\pi x)^\kappa - \frac{1}{\Gamma(\kappa+2)}(\pi x)^{\kappa+2} - \frac{1}{2\Gamma(\kappa+3)}(\pi x)^{\kappa+4} - \ldots \tag{13}
\end{aligned}
$$

Therefore

$$
\begin{aligned}
x^\kappa \left[I_{-\kappa}(2\pi x) - I_\kappa(2\pi x) \right] &= \frac{1}{\Gamma(-\kappa+1)}\pi^{-\kappa} + \frac{1}{\Gamma(-\kappa+2)}\pi^{-\kappa+2}x^2 + \frac{1}{2\Gamma(-\kappa+3)}\pi^{-\kappa+4}x^4 + \ldots \\
&\quad - \frac{1}{\Gamma(\kappa+1)}\pi^\kappa x^{2\kappa} - \frac{1}{\Gamma(\kappa+2)}\pi^{\kappa+2}x^{2\kappa+2} - \frac{1}{2\Gamma(\kappa+3)}\pi^{\kappa+4}x^{2\kappa+4} - (14)
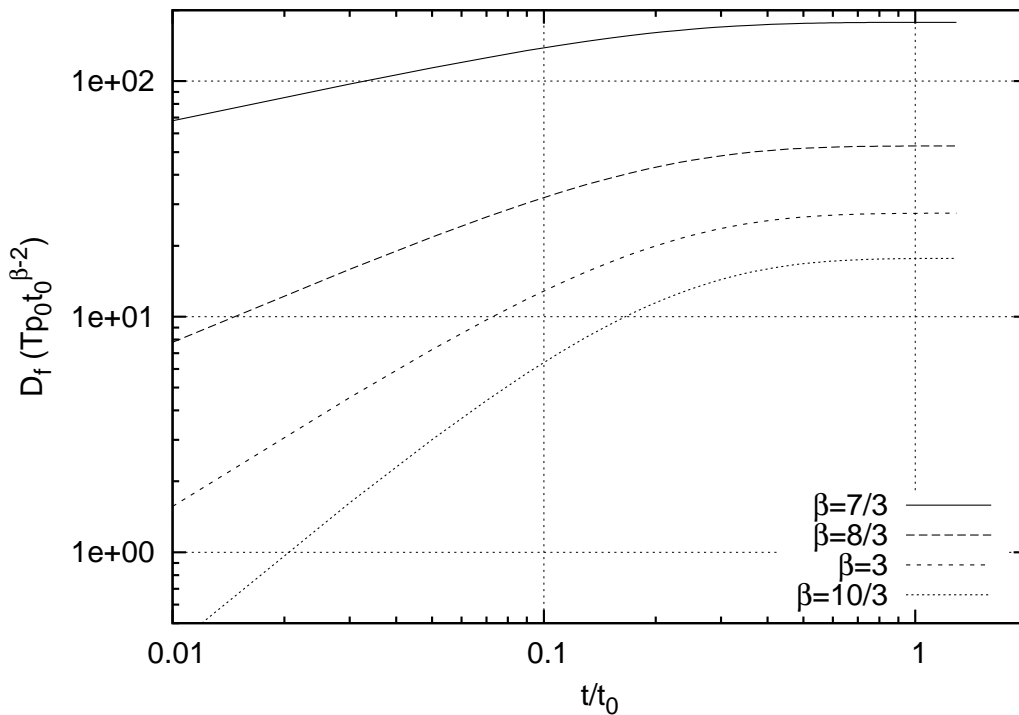\end{aligned}
$$

Figure 55: The structure function of $f(t)$ in (8) for the same exponents β as in Fig. 53, divided by $Tp_0 t_0^{\beta-2}$. Values are derived directly from a numerical evaluation of the modified Bessel function.

The first term on the right hand side will cancel with the last term in (11) by construction. With [1, 6.1.17][8, 8.334.3]

$$x^\kappa K_\kappa(2\pi x) - \frac{\Gamma(\kappa)}{2\pi^\kappa} = \frac{1}{2}\Big[\frac{\Gamma(\kappa)}{1-\kappa}\pi^{-\kappa+2}x^2 + \frac{\Gamma(\kappa)}{2(1-\kappa)(2-\kappa)}\pi^{-\kappa+4}x^4 + \dots$$
$$-\frac{\Gamma(1-\kappa)}{\kappa}\pi^\kappa x^{2\kappa} - \frac{\Gamma(1-\kappa)}{\kappa(1+\kappa)}\pi^{\kappa+2}x^{2\kappa+2} - \frac{\Gamma(1-\kappa)}{2\kappa(1+\kappa)(2+\kappa)}\pi^{\kappa+4}x^{2\kappa+4} - \dots\Big].$$

$\mathcal{D}$ requires the square of this, which we evaluate with the binomial theorem. As $x \to 0$, we extract the powers of x with the smallest exponents; supposed $2 < \beta < 4$, we have $0 < \kappa < 1/2$, therefore

$$\left[x^\kappa K_\kappa(2\pi x) - \frac{\Gamma(\kappa)}{2\pi^\kappa}\right]^2 \to \frac{1}{4}\left[\frac{\Gamma^2(1-\kappa)}{\kappa^2}\pi^{2\kappa}x^{4\kappa} - \frac{\Gamma(\kappa)\Gamma(1-\kappa)}{\kappa(1-\kappa)}\pi^2 x^{2+2\kappa} + O(x^{4+2\kappa})\right]. \tag{15}$$

The leading term is $\Gamma^2(3/2 - \beta/4)\pi^{\beta/2-1}(t/t_0)^{\beta-2}/[4(\beta/4 - 1/2)^2]$. Therefore

$$\mathcal{D}_f(t) \overset{t\to0}{\to} \left[2\sqrt{Tp_0}\frac{\pi^{\beta/4}t_0^{\beta/2-1}}{\Gamma(\beta/4)}\right]^2 \frac{\Gamma^2(3/2 - \beta/4)\pi^{\beta/2-1}}{4(\beta/4 - 1/2)^2}(t/t_0)^{\beta-2}. \tag{16}$$

After some manipulations with well-known functional equations of the Γ function this can be written as

$$\mathcal{D}_f(t) \overset{t\to0}{\to} Tp_0 D_0(\beta)t^{\beta-2} \tag{17}$$

where D_0 is defined in Table 3. This can be considered a straight-line fit to the initial segment $t/t_0 < 1$ in Figure 55.

β	$D_0(\beta) \equiv \frac{(2\pi)^\beta}{[(\beta-2)\cos(\pi\beta/4)\Gamma(\beta/2-1)]^2}$
7/3	315.889
5/2	205.621
8/3	168.576
3	157.914
10/3	187.218
7/2	215.600
11/3	255.770
4	389.636

Table 3:   The normalized factor D_0 for the coefficient of the dominating term of the von-Karman structure function at small times at some characteristic spectral indices β.

A factor in (17) defines C_f^2 (with some arbitrariness since this is only an adaptation to small t),

$$C_f^2 = Tp_0 D_0, \tag{18}$$

$$\mathcal{D}_f = C_f^2 \frac{t_0^{\beta-2}}{\pi^{\beta/2-1}\Gamma^2(1/2-\beta/4)}\left[2\left(\frac{t}{t_0}\right)^{\beta/4-1/2}K_{\beta/4-1/2}(2\pi t/t_0) - \frac{\Gamma(\beta/4-1/2)}{\pi^{\beta/4-1/2}}\right]^2. \tag{19}$$

5.3   Construction of Refractive Index Structure Functions

In most optical applications, the structure functions of the densities are converted to C_n^2, the structure functions of the refractive indices [5], according to the linearized template

$$n = 1 + \rho_{\text{dry}}\hat{\chi}_{\text{dry}}(\sigma) + \rho_{\text{H2O}}\hat{\chi}_{\text{H2O}}(\sigma), \tag{20}$$

where the intrinsic factors $\hat{\chi}$ for the susceptibilities depend on the wavenumber $\sigma = 1/\lambda$:

$$C_n^2 = C_{\rho\text{H2O}}^2 \hat{\chi}_{\text{H2O}}^2 + C_{\rho\text{dry}}^2 \hat{\chi}_{\text{dry}}^2, \tag{21}$$

where a mixed term $\propto \chi_{\text{H2O}}\chi_{\text{dry}}$ is ignored assuming that there is no strong correlation between water and dry air fluctuations. This is a completely separate theme with the wavelength added as a new parameter, and therefore just summarized with Figure 56 [13, 15]. The standard refractive indices at finite humidity (Fig. 3 of [14]) are an overlay of both subplots of this figure.
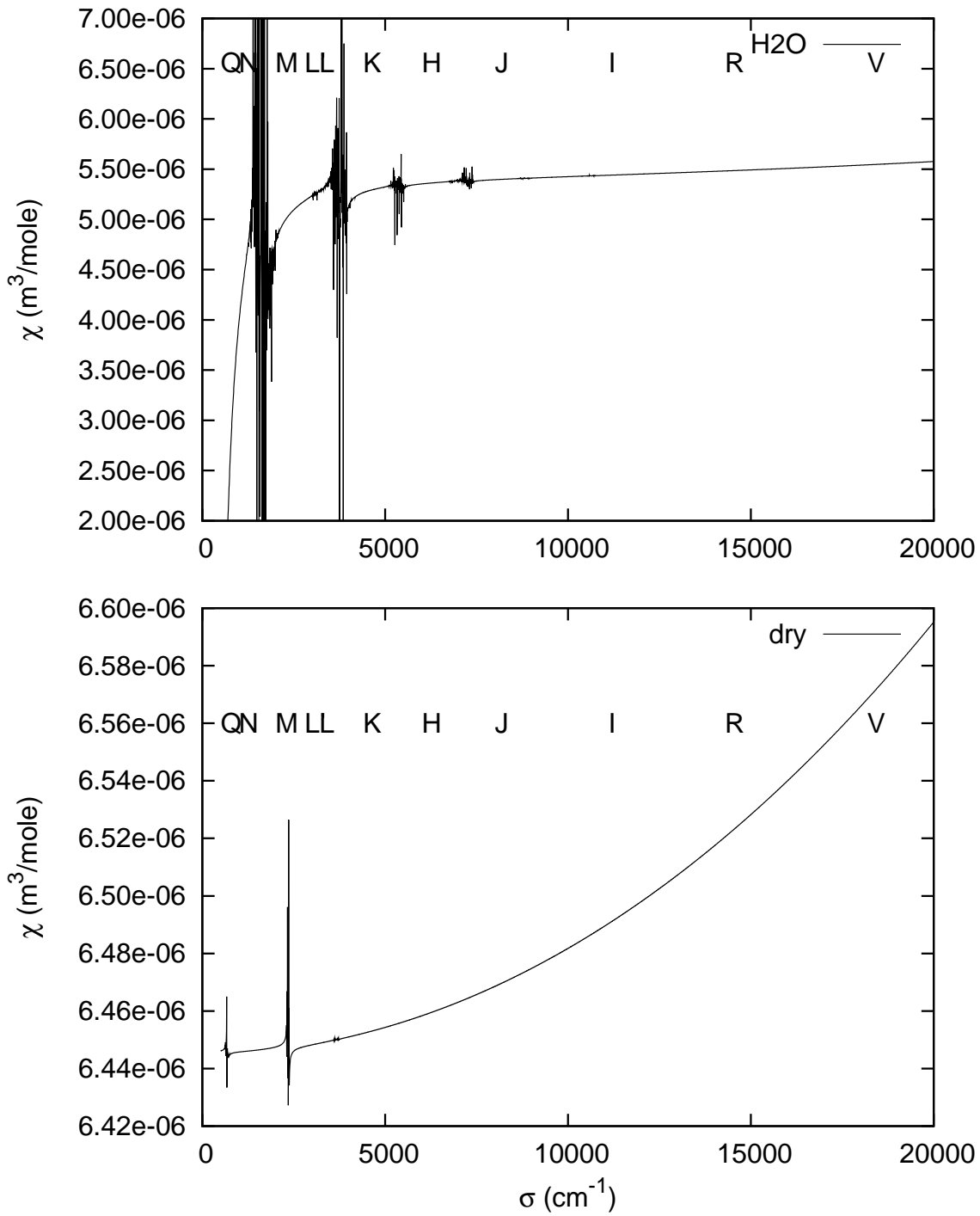
Figure 56: Generic factors $\hat{\chi}$ of the conversion of molecular densities to susceptibilities, as a function of wavenumber from mid-infrared to visible atmospheric windows, ignoring effects quadratic in the densities [12, Fig 2]. The upper plot is for pure water vapor, the lower for dry air.

5.4   Removal of Time Drifts

5.4.1   Conservation of Averages

Removal of a linear term prior to a Discrete Fourier Transform avoids appearance of spurious bumps in the transformed data, because a linear term is virtually interpreted as a series of ramps in the discrete transform, which virtually extends the input series periodically. We shortly describe the subtraction of the linear term, very similar to removal of the linear plus constant term is the standard least squares fit to a straight line. The input data are a series of points (x_i, f_i), enumerated $i = 0, \ldots N - 1$. The aim is to derive corrected values

$$f_i^c = f_i - a - b x_i, \quad i = 0, \ldots N - 1, \tag{22}$$

parametrized with an offset a and a slope b such that the mean (auto-correlation at zero delay etc.) is conserved. If we write averages with an overbar, $\bar{x} \equiv \sum_i x_i / N$, this is (up to a division through N) equivalent to $\sum_i f_i^c = \sum_i f_i$, which leads to

$$a = -b\bar{x}. \tag{23}$$

This eliminates one of the two free parameters (a, b) from the common least squares procedure, and we chose to eliminate the offset a, which yields

$$f_i^c = f_i + b(\bar{x} - x_i). \tag{24}$$

5.4.2   Version A: Minimized squared differences to a horizontal

To stay as horizontal as possible, we minimize

$$\sum_i (f_i^c - \bar{f})^2 \to \min. \tag{25}$$

Setting the first derivative with respect to b to zero yields

$$\sum_i [f_i + b(\bar{x} - x_i) - \bar{f}](\bar{x} - x_i) = 0 \Rightarrow \sum_i f_i(\bar{x} - x_i) + b \sum_i (\bar{x} - x_i)^2 = 0, \tag{26}$$

where we have used $\sum_i (\bar{x} - x_i) = 0$ to eliminate the term $\bar{f} \sum_i (\bar{x} - x_i)$. The result is

$$b = \frac{\sum_i f_i(x_i - \bar{x})}{\sum_i (x_i - \bar{x})^2}. \tag{27}$$

In the cases of this script, the x_i have been interpolated prior to a DFT on an equidistant grid,

$$x_i = i\Delta t + x_0, \quad i = 0, \ldots N - 1, \tag{28}$$

such that some summations can be simplified [8, 0.121], using $\bar{x} = (N-1)\Delta t/2 + x_0$ and $x_i - \bar{x} = \Delta t\,[i - (N-1)/2]$,

$$\sum_i (\bar{x} - x_i)^2 = (\Delta t)^2 N(N^2 - 1)/12. \tag{29}$$

In summary, the number

$$b\Delta t = \frac{12}{N(N^2 - 1)} \sum_i f_i \left(i - \frac{N-1}{2}\right) \tag{30}$$

is computed, then each term f_i individually replaced by

$$f_i^c = f_i + b\Delta t \left[\frac{N-1}{2} - i\right]. \tag{31}$$

5.4.3   Version B: Steadiness at start and end point

The variant proposed in the previous section to define the parameter b still leaves steps in the periodic continuation of f_i^c, which induces artificial powers at all frequencies. This can be eliminated by switching to a parameter b such that the corrected curve continues steadily (ie, with zero-th order periodic boundary conditions) through the terminating points:

$$f_0^c = f_{N-1}^c. \tag{32}$$

This reduces with (24) to

$$b = \frac{f_{N-1} - f_0}{x_{n-1} - x_0}. \tag{33}$$

$_{--}$**oOo**$_{---}$